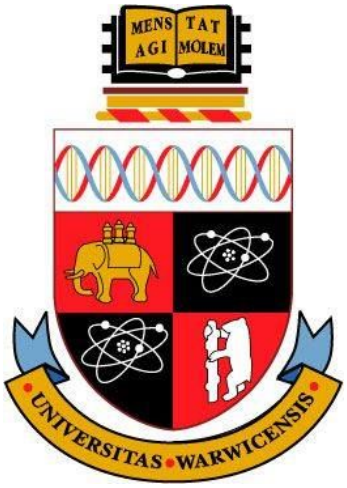

Effect of Ambient Gas on Cavity Formation for Sphere Impacts on Liquids

Hollis Williams

Department of Engineering
University of Warwick

This dissertation is submitted for the degree of
Doctor of Philosophy in Engineering

September 2022

Table of contents

List of figures

Acknowledgements

I would like to thank my supervisor Dr Petr Denissenko for his expertise and assistance during the project.

I would also like to thank Rosario Vidal Rojas and my brother Casey for general advice, Mojtaba Maali Amiri for useful discussions and my friend Alba Carballo González who has been encouraging and supporting me for many years.

Declaration

This thesis is submitted to the University of Warwick in support of my application for the degree of Doctor of Philosophy. It has been composed by myself and has not been submitted in any previous application for any degree. The work presented was carried out in full by the author. Parts of this thesis have been published by the author and are detailed in the list of publications.

Hollis Williams
September 2022

Abstract

Formation of a splash crown and a cavity following the impact of a sphere on a body of liquid is a classical problem. In the related problem of droplet splashing on a flat surface, it has been established that the properties of the surrounding gas can influence the threshold speed at which splashing occurs. At lower impact speeds, this is due mainly to the influence of gas kinetic effects, since the height of the gas lubrication film which is displaced during dynamic wetting is often comparable to the mean free path of the gas. At higher Weber and Reynolds numbers, on the other hand, inertial effects dominate and the density of the gas becomes important in determining whether a splash occurs. Since the influence of the ambient gas on the droplet impact has been known since the beginning of the twentieth century, it is of theoretical importance to investigate whether a similar phenomenon occurs during entry of projectiles into liquids and test the applicability of the wetting theory which is used for droplet impacts.

In this work, we present experimental and theoretical investigations of the influence of the ambient gas on cavity formation during a sphere impact on a free liquid surface. In the experiments, a vacuum chamber was used to provide ambient conditions from atmospheric pressure down to $1/100$-th of an atmosphere, whist high-speed photography is used to provide detailed images both of the cavity beneath the surface and the splash crown and jets which form above the surface. To elucidate the primary forces at work, we vary the radius of the sphere, the properties of the liquid, the ambient gas pressure, and the type of gas. It is found that the threshold entry speed for cavity formation is influenced by the density of the surrounding gas, whereas changing the mean free path of the gas has no effect.

We attribute this phenomenon to the gas slowing the sealing of the thin crown sheet behind the sphere. This assertion is supported with detailed optical measurements of the liquid sheet thickness. In the range of parameters considered, the splash crown influences the movement of the contact line. Finally, we extend our investigations by performing simulations of the impact of a hydrophobic sphere on the surface of a body of water in the presence of ambient air above the liquid. For this purpose, we employ a three-dimensional Eulerian volume of fluid (VOF) multiphase model which uses overlapping meshes. We find that decreasing ambient gas density is not able to suppress cavity formation in the case

of hydrophobic spheres.

Some of the material in the thesis has appeared previously in the following publications:

- H. Williams, J. Sprittles, J. Padrino and P. Denissenko, Effect of ambient gas on cavity formation for sphere impacts on liquids, Phys. Rev. Fluids **7**, 094003 (2022).
- H. Williams, A case study of optical methods for measuring thickness of liquid sheets, Res. Opt. **8**, 100266 (2022).
- H. Williams, Influence of curved surface roughness on white light interferometer microscopy, Phys. Educ. **57**, 015001 (2021).

Chapter 1

Introduction

The study of splashes (the sudden disturbance of a free liquid surface by an instantaneous impact) is a classical subject which has been analysed since the nineteenth century. In particular, by the 1870s Worthington and Cole had already studied and obtained clear images of splashes produced by a droplet impacting a horizontal solid plate, a droplet impacting the free surface of another liquid, and a solid sphere impacting the free surface of a liquid [1, 2]. In Figure 1.1, we show an image of a splash obtained by Worthington in 1908 using single-spark photography and a much more recent image obtained by Marston et al. [3] in 2016 using high-speed photography. One notes that although key features of the flow can be distinguished in the earlier photo, the more recent image is much more detailed. The fact that the image is obtained from a video sequence also enables one to make quantitative rather than qualitative statements about the splash.

The original motivation of the work of Worthington and Cole was to study splashing as a fundamental fluid dynamical process, but it soon became clear that the problem of a sphere impacting on a liquid had practical military applications, where it is necessary to understand the phenomena which accompany water entry of a projectile. It must be emphasised that in these practical applications, the splash is only one of the phenomena which accompanies water entry of a projectile and that one must also understand the physics of the jets and cavities which occur, where the word cavity always refers in this work to the air cavity which follows behind the sphere as it splashes and falls beneath the free surface of the liquid [4–6]. If the splash behind the sphere seals quickly, the cavity pinches off and further growth of the cavity is prevented, affecting the ability to follow or detect the projectile as it falls through the liquid.

A second major reason for studying sphere impacts on liquids is that spherical impactors are simple, symmetric idealisations of more complicated bodies which typically impact on free liquid bodies (including ships and seaplane floats). The study of the forces involved when blunt objects slam into a large body of water was initiated by von Kármán [7],

Fig. 1.1 Left: splash created after the impact of a rough sphere on a liquid, obtained using single-spark photography [2]. Right: splash following the impact of a 10 mm steel sphere onto water at 10 ms^{-1} at atmospheric conditions, obtained using high-speed photography [3] .

who studied the impact pressure on the bottom of wedge-shaped seaplanes landing on a body of water, with applications to aeronautics in mind. This theory has since been extended to more complicated compressible and incompressible models [8–11]. A number of applications have also been found for the droplet-liquid impact and the droplet-solid impact. In the case of a droplet impacting a solid surface, there are highly important applications to spray-cooling, combustion, and coating processes, whereas both types of impact have applications to ink-jet printing [12–16].

Sphere impacts on liquids and droplet impacts on solids have been studied very intensively, both on the experimental and the theoretical side [17–20]. Given the relative simplicity of the sphere and droplet impacts, they are ideal problems to verify complicated theoretical models of free surface disturbances under impact. A common approach in modelling the droplet impact is to consider the jet which is ejected during the initial moment of impact and then to study the wedge region created between the advancing liquid front and the solid substrate, with the transition from splash to no-splash being determined by the balance of forces which either lifts or fails to lift the expanding liquid sheet away from the solid. Since there is no universally agreed upon model to be used either for the droplet or the sphere impact problems, the main investigations are frequently experimental or use machine learning to deal with large amounts of experimental data from disparate sources [21].

1.1 Research Objectives

The central theme of this work is the influence of the ambient gas on cavity formation during a sphere impact on a free liquid body. This is to be distinguished from the large number of related works in the existing literature which consider the influence of the atmospheric pressure on the time evolution of the cavity once the sphere has passed below the free surface or the formation and dynamics of the above-surface splash crown with no reference to the associated cavity [3–6]. In this work, we investigate the possibility that in certain regimes it might be possible to suppress a cavity entirely by changing the properties of the ambient gas. This is inspired by results which show that splashing during droplet impacts can be completely suppressed by lowering the ambient gas pressure [17]. Given that the influence of the gas on the outcome of droplet impacts has been studied since [17], it would seem to be a priority to investigate whether the same phenomenon can occur in a sphere impact, in order to know how widely applicable are the wetting models which are used for droplet impacts. No previous authors have studied this possibility directly and whilst the experimental set-up which we use does not currently have a direct application besides projectile impacts in rarefied atmospheres, our findings may be useful for deriving models which incorporate both droplet-solid and solid-liquid impacts.

The thesis is structured into six chapters. Chapter 1 introduces the topic and provides a general overview of splashing phenomena, which include droplet impacts on solid surfaces, droplet impacts on liquid surfaces, and sphere impacts on liquid surfaces. Chapter 2 covers the literature associated with these impacts, presenting previous results and also covering the necessary technical details of wetting phenomena. Chapter 3 covers the design of the experimental set-up used throughout the thesis, as well as the main experimental results obtained. Chapter 4 describes the remaining experimental results, which include the optical measurements which were performed of the thickness of the splash curtain. Chapter 5 describes the theoretical model which was proposed to explain the experimental findings and also explores computational simulations which were performed to investigate the influence of gas density on cavity formation for hydrophobic spheres. Chapter 6 concludes the thesis with evaluation of results and potential ways in which the research could be extended.

Chapter 2

Literature Review

In this chapter we outline literature which is relevant for the research topic.

2.1 Droplet-Liquid Impacts

The original work of Worthington and Cole [1, 2] identified three main scenarios of interest when considering the physics of a splash: that of a droplet impacting on a liquid body, that of a droplet impacting a solid substrate, and that of a solid sphere impacting on a liquid body. Although the droplet-liquid impact is likely of least relevance to our research topic, there are still some similarities with the case which we study, so we we will consider this type of impact first before moving on to droplet-solid and sphere-liquid impacts.

2.1.1 Experimental Set-up

A key difference which occurs in the droplet-liquid compared to the droplet-solid impact is the different set of parameters which may be varied during an experiment (shown schematically in Figure 2.1) [22–24]. One notes that whereas the droplet-solid impact allows for variation in the properties of the solid, the droplet-liquid impact can be studied using different liquids or different depths of the liquid body. It is also worth noting that in comparison to the sphere impact, droplets may be spherical, deformed, or oscillating (only spherical droplets were considered in the work of Worthington) [1, 2].

Although experimental investigations focus on different parameters or stages of the impact process, the experimental set-up is usually quite similar and a typical example used by Castrejón-Pita et al. [25] is shown in Figure 2.2. Droplets (usually with radii between 1 and 3 mm) are produced above a liquid pool and fall under gravity to impact on the pool. The liquid used is typically a water-ethanol mixture. These are good models for Newtonian fluids, since their viscosities range from 1 mPa s to 1.5 Pa s with only small

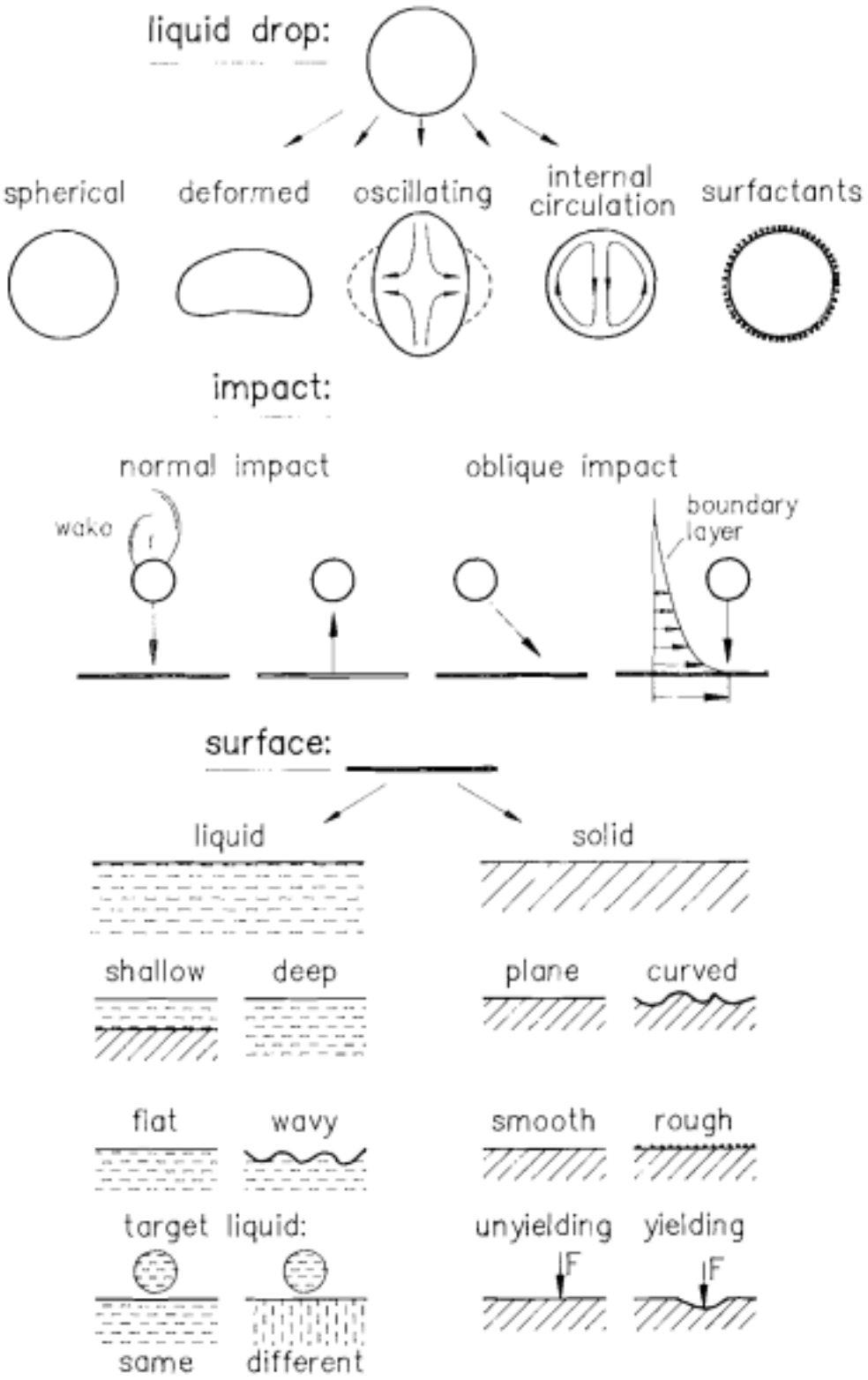

Fig. 2.1 Survey of parameters governing the impact of a liquid drop [22].

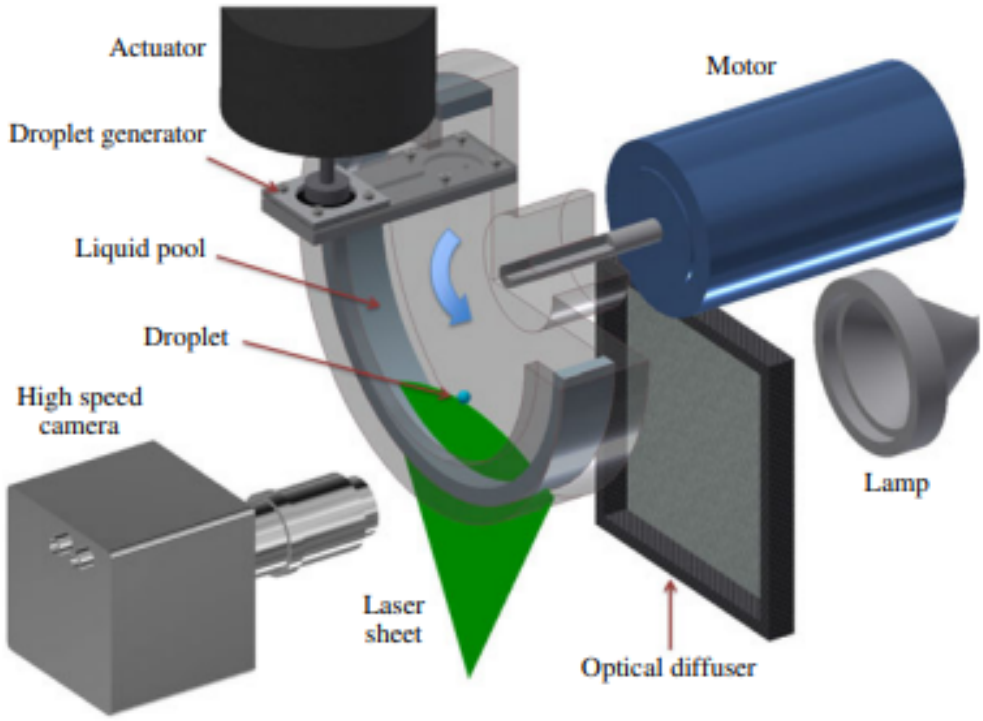

Fig. 2.2 Schematic view of the experimental set-up for a droplet impacting a moving liquid surface, including a view of the liquid channel [25].

variations in surface tension [26–28]. Droplets of different sizes and speeds are formed either by dripping or jetting, with the conditions being controlled by adjusting the dripping flow or the size of the nozzle. More information on pinch-off and breakup of dripping droplets of near-inviscid Newtonian fluids and droplet formation from a drop-on-demand printhead may be found at [29, 30]. The depth of the pool is carefully adjusted without splashing droplets or introducing bubbles onto the walls of the channel which would obstruct visualisation. In the set-up shown in Figure 2.2, the liquid surface moves at a constant speed at a right angle to the motion of the impacting droplet, but this is not essential. High impact speeds can be produced either by using a large drop height or by using an electromagnetic actuator to push the liquid out of the nozzle: the latter method allows for impact speeds between 1.2 and 1.7 ms^{-1} [25].

The main obstruction to studying the droplet-liquid impact quantitatively is the difficulty of being able to observe the internal dynamics of the droplet and the liquid pool. High-speed photography can be used to monitor mixing at the interface as well as the dynamics directly above and below the surface. Grey scale shadowgraphy and laser-sheet visualisation allow for a determination of the impact dynamics over the surface of the pool, whereas colour imaging and laser fluorescence provide more detailed information on the internal dynamics. A combination of these techniques then allows for visualisation of the

flow and the internal dynamics of the droplet and the liquid pool [25]. Similar experimental set-ups are described by Roy et al. [31] and Lee et al. [32], with both of these experiments focusing on the entrainment of air during an impact. Experiments of Fudge et al. [33] have considered the impact of a droplet onto a pool composed of a different liquid, a scenario which is complicated due to the fact that viscosity and density ratios may greatly affect the speed of penetration.

2.1.2 Results

The main qualitative result of Castrejón-Pita et al. is that the impact behaviour can be classified into four regimes: surfing, smooth coalescence, lamella jetting and splashing [25]. In the surfing regime (commonly found when using higher viscosity liquids, low to medium impact speeds and high relative speeds of the liquid surface), the droplet bounces and levitates on an air cushion above the surface. The word 'surfing' refers to the fact that in these experiments the liquid bath is moving. In the smooth coalescence regime, the drop penetrates the pool and merges with it, with almost no mixing at the interface. The depth reached by the drop depends on the absolute velocity. In the lamella jetting regime, the droplet partially coalesces at the first point of contact, but not all of the volume merges into the pool. In the splashing regime, the rear part of the impacting droplet quickly coalesces with the pool whilst a lamella emerges from the front of the drop.

These results are summarised in Figure 2.3, which shows the regimes of different impact dynamics for a droplet impact on a liquid pool in terms of relevant dimensionless numbers for glycerol-water mixtures over a wide range of impact conditions, where v_n denotes the impact speed of the drop, v_t is the tangential relative speed of the liquid surface, and Re and We are dimensionless quantities defined as

$$\mathrm{Re} = \frac{\rho U L}{\mu}, \tag{2.1a}$$

$$\mathrm{We} = \frac{\rho U^2 L}{\gamma_{lv}}. \tag{2.1b}$$

ρ is the density of the liquid, L is the characteristic length scale, U is the flow speed, μ is the dynamic viscosity of the liquid, and γ_{lv} is the liquid-vapour surface tension. The Reynolds number Re quantifies the relative importance of inertial and viscous stresses and the Weber number We quantifies the relative importance of inertial and surface tension stresses.

Lee et al. [32] used ultrafast X-ray phase-contrast imaging to observe the evolution of the entrained air during droplet impact, finding that the evolution of the entrained air and whether it evolves into single or double bubbles is affected by the interaction

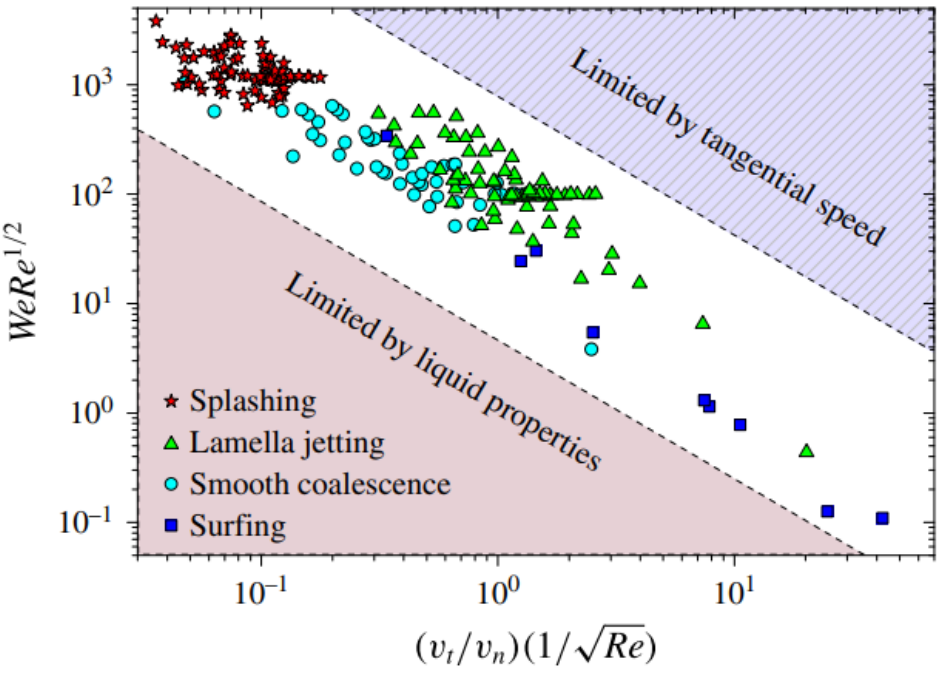

Fig. 2.3 Regime dynamics showing different impact dynamics for a droplet impact on a translating liquid pool in terms of relevant dimensionless numbers for glycerol-water mixtures [25] .

between inertial forces, viscous forces and capillarity. A phase diagram (shown in Figure 2.4) characterises the possible outcomes of the entrained air as a function of the inverse Ohnesorge number and the Weber number for the air film which is defined to be $\mathrm{We}_{\mathrm{film}} = \rho v^2 \delta/\gamma$, where v is the speed of retraction of the entrained air film and δ is the thickness of the air film modelled as a flat disc with a radius R. Both v and δ were measured experimentally using X-ray imaging. The Ohnesorge number Oh represents the effect of viscosity over inertia and surface tension and is defined to be

$$\mathrm{Oh} = \frac{\mu}{\sqrt{\rho \sigma L}}. \tag{2.2}$$

The properties of the ambient gas were not considered in these experiments.

Roy et al. [31] studied the entrapped air cushion during a droplet impact on an immiscible liquid pool, finding that the radius of the air disc grows as $t^{2/3}$ due to the very small capillary number, which is of order 10^{-4}. Hydrodynamic structures were also observed in the air disc during impacts at low Weber numbers of order 10. Das et al. [34] studied the formation and evolution of jets from the free surface during droplet impact, observing that different quantities related to the jets have a dependence on the Froude number Fr, which is defined as

$$\mathrm{Fr} = \frac{U}{\sqrt{gL}}, \tag{2.3}$$

where g is the acceleration due to gravity. In Fig 2.5, the central jet height and the jet velocity are plotted against the Froude number along with a linear fitting curve [34]. It was also established that there is a relation between cavity and jet formation, since the dimensionless jet velocity may be expressed as a function of Fr, We, and the minimum radius of the cavity.

Cavity formation and geometry have been studied by Minami et al. [35], Berberovic et al. [36], and Jain et al. [37]. A qualitative finding of this work is that the viscosity of the liquid used for the droplet may affect the geometry of the cavity, since droplets of water, ethanol, and silicone oil (1, 10, and 100 cSt) form hemispherical cavities, whereas a 1000 cSt silicone oil droplet forms a cylindrical cavity. It was also observed that the normalized cavity depth increases with Froude number. This is shown in Figure 2.6, which plots the maximum depth of a cavity formed under each Froude number condition for droplets of pure water and silicone oil with differing viscosities [35]. The vertical axis shows the dimensionless number given by the ratio of the maximum cavity depth divided by the initial droplet diameter, where the theoretical value for the maximum depth is calculated as

$$\frac{H_c}{d} = \left(\frac{\mathrm{Fr}}{3}\frac{\rho_d}{\rho_p}\right)^{1/4}, \tag{2.4}$$

where ρ_d is the density of the liquid droplet and ρ_p is the density of the liquid pool.

2.1.3 Flow Description

The experimental results provided in the previous section enable a classification and a detailed description of the diverse range of possible phenomena which may be observed during impact both above and below the free surface of the liquid, but do not provide much insight into the underlying physical processes. The transition between coalescence with the liquid pool or splashing is complicated and proceeds via several intermediate steps, which include jet formation and entrapment of gas bubbles [38]. However, although the phenomena involved are complicated, the main underlying physical principle is that there is a balance of forces during impact which influence both the flow field during impact and the final outcome afterwards, which can be split roughly into gravity, viscosity, inertia, and surface tension. Depending on the evolution of the flow, certain of these may become less significant. As an example, once the hole created by a droplet impact has reached its maximum possible diameter and depth, inertial forces become less significant and the way that the holes recedes (or retracts) is governed mostly by surface tension. On the other hand, capillarity is responsible for the formation of the liquid rim during impact [39].

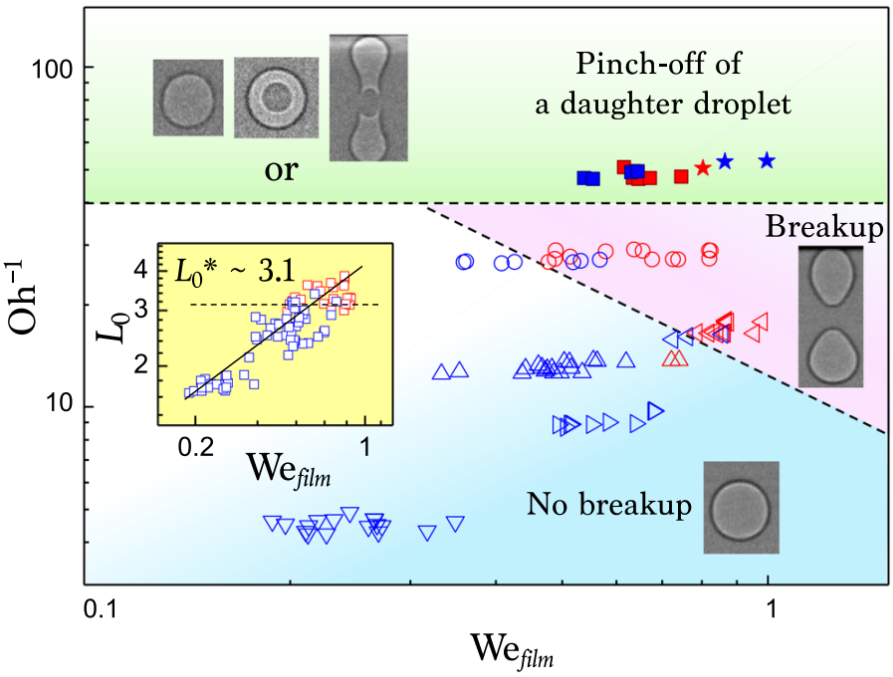

Fig. 2.4 Phase diagram for the bubble evolution with respect to We_{film} and Oh^{-1}. Blue open symbols represent retraction into one bubble, red open symbols represent the breakup into a double bubble, blue closed symbols represent an antibubble formed when a small daughter droplet is encapsulated by a larger air shell bubble, and red closed symbols represent a double bubble. Inset: aspect ratio L_0 of a bubble, measured as a function of We_{film} for liquids [32].

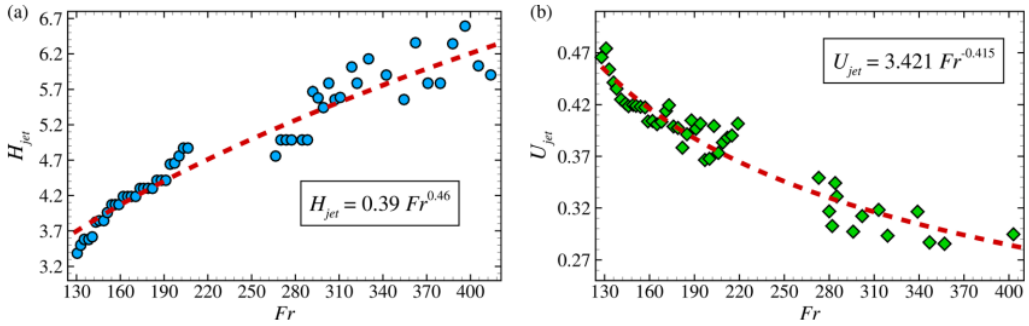

Fig. 2.5 Quantities plotted against the Froude number: (a) central jet height and (b) jet velocity. The dashed red line represents the linear fit, with the fitting value shown in the inset [34].

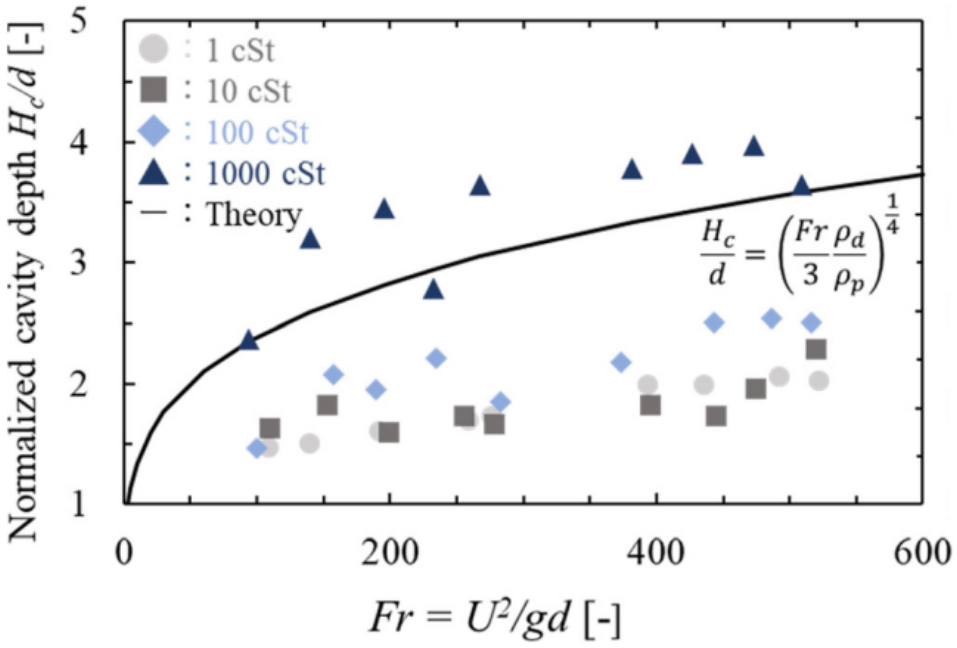

Fig. 2.6 Normalized cavity depth for droplet impact on a liquid pool plotted against Froude number [35] .

Since the system is a multiphase system with a liquid and a gaseous phase, the starting point for the models of Das et al. [34], Castillo-Orozco et al. [40], Berberovic et al. [36], and Ray et al. [38] is that one can use a two-fluid model for a two-phase flow, in which phase fraction equations are solved separately for each individual phase. This is obviously distinct from the droplet-solid and solid-liquid impacts which we will consider shortly, where the situation is very different because one must model the properties of the solid. Both the liquid and the air phase satisfy the mass and momentum equations for incompressible Newtonian fluids [41]:

$$\nabla \cdot \mathbf{V} = 0, \tag{2.5a}$$

$$\rho\left(\frac{\partial \mathbf{V}}{\partial t} + \nabla \cdot \mathbf{V}\mathbf{V}\right) = \nabla P + \rho g + \nabla \cdot [\mu(\nabla \mathbf{V} + (\nabla \mathbf{V})^T)] + f_{sv}, \tag{2.5b}$$

where $\mathbf{V}$ is the velocity vector, P is the pressure, and f_{sv} is the surface tension force per unit volume. At the interface, one specifies a modified momentum equation which incorporates the surface tension force

$$\rho\left(\frac{\partial \mathbf{V}}{\partial t} + \nabla \cdot \mathbf{V}\mathbf{V}\right) = \nabla P + \rho g + \nabla \cdot [\mu(\nabla \mathbf{V} + (\nabla \mathbf{V})^T)] + \sigma \kappa \mathbf{n} \delta_s, \tag{2.6}$$

where σ is the surface tension force, $\mathbf{n}$ is the unit normal vector at the interface, κ is the mean curvature of the interface, and δ_s is the interface Dirac delta function. Boundary conditions are the slip condition at the left and right boundaries of the computational domain, outflow conditions on the top of the domain, and impermeability conditions on the bottom of the domain. The equations of motion and boundary conditions may then be cast into dimensionless form using the Froude, Reynolds, and Weber numbers.

Although the phenomena at work are very complex, numerical solution of this two-phase boundary value problem finds that there are three basic stages which occur for all phenomena: formation of a hole (or crater) with a rim during impact which expands, retraction of the rim leading to retraction of the crater side, and retraction of the crater base [38]. In Figure 2.7, we show that for coalescence and all types of jet formation (including those where bubbles are entrapped), the time for retraction of the rim (or wave swell), the crater retraction time, and the maximum crater depth do not vary much, although the wave swell height increases with impact velocity.

Since the crater (or cavity) growth and retraction is fundamental to the droplet-liquid impact (regardless of jet formation and bubble entrapment) which may occur, many analytic models have been proposed to estimate the crater growth over time by considering a spherical crater in potential flow: this includes the models of Engel [42], Liow [43], Berberovic et al. [36], and Bisighini and Cossali [44]. Arguing from physical intuition, Liow [43] argued that for a relatively high-speed impact of a water droplet on a pool of water, the gravitational potential energy of the cavity, the rim and the free surface, the kinetic energy in the cavity and the cylindrical wave produced by the impact, and the dissipated energy may be equated with half of the energy of the impacting droplet, which enables one to derive an expression for the kinetic energy E_k of the cavity

$$E_k = -\frac{\rho}{2}\int\int \phi \frac{\partial \phi}{\partial r} dS = \pi \rho R^3 \left(\frac{dR}{dt}\right)^2, \tag{2.7}$$

where R is the cavity radius, ϕ is the velocity potential, and S is the surface element.

Furthermore, it was argued that for large Froude numbers, the kinetic energy does not change much in the early stages of cavity formation, so that for constant kinetic energy the crater grows with time as $R^{5/2}$. The model of Berberovic et al. [36] was based on balancing the linear momentum of the liquid around the cavity at high Weber and Froude numbers, showing that the crater grows asymptotically as $R = t^{-4/5}(5t-6)^{2/5}$. Although the droplet-liquid impact is a very complex problem, we have emphasised in this section that some simplifications are possible both on the analytic and the numerical side, especially if one considers a liquid droplet which impacts a pool composed of the same liquid. As might also be expected from physical intuition regarding multiphase flows, it also turns out that despite the very large number of ancillary phenomena which may occur

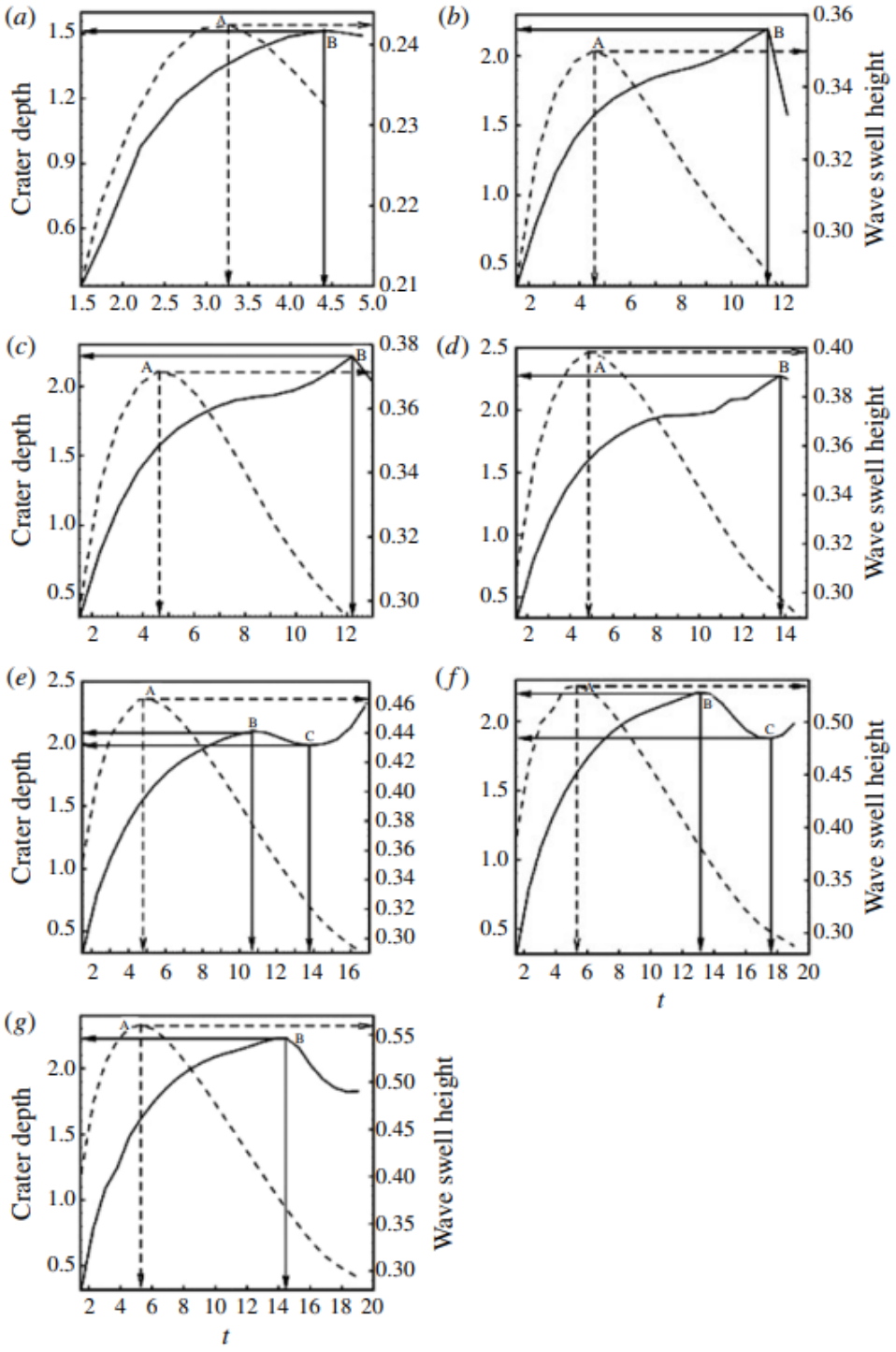

Fig. 2.7 Crater depth and wave swell height during (a) coalescence, (b) formation of a short thick jet, (c) formation of a thick jet with a secondary droplet, (d) formation of a thin jet, (e) formation of a thin jet and entrapment of a large bubble, (f) formation of a long thick jet and entrapment of a small bubble, and (g) formation of a long thick jet only [38] .

in the form of coalescence, jet ejection, bubble entrapment, and secondary droplet ejection, there is a universal feature (formation of a cavity in the disturbed liquid surface) which always occurs when a droplet impinges upon the surface of another liquid and it is possible to analyse this feature in great detail. In the next section, we will introduce a solid surface into the system which significantly complicates the problem even further.

2.2 Droplet-Solid Impacts

Of greater relevance for this thesis is the problem of a liquid droplet which impacts a solid surface. Research into this topic could be used to understand splashing of raindrops, impact of fuel droplets on the walls of a combustion chamber, pesticide and paint sprays, inkjet printing, and soil erosion. One of the key parameters which can be varied for droplet-solid impacts is the wetness of the solid substrate which is used for the impact: the substrate may be dry or it may be coated with a thin liquid film [45–47, 23, 48]. In this case, depending on the depth of the liquid film in comparision to the radius of the liquid droplet, there may be substantial overlap with the case of the droplet impact on a liquid pool which we outlined in the previous section.

We will focus in this section on the case of a dry smooth surface, where there is overlap with the sphere-liquid impact problem which we study in this thesis. We will mention that Josserand et el. [47] found that splash formation on a thin liquid film depends on the inertial dynamics of the liquid and the cushioning of the gas. Two asymptotic regimes were identified: one which occurs for occurs for weak gas cushioning characterized by jet formation after entrapment of a sequence of bubbles where the jet speed is mainly controlled by the Reynolds number of the impact, and the other for significant air cushioning which is characterised by entrapment of a single bubble and a slower jet velocity. In the latter case, the dynamics is controlled by the lubrication of the gas between the droplet and the liquid film.

2.2.1 Experimental Set-up

The experimental set-up in the case of the droplet-solid impact is similar to that of the droplet-liquid impact. A typical example with a flywheel set-up is shown in Figure 2.8 [49]. Water droplets of diameter $D \approx 3.7$ mm and formed and released by a droplet generator similar to ones discussed in Section 2.1. The droplets fall freely under gravity where they usually impact a glass microscope slide. In the set-up of Burzynski and Banmer [49], the impact substrate is mounted to the side of a flywheel which rotates at a constant angular velocity ω. The relative velocity between the falling droplet and the impact substrate determines the impact speed, which is held constant at a high speed of $U \approx 10$ ms^{-1}.

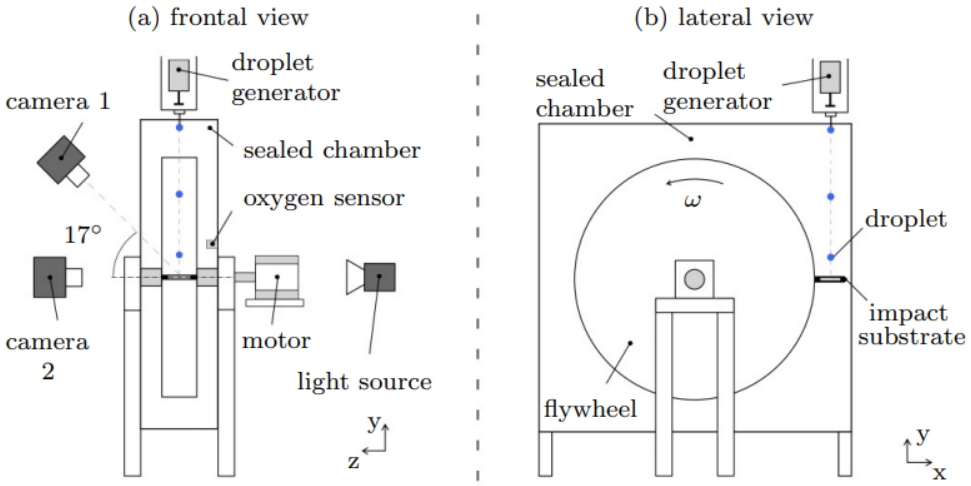

Fig. 2.8 Experimental set-up for droplet impacts on a flat substrate. (a) Sketch of the flywheel experiment showing the shadowgraph setup, consisting of two high-resolution cameras and a laser light source. (b) Sketch demonstrating the operation of the wheel and the position of the substrate when the impact occurs [49] .

The flywheel is sealed in a chamber to allow for the use of different gases. The oxygen concentration and the absolute pressure are measured to calculate the properties of the gas mixture [50, 51]. The use of a transparent vacuum chamber is employed in many versions of the experiment, including those of Ashida et al. [52], Xu et al. [53, 17] and Riboux and Gordillo [18–20], since it allows for investigation of the properties of the ambient gas on the process [54]. There are also a wide range of experimental set-ups which consider the properties of the roughness and texture of the surface on splashing, where the impact substrate is roughened or etched with various patterns. This includes the experiments of Marengo et al. [55], Palacios et al. [56], Hao [57] and Xu [58]. Similarly to droplet-liquid impacts, a combination of laser-sheet visualisation and shadowgraph methods may be used to visualise the dynamics in the early stages of the droplet-solid impact [49, 59].

2.2.2 Results

There are several main possible outcomes for droplet impact on a flat dry solid surface, which are shown in Figure 2.9. These are bouncing, splashing (where the edges of the droplet lift away from the surface and break up into secondary droplets), and spreading (where the droplet spreads out on the solid substrate without splashing). The splashing phenomenon can also divided into separate types of splashing: corona splashing (characterised by lift-off of the lamella and and early-stage ejected secondary droplets) and prompt splashing (where small droplet are ejected directly from the advancing liquid-substrate contact line) [53, 60]. The distinction between corona splashing and prompt splashing is

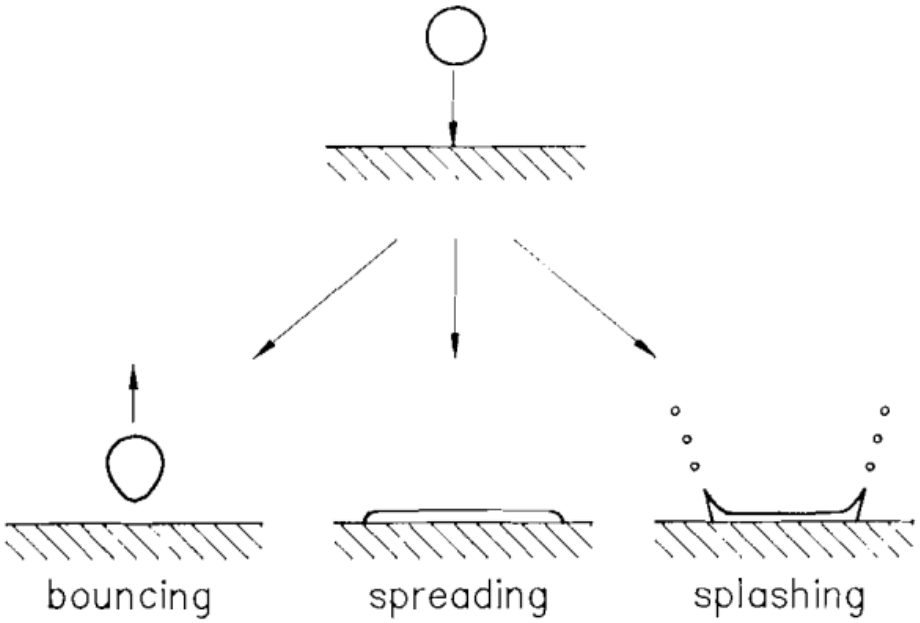

Fig. 2.9 Possible outcomes of a droplet splash on a flat dry surface [22].

not clear for a smooth compared to a rough impact substrate, so it is often assumed that the threshold speed for prompt splashing is equal to that of corona splashing on smooth substrates [24].

We will begin by outlining some of the key experimental results in the recent literature concerning the influence of the ambient gas. The seminal result in this area was that of Xu et al. [17], who found that splashing can be completely suppressed by decreasing the pressure of the surrounding gas, where the threshold pressure for splashing to occur is a function of the impact speed and scales with the molecular mass of the gas and the viscosity of the liquid. In Figure 2.10, we show a sequence of images demonstrating that splashing and ejection of secondary droplets may be suppressed by gradually lowering the pressure of ambient gas [17].

The experiments were in a regime above the point where dynamic viscosity of air varies with pressure, which occurs when the mean free path of the molecules is above the geometric length scale. Another possibility is that the splash threshold depends on the mean free path λ of the gas:

$$\lambda = \frac{\mu}{\rho}\sqrt{\frac{\pi M}{2kT}}, \tag{2.8}$$

where μ is the viscosity, M is the molecular mass of the gas, k is the Boltzmann constant, and T is the temperature. The dependence on gas density ρ can be seen in the above

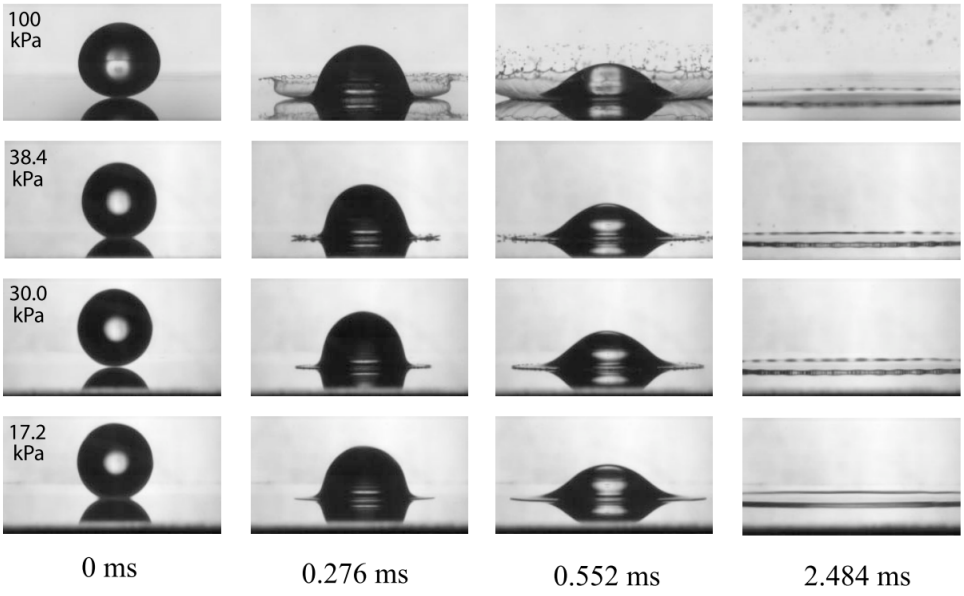

Fig. 2.10 Photographs of a liquid drop hitting a smooth dry substrate. A 3.4 ± 0.1 mm diameter alcohol drop hits a smooth glass substrate at an impact speed of 3.74 ± 0.02 ms^{-1} in the presence of different background pressures of air. The top row shows splashing at atmospheric pressure, the second row shows impact at 38.4 kPa, the third row shows impact at 30.0 kPa, and the bottom row shows impact at 17.2 kPa, where splashing is completely suppressed [17] .

equation, where the density can be altered by changing the pressure of the gas (this follows from the ideal gas equation).

Xu et al. [17] suggest that one should consider the stress on the expanding liquid layer after impact. There are two contributions here: the stress Σ_G due to the pressure of the gas acting on the spreading liquid which deflects the liquid front upwards, and the stress Σ_L due to the surface tension of the liquid, which prefers to stabilise the liquid and keep it intact (we will see shortly that the presence of the gas close to the spreading liquid front is also of key importance for the sphere impact problem). They argued that Σ_G should depend on the compressibility of the air, because the characteristic length scale over which the flow is close to the spreading liquid rim is small [61]. This implies the following estimate for Σ_G:

$$\Sigma_G \sim \rho_G C_G V_e \sim \frac{PM}{kT}\sqrt{\frac{\gamma kT}{M}}\sqrt{\frac{RV_0}{2t}}, \tag{2.9}$$

where C_G is the speed of sound in the gas, V_e is the expanding velocity of the liquid layer on the substrate, γ is the adiabatic constant of the gas, R is the initial radius of the droplet, t is the time measured from impact, and V_0 is the velocity of the drop.

To estimate Σ_L, one considers the surface tension pressure close to the advancing liquid front, which is given by the ratio of the surface tension coefficient σ to the thickness of the liquid layer at the front. This gives us

$$\Sigma_L = \frac{\sigma}{d} = \frac{\sigma}{\sqrt{\nu_L t}}, \tag{2.10}$$

where ν_L is the kinematic viscosity of the liquid. These estimates combined imply

$$\frac{\Sigma_G}{\Sigma_L} = \sqrt{\gamma M} P \sqrt{\frac{RV_0}{2kT}} \frac{\sqrt{\nu_L}}{\sigma}. \tag{2.11}$$

If the two stresses are comparable in magnitude, the liquid rim is deflected upwards, resulting in ejection of droplets. A major qualitative prediction of this ratio is that more viscous liquids splash more easily than less viscous liquids. This is a somewhat counter-intuitive conclusion, since one might expect that a droplet which is more viscous would be harder to splash against a solid substrate. Xu et al. [17] also found that there is a good collapse of the data when V_0 is plotted against Σ_G/Σ_L. This argument leads to a collapse of the splashing threshold, but no mechanism was proposed for the process. Although no detailed model was proposed, the above experimental scaling relations support a model in which compressible effects in the gas are responsible for splashing in droplet-solid impacts.

Burzynski and Bansmer [49] studied the role of the ambient gas at higher impact speeds, finding that gas entrapmment is not the mechanism which is responsible for droplet splashing at high Weber and Reynolds numbers and that splashing is influenced primarily by the density, not the mean free path, of the surrounding gas. In Figure 2.11 (left), splashing is shown at the same impact speed but with four different gases at atmospheric pressure, showing that the type of gas changes the outcome of the impact and the volume ejected. Figure 2.11 (right) shows the total ejected volume normalized to the primary droplet volume over the splashing parameter β, which will be described when we explain the model of Gordillo and Riboux shortly. The main experimental conclusion (shown in Figure 2.11) is that the surrounding gas mostly affects the angle and the number of secondary droplets ejected, whereas the droplet size distribution and horizontal velocity are independent of the properties of the gas. By comparing with the semi-empirical model of Gordillo and Riboux, these results demonstrate the importance of the aerodynamic lift force exerted on the edge of the lamella during splashing, where this lift force is influenced primarily by the density of the ambient gas, followed by the viscosity, and finally by the mean free path.

Besides the influence of the properties of the gas and the liquid on the splashing outcome during a droplet-solid impact, experimental investigations have further established that the

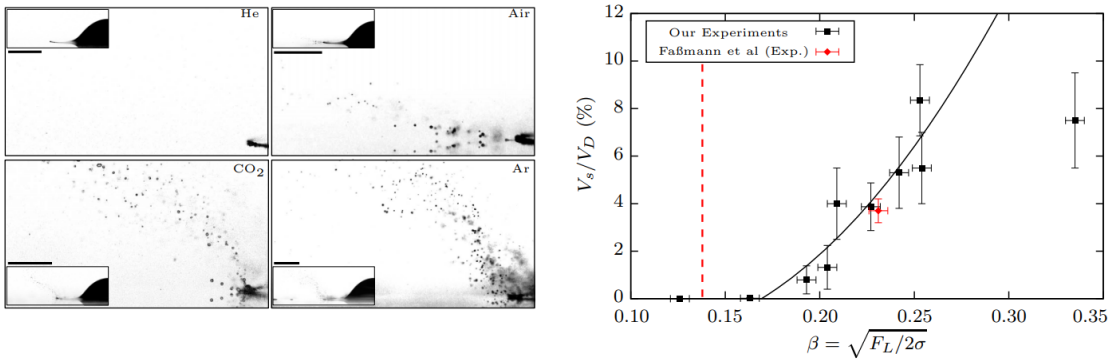

Fig. 2.11 Left: Dependence of total volume ejected on surrounding gas, with scale bars of length 500 μm. Top-left image is helium gas, top-right is air, bottom-left is CO_2, and bottom right is argon. Right: diagram showing the total ejected volume normalized to the primary droplet volume V_D over the splashing parameter β from the Gordillo-Riboux model[49, 20] .

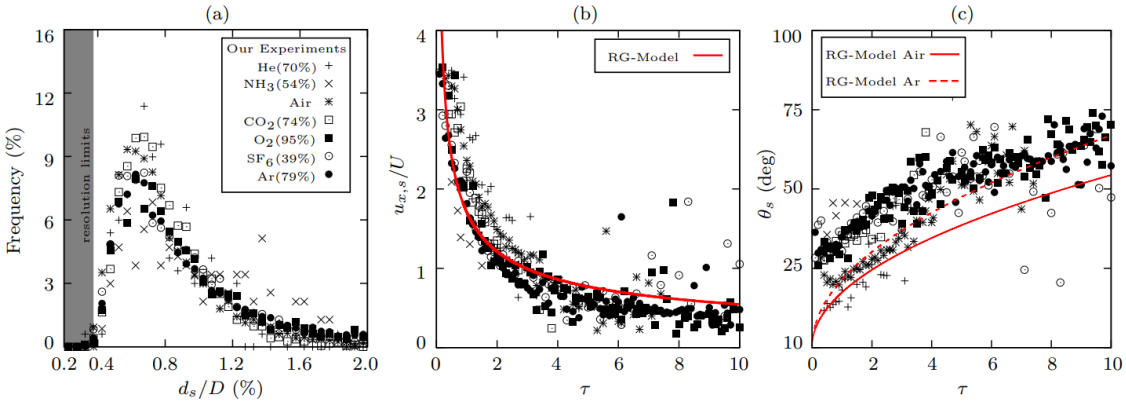

Fig. 2.12 Secondary ejected droplets. (a) shows the droplet size distribution, which is independent of the ambient gas. (b) shows the horizontal velocity as a function of the time, which is also independent of the gas. (c) shows the angle of the droplets relative to the surface as a function of time [49] .

roughness of the surface plays a role in producing a splash. To isolate the effect of surface roughness, Xu et al. [53] used helium gas at a low pressure of 13 kPa, much lower than the threshold pressure which is necessary to produce a corona splash. It was found that there are two contributions to splashing: a corona part caused by the presence of the gas and a prompt part caused by surface roughness (shown in Figure 2.13). This experimental result indicates that without the ambient gas, splashing is caused when the expanding liquid film of thickness d is destabilised by the roughness of the surface.

If the roughness is too small or the film is too thick, splashing does not occur. During the initial moment of impact, the expanding film thickness d is of molecular size (smaller than the mean free path of the gas) and increases in thickness as more liquid is added to the film during expansion. It follows that for small roughness $R_a = 5\mu$m, splashing should occur immediately after impact and be restricted almost entirely to this initial impact stage, whereas for large roughness $R_a = 78\mu$m, splashing occurs throughout the entirety of the film expansion, since d never becomes large enough to be perturbed by surface roughness. From the photographs in Figure 2.13, it was estimated that the liquid film thickness $d \sim 50$ μm at the point where the splashing stops at $R_a = 5\mu$m. This suggests a criterion for prompt splashing:

$$\frac{R_a}{d} = C(\mathrm{We}, \mathrm{Re}), \tag{2.12}$$

where $C(\mathrm{We}, \mathrm{Re})$ is a dimensionless number depending on both the Reynolds and the Weber number. For the impact conditions used in Figure 2.13 ($\mathrm{We} \approx 2400$ and $\mathrm{Re} \approx 11500$), it can be concluded that $C \sim 0.1$.

A key part of the droplet-solid impact which is observed empirically is that the liquid breaks up into many very small droplets after impact. Since the size distribution of the ejected droplets $N(r)$ might offer insight into the exact mechanism which intiates the interfacial instability during impact, Xu et al. [53] studied $N(r)$ for prompt splashing on rough substrates. The results (shown in Figure 2.14) indicate that the decay constant r_0 of the exponential decay in $N(r)$ as a function of substrate roughness R_a is approximately linear in the roughness for small values of roughness, but saturates for large values.

The experimental connection between splashing and surface roughness was investigated further by Hao [57], who found that a corona splash for the impact of a water droplet can be triggered by using a slightly rough substrate. The corona splash can then be suppressed to a prompt splash either by decreasing or increasing the surface roughness from this problem and that corona splashing always occurs on a rough substrate with $R_a = 9.16\mu$m if the impact speed is sufficiently high. The non-monotonic effect from the surface roughness can be reduced by lowering the surface tension of the liquid used for the droplet. If V_1 is defined to be the threshold speed below which the droplet spreads on the substrate and

V_2 is defined to be the threshold speed over which corona splashing occurs on impact, it was found that experimental values for V_1 on rough substrates above $R_a = 0.38\mu$m can be collapsed onto curves using both the Weber number and the splashing parameter, as can the values of V_2 on highly rough substrates above 2μm. This was not possible for other values due to the complex phenomenological effect which slightly rough surfaces have on droplet-solid splashing. Ashida et al. [52] performed experiments to confirm this effect and proposed that corona splashing may hide prompt splashing during an impact at atmospheric pressure on a smooth surface for low Ohnesorge numbers (Oh ≤ 0.01).

2.2.3 Mathematical Modelling

Although splashing of a droplet is a ubiquitous process, the physics involved is extremely complicated and there is no universally accepted explanation for the process or for the exact interplay between the properties of all three phases involved. The mathematical models which are used are generally semi-phenomenological in nature and in particular there is no agreed-upon proposal for the mechanism which causes a droplet to eject a liquid sheet during impact. One simple possibility is that the formation of the crown sheet is due to the compressibility of the fluid. At the moment of impact, there is a singularity due to the locally parabolic profile of the interface and this singularity causes the contact line to exceed the speed of sound. A shock wave develops as a result. If the contact line is below the speed of sound, the shock wave detaches away from the contact line and sheet ejection is observed [62–64].

Mani et al. [65] argued that this cannot be the explanation for the sheet ejection, since if the droplet is sufficiently small and travels at a speed below 1 ms^{-1}, the presence of the surrounding gas around the droplet should deform it and keep the speed of the liquid below the speed of sound, hence this is not a general explanation for the mechanism by which the liquid sheet is ejected during impact [66, 67]. Mani et al. [65] propose that splashing is a two-stage process, where the first stage causes formation of a liquid sheet which is separated away from the flat solid surface by a thin layer of air. This can be shown rigorously by solving the governing equations, which are the two-dimensional inviscid flow equations for the incompressible fluid

$$\rho_l \mathbf{u}_t + \nabla \pi = -\rho_l \mathbf{u} \cdot \nabla \mathbf{u}, \quad \nabla \cdot \mathbf{u} = 0 \quad \text{for } y > h(x,t) \tag{2.13}$$

and the Reynolds lubrication equation modified for a compressible gas [39]

$$12\mu(\rho h)_t - (\rho h^3 p_x)_x = -6\mu(\rho u h)_x, \quad \pi - p = \sigma\kappa \quad \text{at } y = h(x,t) \tag{2.14}$$

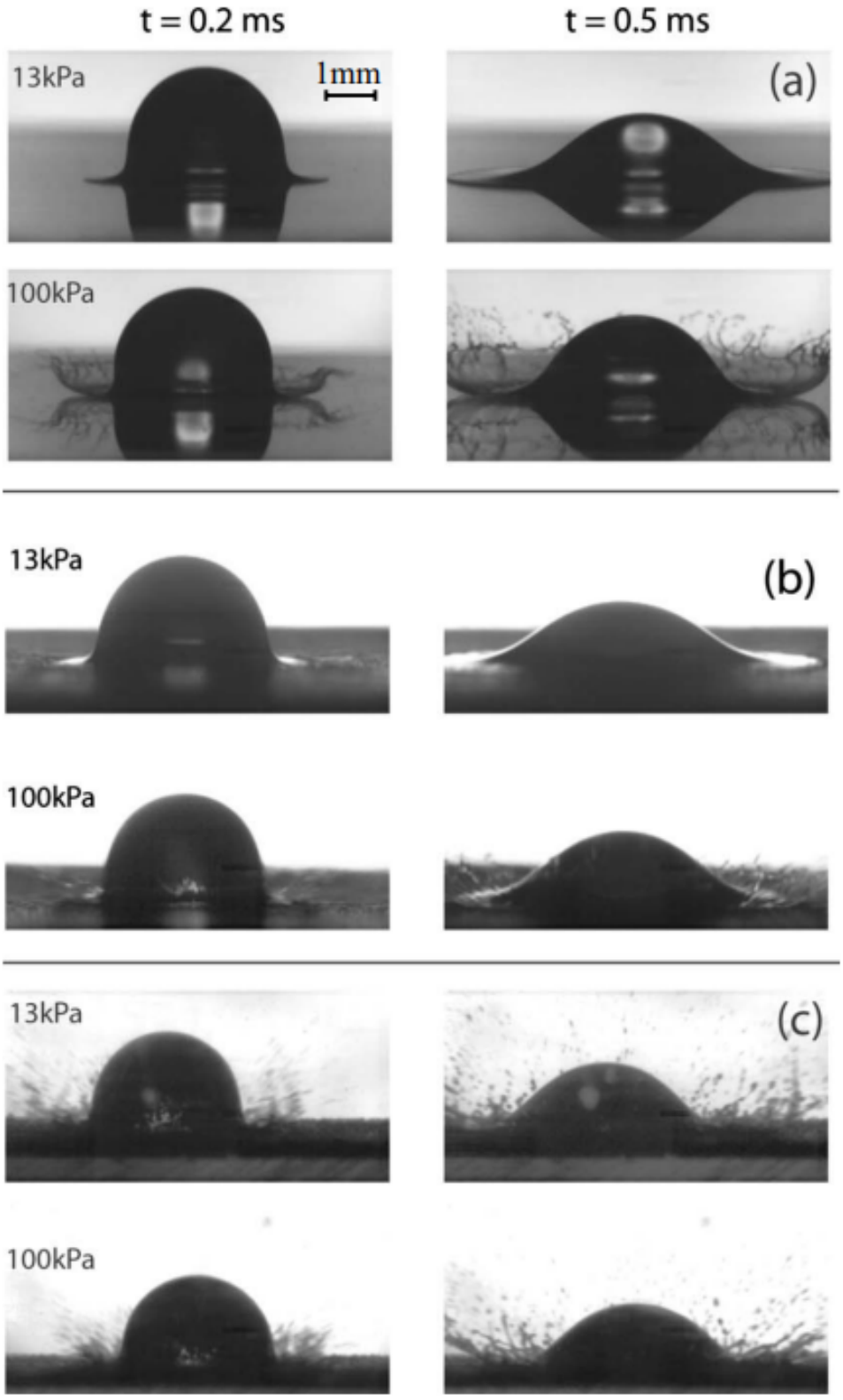

Fig. 2.13 Photographs of splashing as a function of gas pressure and surface roughness. (a) Splash on a smooth substrate which is a clean microscope slide. (b) Splash on a substrate with roughness $R_a = 5\mu$m. (c) Splash on a substrate with roughness $R_a = 78\mu$m [53] .

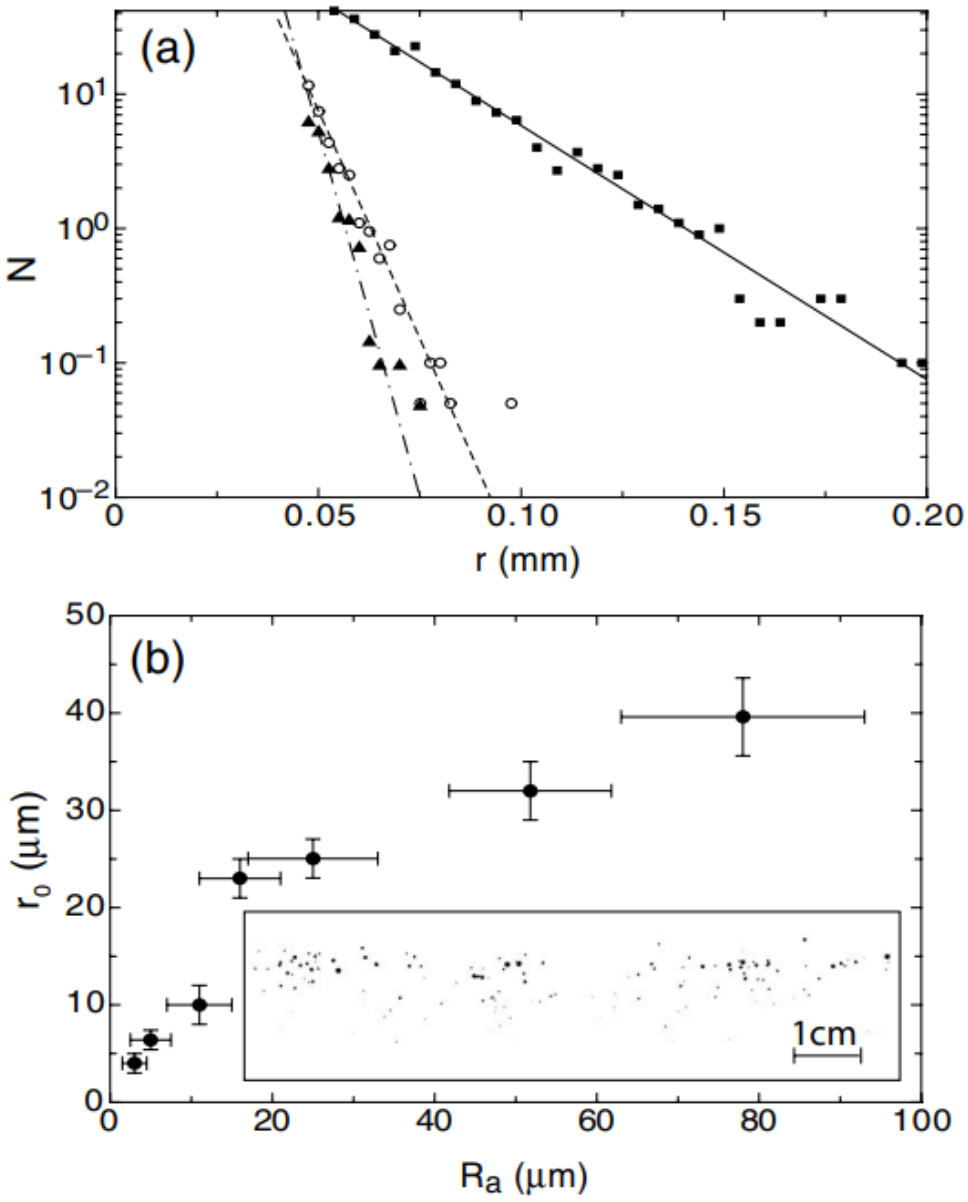

Fig. 2.14 The distribution of ejected droplets in a prompt splash on rough substrates. (a) $N(r)$ versus r for splashes on substrates with three values of roughness: $R_a = 16\mu$m , $R_a = 5\mu$m, and $R_a = 3\mu$m. (b) The decay constant r_0 of the exponential decay in $N(r)$, as a function of substrate roughness R_a. For small values of roughness, the decay constant is approximately linear in the roughness. At large roughness, the decay constant saturates. The sizes of particles on sandpaper are randomly distributed around an average value R_a. The fluctuation of particle sizes gives error bars for R_a and the standard deviation from exponential fitting gives error bars for r_0. [53] .

where π is the pressure field for the liquid, ρ_l is the density of the liquid, $y = h(x,t)$ is the height of the liquid interface, μ is the viscosity of the gas, p and ρ are the pressure and density of the gas, σ is the interfacial tension between the two fluid phases and κ is the interface curvature.

A detailed mechanistic model for the droplet splash which has been widely adopted was proposed by Gordillo and Riboux [18]. In this model, the threshold speed for splashing is determined using the fact that splashing occurs due to a vertical lift force on the edge of the liquid sheet from the surrounding gas. This lift force has two contributions: the lubrication force $\sim K_l \mu_g V_t$ and the suction force $\sim K_u \rho_g V_t^2 H_t$, where μ_g is the viscosity of the gas, ρ_g is the density of the gas, V_t is the initial velocity of the ejected lamella and H_t is the initial height of the lamella. K_l and K_u are coefficients which are derived from detailed calculations of the lift force in the region located between the lamella and the substrate (these calculations show that K_l is approximately equal to a sum of two terms which both depend on the mean free path of the gas).

The lubrication force captures the viscous contributions to the lift force on the lamella edge and the suction force captures the inertial forces. Note that viscosity is actually a mean free path effect, since changes in gas pressure do not change the viscosity of the gas. During the characteristic impact time, viscous effects are confined to thin boundary layers with a typical width much lower than the radius of the droplet R. Since the gas Reynolds number Re_g based on H_t and V_t as the characteristic scales is $\sim \mathscr{O}(10)$, both the viscous and inertial contributions to the lift force must be considered. The model recovers the expectation that at higher Weber and Reynolds numbers the dominant forces in the droplet splashing problem for a smooth dry surface are inertial in nature [18]. As a result of detailed calculations, Gordillo and Riboux found that there is a criterion which expresses the splash threshold velocity for a smooth flat dry surface as a certain function β:

$$\beta = \left(\frac{K_l \mu_g V_t + K_u \rho_g V_t^2 H_t}{\sigma} \right)^{1/2} \sim \mathscr{O}(1). \tag{2.15}$$

The critical speed for splashing can be determined from the condition

$$\beta = \sqrt{\frac{F_L}{2\sigma}}, \tag{2.16}$$

where F_L is the vertical lift force per unit length $F_L \sim \mu_g V_t$ on the edge of the expanding liquid sheet due to the gas lubrication layer.

This model has since been modified and improved. A key oversight in the original Gordillo-Riboux model is that the mechanism of sheet formation relies on the assumption of initial contact between the droplet and the solid surface, where the liquid sheet is ejected close to the point of impact. However, Mandre et al. [67] had previously argued that the

liquid does not initially make contact with the solid prior to impact and instead spreads on an extremely thin gas film. The droplet develops curvature, spreads on the air film and emits capillary waves. Riboux and Gordillo [19] accordingly modified the model of [18] by including the effect of the growth of the gas boundary layer which develops at the root of the ejected liquid sheet. It was found that depending on the value of the ratio δ/H_t, where δ is the thickness of the boundary layer and H_t is the initial thickness of the advancing rim, the time for ejection of the liquid sheet can be explicitly written down as a function of the Weber number, with the exact function depending on whether $\mathrm{Re}^{1/6}\mathrm{Oh}^{2/3}$ is below or above 0.25, where the Ohnesorge number Oh relates viscous forces to inertial and surface tension forces:

$$\mathrm{Oh} = \frac{\sqrt{\mathrm{We}}}{\mathrm{Re}} = \frac{\mu_L}{\sqrt{\rho_L \sigma L}} \tag{2.17}$$

Notably, this modified expression for the ejection time of the lamella has much better agreement with experimental measurements, vindicating the suggestion that the gas boundary layer must be taken into account to provide a fuller description of the droplet splashing phenomenon.

Making use of more recent experimental results due to Hao et al. [24], Gordillo and Riboux [20] later revisited the role of the gas lubrication force in the wedge region between the liquid front and the solid substrate in causing the edge of the liquid sheet to deflect upwards away from the solid. It was demonstrated that the magnitude of the gas lubrication force is limited both by the slip length l_μ at the gas-liquid interface and the slip length l_g at the solid, which is proportional to the mean free path. The splashing regime was shown to change depending on the ratio l_μ/l_g, which explains the fact that splashing re-enters in the droplet splashing problem at low gas pressures (there is a transition from spreading to splashing and then back to spreading). We will later show that we do not observe such re-entrant splashing in our sphere impact experiments in the parameter range which we use. This analysis produces an expression for the threshold speed which depends on the inclination angle of the substrate, the droplet radius, the properties of both the liquid and the gas, and in particular the mean free path of the gas.

In this most recent model, it is argued that lift-off of the droplet away from the solid substrate should occur when the lift force exceeds the force due to surface tension, which leads to the requirement that

$$\frac{K_L \mu_L U}{\gamma} > K, \tag{2.18}$$

which implies that

$$K_L \mathrm{Ca} > K, \tag{2.19}$$

where Gordillo and Riboux estimate the constant K to be 0.034. We will see that this is roughly similar to the scaling which can be used for the sphere impact. All of the gas dynamics are hidden in the parameter K_L which depends on the dynamics of the lubrication gas film. Gordillo and Riboux also have simplified expressions for K_L depending on whether the mean free path is larger or smaller than the viscous boundary layer at the free surface. It should be emphasised that, although it has been widely applied, the model of Gordillo and Riboux [20] is only for smooth surfaces and that work on the detailed influence of surface roughness on droplet-solid splashing is still mostly at an experimental or phenomenological stage [69].

The Gordillo-Riboux model [18] has since been expanded by Pierzyna et al. [21] using a data-driven threshold model which re-defines the threshold for droplet splashing on a dry smooth surface by collating a large number of experimental sources with different conditions and analysing the data with an uncertainty qualification analysis combined with machine learning . The Gordillo-Riboux model can be considered as the special case where the parameter β for determining splashing is a constant (in the general case, each impact parameter has a different dependence on β). This more detailed threshold model incorporating a large number of diverse experimental results observed a linear dependence of the splashing threshold β on impact speed V, surface tension σ and gas density ρ_g and an inversely proportional relation between β and the liquid viscosity μ_l. This new model exhibits only weak dependency on the radius of the droplet R, liquid density ρ_l, gas viscosity μ_g and the mean free path of the gas λ_g. These dependent variables are eliminated by a recursive feature elimination process to leave the four impact conditions mentioned above. The eliminated variables are only irrelevant in the sense that they are irrelevant beyond the expression for β. The Gordillo-Riboux model captures all the influence of the eliminated variables on the splashing parameter such that they are not needed for any further corrections.

2.3 Sphere-Liquid Impacts

We now move on to the final scenario mentioned in the work of Worthington and Cole: that of a solid sphere impacting a liquid body [1]. As with the droplet-liquid and the droplet-solid impacts, this problem and many variants of it have been studied very intensively both on the experimental and the theoretical side, with much interest coming from the applications in ballistics, impact reduction on ships and seaplanes. Biological applications of solid–liquid impacts include locomotion of water walkers and insects at air–water

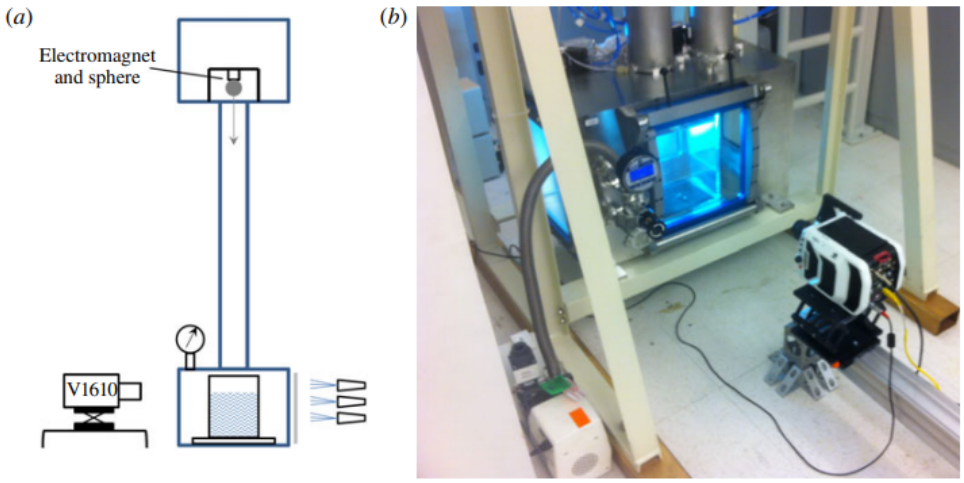

Fig. 2.15 (a) Schematic of the experimental apparatus and (b) photograph of the lower chamber, showing position of the camera, backlighting, liquid container in the chamber, vacuum pump and pressure gauge [3] .

interfaces, where it is known that some large water walkers such as basilisk lizards and certain types of shore bird use inertial forces generated by impact of the driving leg on the liquid surface to support their weight [70]. The dynamics of cavity closure is also relevant for insects and animals which penetrate liquid surfaces at high speed in search of prey [71].

2.3.1 Experimental Set-up

A typical experimental set-up is used by Marston et al. [3] (shown in Figure 2.15). The experimental apparatus consists of two main chambers connected by cylindrical tubes. The target liquid container is placed in the lower chamber and the sphere release mechanism, consisting of an electromagnet and a positioning stage, is placed in the upper chamber. Once sealed, a vacuum pump is used to reduce the ambient pressure inside the chamber down from 101 kPa (atmospheric pressure) to 6.3 kPa (1/16th atmospheric pressure), with the pressure being read by a pressure gauge connected to the lower chamber. The sphere is released by switching off the electromagnet outside the chamber, allowing the sphere to fall freely under gravity. The impact dynamics are captured by a high-speed video camera, with the recordings being triggered manually and saved to a PC for later analysis. In other versions of this basic experimental set-up, the ambient gas pressure is not varied and one instead varies the properties of the solid sphere [72].

2.3.2 Results

The range of experimental results which has been obtained in the literature on sphere-liquid impacts is extremely wide and diverse. We will provide a small list of examples to give an idea of this range. Aristoff et al. [73] considered buoyant low-density spheres, finding expressions for the pinch-off time of a cavity and the volume of air entrained by the sphere. Hurd et al. [74] and Yang et al. [75] studied the water entry characteristics of deformable elastomeric spheres, finding that the elasticity of the sphere can affect the splash formation and that the oscillations of these spheres during impact results in new types of nested cavities. Watson et al. [76] examined spheres with heterogeneous wetting properties, finding that spheres which are partly hydrophilic and partly hydrophobic always have asymmetric cavities and drift away from straight-line trajectories. Marston et al. [77] observed cavity formation for heated sphere impacts, finding that there is an inverted Leidenfrost effect when the sphere temperature is much larger than the boiling point of the liquid, which either produces a cavity with smooth walls or a double cavity structure. Impacts of heated spheres were studied further by Jetly el al. [78], who found that the vapour layer on the surface of the sphere can greatly reduce the hydrodynamic drag on the sphere due to an early drag crisis transition. Mansoor et al. [79] also studied super-hydrophobic spheres and used a splash-guard mechanism to eliminate the phenomenon known as surface seal. Related studies have considered projectiles with varying aspect ratios, impacts on a two-phase fluid and non-axisymmetric cavities created by impact of discs [80–83]. A review of many more variants of the problem may be found at [84].

If we restrict to a one-phase liquid body and standard rigid spheres, the experimental results which are relevant for our work can be split roughly into those which consider the influence of the properties of the gas and the liquid on the splash, jet and cavity phenomena which accompany the impact and those which focus on the properties of the solid. The first important results on the properties of the gas were obtained by Gilbarg and Anderson [4], who studied the influence of the atmospheric pressure on cavity formation for spheres impacting the surface of a body of water at impact speeds between 3 and 30 ms^{-1}. It was observed that for an impact of a 25.4 mm steel sphere at speed 21.3 ms^{-1} and atmospheric pressure, the surface ejected above the point of impact closes early, preventing further growth of the cavity and occurrence of a deep closure (shown in Figure 2.16).

On the other hand, for impact of a 25.4 mm steel sphere at speed 21.3 ms^{-1} and ambient pressure of 25 kilopascals, a long closed cavity trails the sphere after deep closure. Jets were found to occur for both surface and deep closures of the cavity. Gilbarg and Anderson [4] note that it is the density of the gas, not the pressure, which is the active agent involved. If we assume potential flow, the pressure on the liquid dome above the surface after impact is essentially equal to the Bernoulli pressure $\frac{1}{2}\rho_g V^2$, where ρ_g is the density

of the gas and V is the impact speed of the projectile. Increasing the gas pressure increases the gas density by the ideal gas equation, and increasing either the gas density or the speed of the sphere increases the Bernoulli pressure, which decreases the time needed to close the surface up into a dome, at which point the cavity cannot grow further in size. With surface closure, further air passage into the cavity ceases, so that expansion is inhibited by the under-pressure in the cavity, resulting in a smaller cavity size and an earlier deep closure.

The results of Gilbarg and Anderson were extended by May [5] and Yakimov [6]. May provided a more detailed study of the effect of several experimental parameters on the time and place of occurrence of various events over the lifetime of the cavity, including both pressure and the density of the ambient gas. Only impact speeds above 7.9 ms^{-1} were considered, since at speeds below 6 ms^{-1}, surface forces become important. May established that the time for deep seal of cavities and depth of deep seal are functions of entry speed and air density. Graphs of time for surface seal against speed were plotted using two different gases (air and a mixture of Freon and water vapour) with the same density, but only one-sixth of the pressure in the latter case. The graphs were found to agree within experimental uncertainties, providing evidence that the most important property of the gas which influences the surface seal is the density, not the pressure.

However, although May attributed the early surface seal at atmospheric pressure to a region of low pressure caused by air flowing into the cavity, the Bernoulli pressure at both atmospheric pressure and one-sixteenth atmospheric pressure gives values of under-pressure which are small in comparison with the ambient pressure, so a theoretical reason was not provided for the closure of the cavity [3]. Marston et al. [85] performed related experiments with the ablation of a free liquid surface excited by a focused laser pulse to form a very thin cone-shaped sheet. It was observed that the liquid sheet always seals and domes over, even at the lowest pressures of 3.8 kPa. At reduced pressures, the sheet evolution developed interference fringe patterns which can be used to determine the thickness of the ejected liquid sheet by comparing with the opening speed of rupture.

Abelson [86] performed measurements with underwater probes showing that the theoretical under-pressure in the cavity region due to the Bernoulli effect underestimates the true pressure drop by a factor between 15 and 20. Lee et al. [87] provided an analytic model which specifies the energy transfer for cavity production as being equal to the energy dissipated by velocity-dependent drag on the sphere. The model for the cavity dynamics indicates that the Bernoulli pressure would need to increase by a factor of 50 to be able to theoretically explain observations of time for surface closure observed by Gilbarg and Anderson [4]. Figure 2.19 shows the general picture for the cavity following a sphere beneath the free surface, where it can be seen that air flows into the cavity with speed V_0.

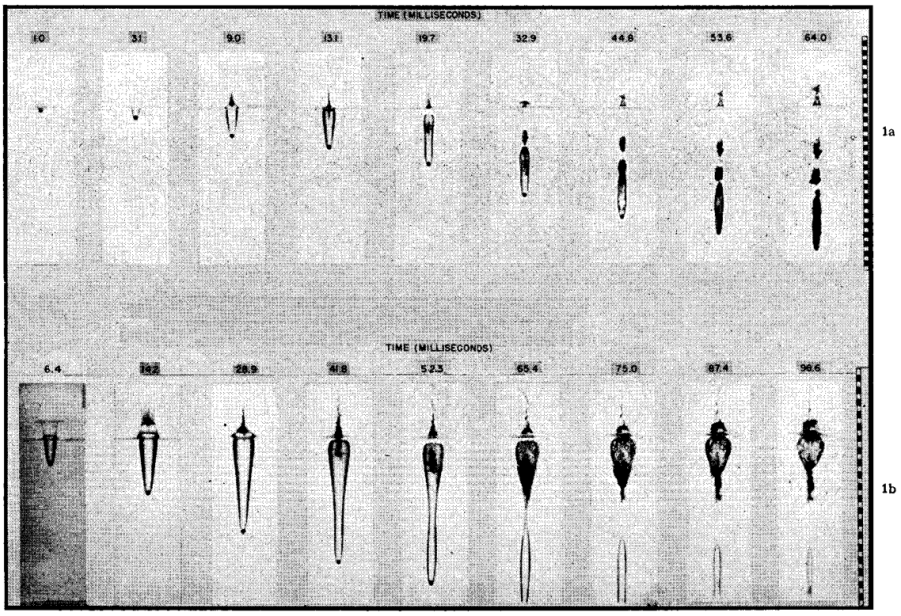

Fig. 2.16 (1a) Impact of a 25.4 mm steel sphere at speed 21.3 ms^{-1} and atmospheric pressure. The domed surface above the point of impact closes early, preventing further growth of the cavity and occurrence of a deep closure. (1b) Impact of a 25.4 mm steel sphere at speed 21.3 ms^{-1} and ambient pressure of 25 kilopascals. A long closed cavity trails the sphere after deep closure [4].

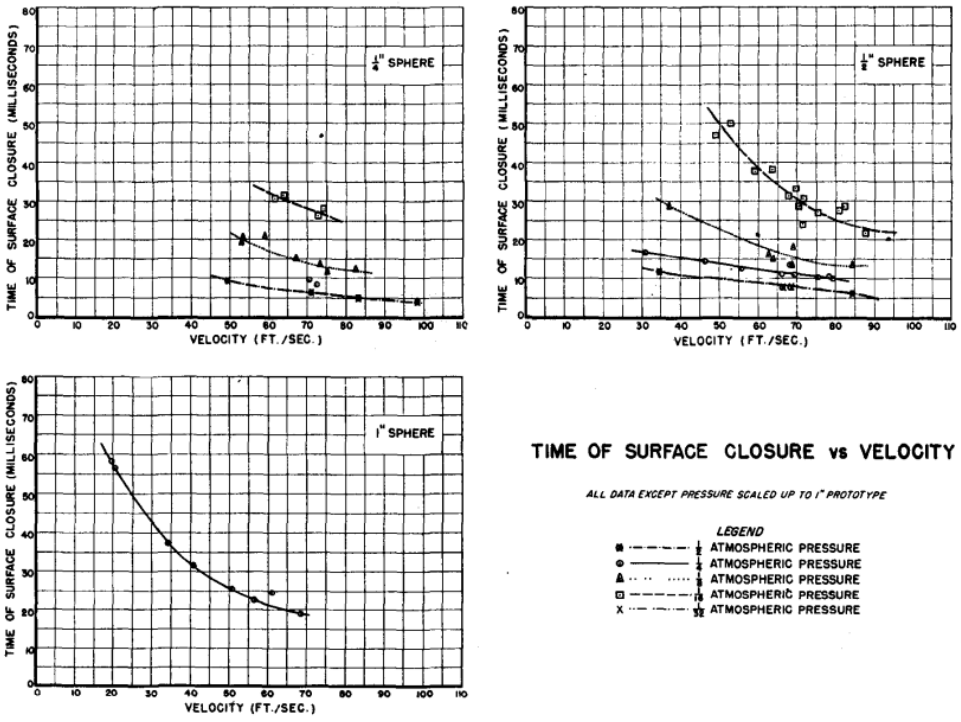

Fig. 2.17 Plots of time for surface closure vs velocity for spheres with diameters 6.35 mm, 12.7 mm, and 25.4 mm [4].

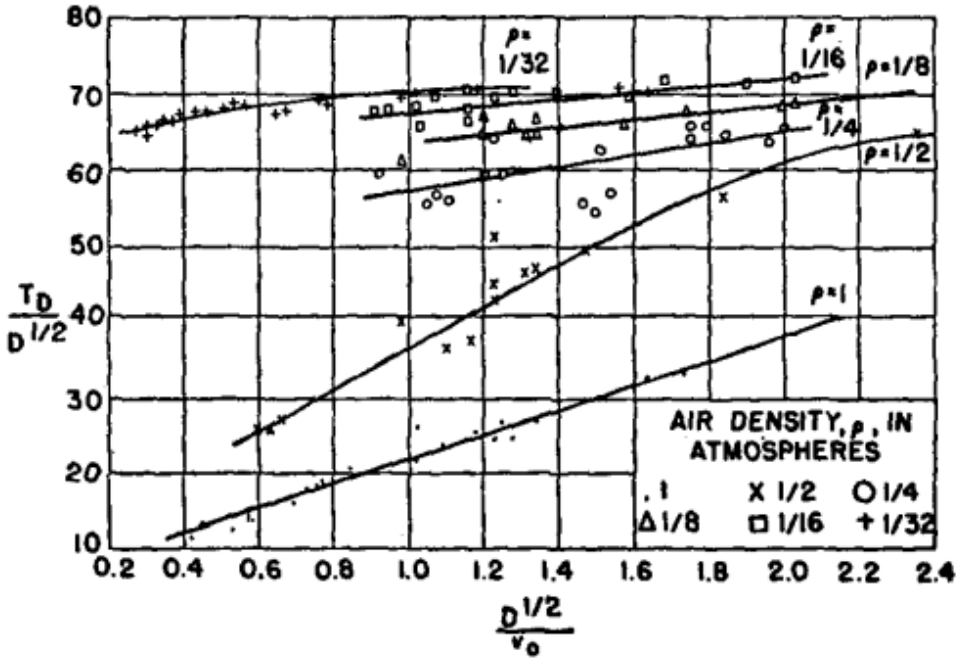

Fig. 2.18 Time for deep seal of cavities formed by 12.7 mm steel spheres, showing dependence on entry speed and air density [5].

Marston et al. [3] showed that the surface tension of the liquid plays an additional role in closure of the crown splash, for both low and high impact speeds. The sheet liquid thickness δ must be taken into account as the relevant length scale for the problem by constructing a sheet Weber number $\mathrm{We}_s = \rho_l \delta V_s^2/\sigma$, where V_s is the sheet velocity. Detailed images of the crown evolution and closure under reduced ambient pressures were also provided, showing that the crown has a buckling instability, whereby the thin films in between the thick vertical striations in the crown are more susceptible to pressure differentials across and are drawn inwards first. It was established that crown sealing features at atmospheric and 1/16th atmospheric pressures were similar and that surface tension must play a significant role in the closure of the crown. This was confirmed by comparing splash crowns with water for splash crowns with perfluorohexane, a liquid with a low surface tension of $\sigma = 11.9$ mN m^{-1}. In Figure 2.20, the influence of both the ambient pressure and surface tension are shown on the growth and collapse of the neck of the splash crown. Once the collapse begins, the rate of collapse is independent of the pressure, indicating that the collapse is driven mostly by surface tension, whereas surface seal is driven by both surface tension and pressure effects [88].

In the previous paragraph, we indicated that properties of the liquid strongly influence the collapse of the splash crown due to buckling instabilities. Given that the properties of the substrate play a role in the outcome of droplet-solid splashing, one might ask if

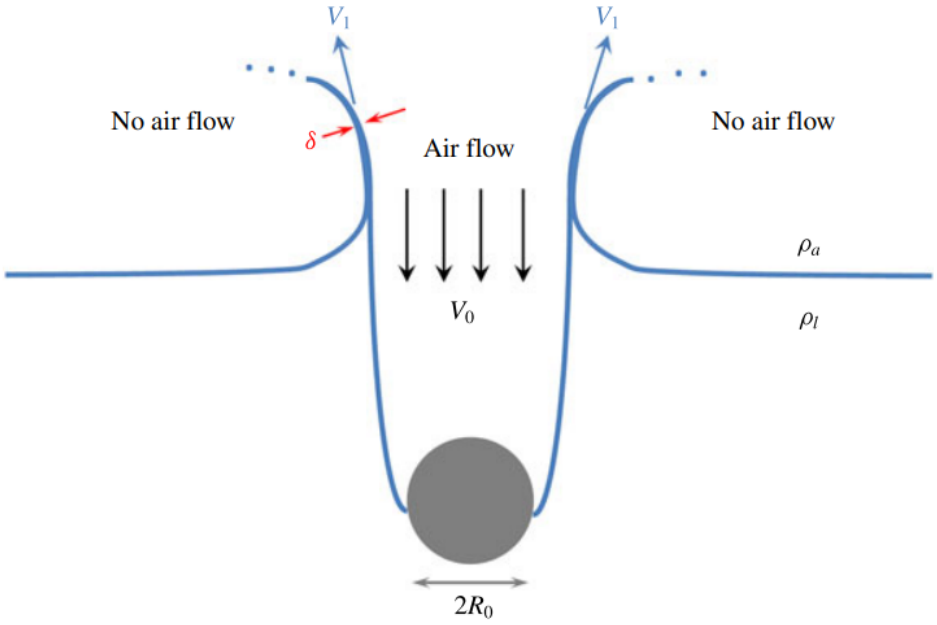

Fig. 2.19 Schematic of air flow into the cavity, where V_0 is the speed of the air flow, V_1 is the upward speed of the ejected liquid, and δ is the sheet thickness [3] .

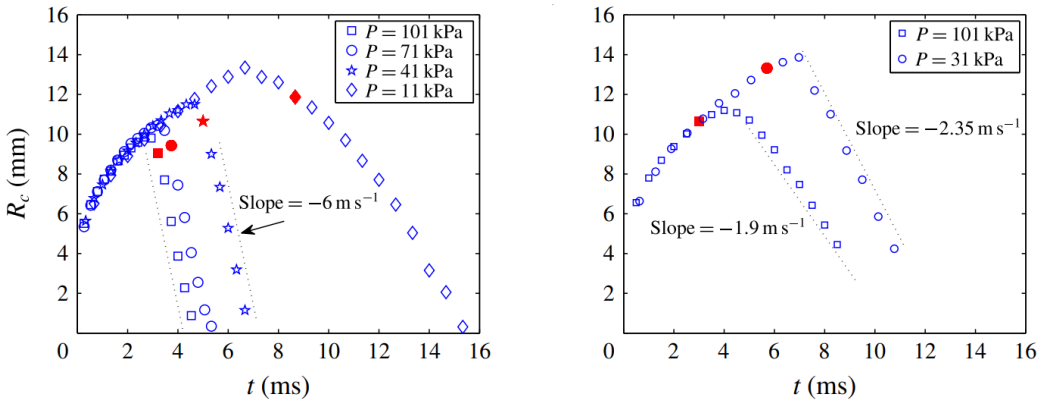

Fig. 2.20 Left: Growth and collapse of the neck radius for water with Re $= 5 \times 10^4$. Right: Growth and collapse of the neck radius for perfluorohexane with Re $= 7.77 \times 10^4$. Red symbols indicate the time and location of the minimum radius when pronounced buckling becomes visible [3] .

the properties of the sphere also play a role in the fate of the cavity which forms during impact. Duez et al. [89] found that cavity formation can be suppressed completely below a threshold speed U^* which is a function of the advancing static contact angle θ, where the contact angle is defined to be the angle with which the liquid-gas interface meets the solid surface. For example, hydrophilic spheres ($\theta < 90^\circ$) form cavities above a threshold speed $U^* \approx 7.2$ ms^{-1}. The threshold speed decreases for hydrophobic spheres ($\theta > 90^\circ$) and vanishes in the limit as θ goes to 180°. This is explained theoretically in terms of the stability of the contact line of the splash crown which forms around the circumference of the sphere during impact.

In more detail, this theoretical argument begins with a balance of the classical hydrodynamic forces, which shows that the splash crown separates at a critical capillary number Ca* obeying

$$\mathrm{Ca}^* \approx \frac{\Theta_0^3}{9l}, \tag{2.20}$$

where Θ_0 is the static contact angle defined with respect to the gas (wetting) phase and l is between 15 and 20. Using the fact that $\Theta_0 = \pi - \theta_0$, this can be rewritten as

$$\mathrm{Ca}^* \approx \frac{(\pi - \theta_0)^3}{9l}. \tag{2.21}$$

The classical reasoning of von Kármán and Wagner neglects dissipation in the liquid phase, so a contribution at the triple line due specifically to the dynamic viscosity of the gas must be included. This is given by

$$F_L \approx Cv\mu_L \tag{2.22}$$

where C is approximately equal to 1 and v is the speed of the triple line, which is proportional to the speed of the impacting sphere. Using the expression for the frictional force, the critical speed v^* is found to be

$$v^* = \frac{g_0}{9l}\frac{\gamma_{LV}}{\mu_L}(\pi - \theta_0)^3 \tag{2.23}$$

where g_0 is of an order between 5 and 10. However, the triple line speed v is assumed to be proportional to the speed of the impacting sphere U, so one has $v = \zeta U$, where ζ is a numerical pre-factor which might depend on the static contact angle θ_0. Using this, we have

$$U^* = \frac{g_0}{9l\zeta}\frac{\gamma_{LV}}{\mu_L}(\pi - \theta_0)^3 \tag{2.24}$$

This prediction was found to be in very good agreement with experimental data on non-wetting spheres which have a static contact angle $\leq 90^\circ$.

In the case of a hydrophilic sphere, the triple line still disappears as the dynamic contact angle goes to 180°, but an analytic result does not exist for the dynamic contact angle in this case. Since the physics is qualitatively similar, Duez et al. assume that for a hydrophilic sphere, the threshold speed for cavity formation U^* is given by

$$U^* \approx \zeta \frac{\gamma_{LV}}{\mu_L}, \tag{2.25}$$

where γ_{LV} is the liquid-vapour surface tension. In this case, ζ is only expected to have a weak dependence on θ_0 but since the dynamic contact angle at which destabilisation occurs (ie. around 180°). This is also confirmed by experimental data, where there is no appreciable dependence of U^* on the static contact angle once θ_0 goes below 90° (see Figure 2.21). One notices from both expressions that regardless of whether the sphere is wetting or non-wetting, the threshold speed for cavity formation is proportional to the surface tension and inversely proportional to the liquid viscosity. This qualitatively matches the conclusions found for the droplet splashing problem, since increasing the viscosity of the liquid makes it easier to form a splash [17].

The presence of the viscosity in an expression for threshold speed determining cavity formation might initially seem surprising, since in the classical work of von Kármán [7] and Wagner [8], it was reasoned that one could neglect the presence of the viscosity of the liquid because of the large values for the Reynolds and Weber numbers. In a sphere impact problem, Re is typically of order between 10^4 and 10^5 and We is of order between 10^3 and 10^4, so one would expect that the influence of the surface tension and the liquid viscosity would only play a negligible role in deciding whether a sphere splashes or not.

However, we may also compare the ratio of the inertial forces within the gas $\rho_g UL$ to the inertial forces within the liquid $\rho_l UL$, where L is a characteristic length scale and U is the flow speed. In a multi-phase system, L is the same in both cases and the flow speed U can be taken to be the same, so the ratio of the gas inertia to the liquid inertia simplifies to the ratio of the densities ρ_g/ρ_l. This is a dimensionless number which indicates the importance of the density of the gas, so we expect this ratio to play a role in any estimates which argue that the gas density can influence the outcome of a sphere impact on a liquid body in the presence of ambient gas. Regarding the presence of the gas, a major qualitative conclusion of Duez et al. [89] is that changing the pressure of the gas has no influence on whether a cavity forms (this was also confirmed experimentally). Again, this seems like a startling conclusion, given the similarity with the droplet-solid impact where it is known that the ambient gas plays a crucial role in determining the outcome of splashing.

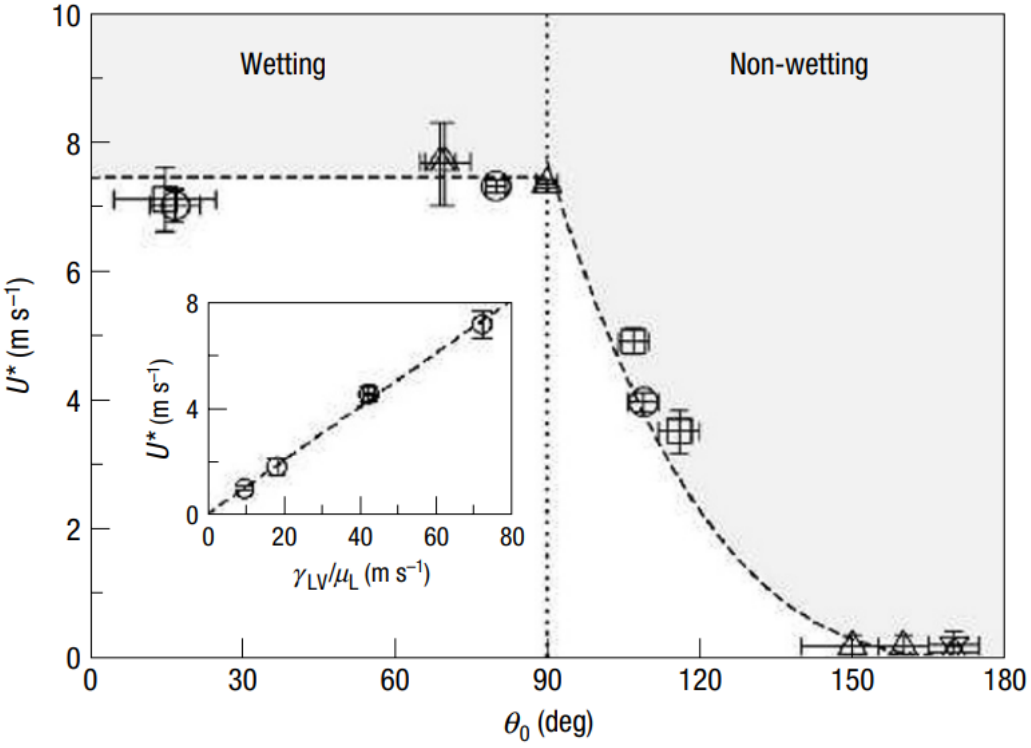

Fig. 2.21 Threshold speed U for cavity formation as a function of (advancing) static contact angle θ_0 of the smooth impacting sphere. The dashed lines are the theoretical predictions based on relations (2.23) and (2.25). The shaded area is the regime where a cavity forms. The different symbols correspond to different sphere diameters and materials —square: 25.4 mm (glass); down-triangle: 20 mm (aluminium); circle: 15 mm (glass, steel); up-triangle: 7 mm (aluminium, steel). Inset: Dependence of the threshold speed for a wetting glass sphere (25.4 mm) on the ratio γ_{LV}/μ_L. Several liquids were used for the inset plot (water, isopropanol, ethanol and a water-glycerol mixture with 20% glycerol). The contact angle for these liquids was always below 10° [89] .

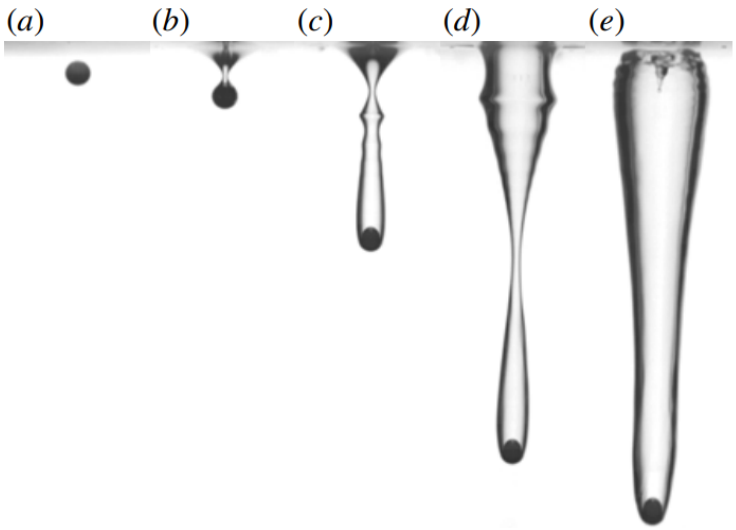

Fig. 2.22 Impact of a 2mm sphere on a body of water. (a) $\theta = 101^\circ$ and the sphere impacts at 4.43 ms^{-1}. (b)-(e) the sphere has a contact angle $\theta = 141^\circ$ and impacts with speeds 0.24 ms^{-1}, 1.40 ms^{-1}, 2.80 ms^{-1} and 4.43 ms^{-1}, forming quasistatic, shallow, deep and surface seal cavities, respectively [72].

Aristoff and Bush [90] studied sphere-water impacts with fixed contact angle $\theta 120 \pm 5^\circ$ and found distinct types of cavity (shown in Figure 2.22) which can be defined by their collapse or the pinch-off location. Each of these cavities occurs in a regime diagram where the Weber number is plotted against the Bond number (shown in Figure 2.23). At the lowest Weber numbers, one has quasi-static cavities, which pinch-off occurs just below the surface of the liquid. Shallow seal occurs at higher We and lower Bo, where surface tensions dominates and the depth of pinch-off is of the order of the capillary length. Deep seal occurs at higher We and higher Bo, where gravitational forces dominate and pinch-off occurs halfway between the free surface and the sphere. Surface seal was described by Marston et al. [3] and occurs at the highest Weber numbers. As outlined above, in this scenario a splash crown is created on impact and collapses inwards due to the combined influence of air pressure and surface tension, sealing at the liquid surface. A theoretical model was also developed to describe the evolution of the cavity shape, which provides exact solutions for the evolution of the cavity and simple expressions for the pinch-off time and cavity depth.

The foundational analysis of Duez et al. [89] and Aristoff and Bush [90] was extended by Speirs et al. [72], who created cavity regime diagrams for four different contact angles, finding that the regimes can be predicted for various impacting bodies (spheres, multidroplet streams and jets) using the cavity diameter d_c and cavity speed U_c to define cavity Bond and Weber numbers Bo_c and We_c. At low We, a slow-moving thick rim forms around the sphere, which allows air to entrain behind the sphere, forming a small cavity.

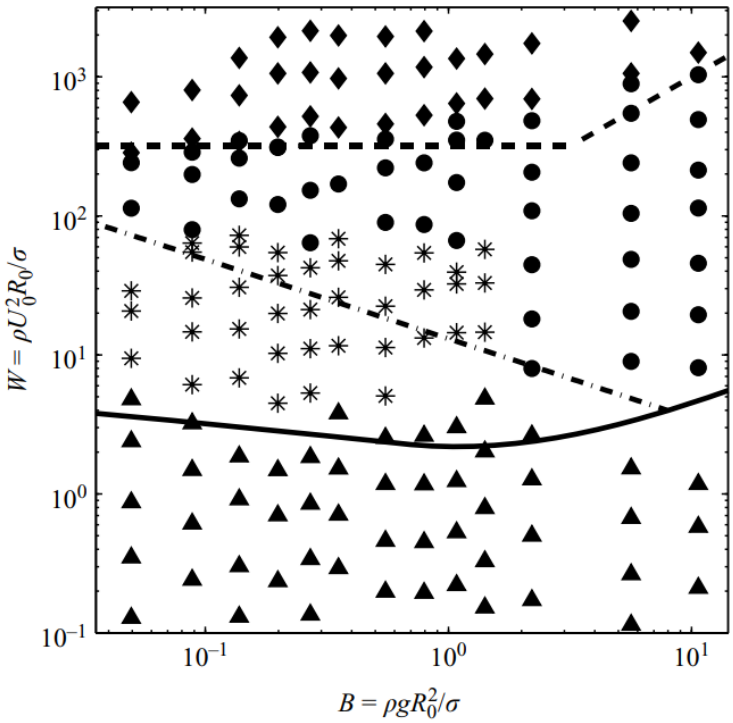

Fig. 2.23 . Regime diagram indicating the dependence of the observed cavity type on Bo and We for advancing contact angle 120°. The triangle, asterisk, circle and diamond symbols denote the quasi-static, shallow seal, deep seal and surface seal regimes, respectively [90].

At higher We, the crown thins and adheres to the sphere, meeting at the top of the sphere prior to submergence so that no cavity forms. Once the threshold speed is exceeded, the splash crown separates from the sphere and forms the familiar classical cavities discussed. The boundaries between these regimes were defined by formation of a splash crown, which was shown to be independent of the contact angle for $\theta = 86^\circ$ and 101°. For hydrophilic or slightly hydrophobic spheres, splash crown formation and adherence to the sphere decreases the cavity sizes, leading to quasi-static and shallow seal cavities.

2.4 Contact Line Pinning

Cavity formation for impacts of spheres on liquids is accompanied by pinning of the contact line to the sphere (shown in Figure 2.24). In most cases, the line pins to the equator of the sphere. Note that in certain cases, cavities may form without the presence of a contact line (impacts of superheated spheres, for example) [77]. Snoeijer and Andreotti [91] noted that the striations in the walls of a cavity also extend to the splash crown and that they are an artefact of the contact line pinned around the equator of the sphere, which has a jagged, saw-tooth apperance which can be distinguished in Figure 2.24. Marston et al. [3] observed that this contact line saw-tooth formation persists until the buckling instability is seen above the free surface. The striations provide favourable locations for the buckling around the circumference of the splash crown. The buckling instability was found to appear in all crown sealing events across different timescales (including impacts of superheated spheres), but is intensified by the pinning of a contact line.

Models of moving contact lines on smooth solid surfaces have been proposed by various authors, including Shikhmurzaev [92], Billingham [93] and Ding et al. [94]. Contact line pinning is distinct from the connection which had already made by Duez el al. [89] between contact line motion and splashing, who reasoned that splashing is caused by detachment of the liquid film which wets the surface of the sphere and that detachment occurs when the interface moves faster than the maximum permissible speed of the contact line, which is of order σ_L/μ_L. This accounts for splash crown formation during early impact times, but at late times after initial impact, the cavity line eventually pins to the equator of the sphere and stops travelling.

Ding el al. [94] considered the question of why a contact line which is initially in motion should pin to the surface and whether the geometry of the impacting body would influence the pinning. It was found that the balance of forces between the viscous stress and the Laplace pressure leads to pinning of the contact line, which further induces a cavity, with the contact line always stopping on the equator of the sphere as the cavity begins (shown in Figure 2.25). This force analysis connects the bending of the interface

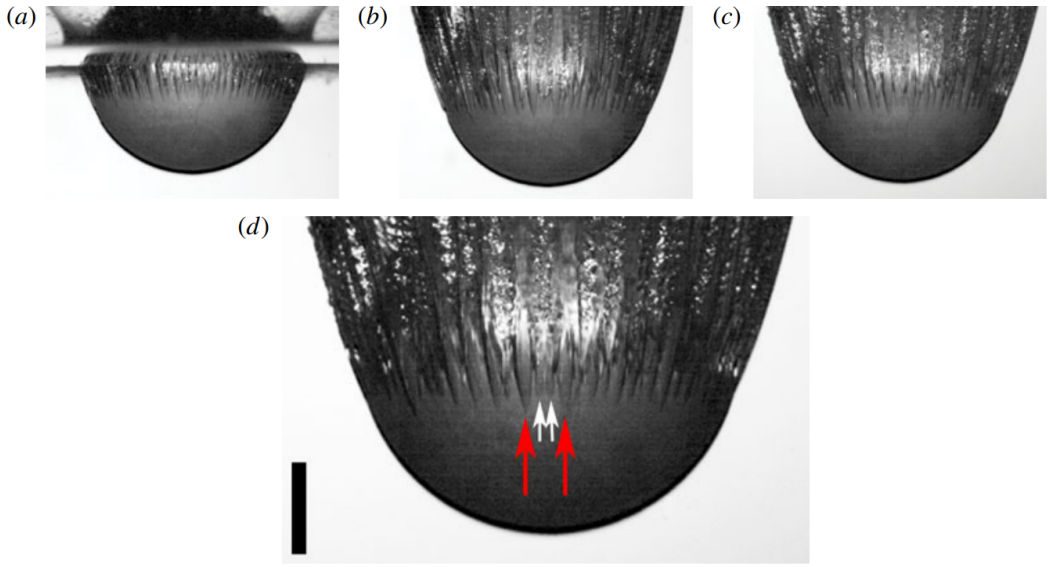

Fig. 2.24 Contact line formation during water entry of a 20 mm sphere. The times from impact and depth of the bottom of the sphere below the free surface are (a) $t = 1.4$ ms, $z = 13.9mm$, (b) $t = 2.2$ ms, $z = 21.8$ mm, (c) $t = 3.8$ ms, $z = 37.5$ mm. (d) Enlarged view of contact line formation, where red arrows indicate the southernmost pinning points and white arrows indicate intermediate pinning points [3].

α, the contact angle, the position of the contact line ϕ, and the size of the steady liquid eddy attached to the contact line l_s with the Weber number. It was found that as the Weber number is increased, the position of the pinned contact line moves upwards towards the equator of the sphere (shown in Figure 2.26).

In simulations of Yang et al. [95], a thin gas film was found between a hydrophobic sphere and a liquid body just prior to impact. It was suggested that the generation of this gas film could affect the formation and evolution of the cavity. After the gas film ruptures at the bottom of the sphere, it was found that a moving contact line is generated which retracts along the surface of the sphere, where the speed of retraction is generally proportional to the inverse square root of the time. In these simulations, it was confirmed that in all cases the moving contact lines eventually pins just above the equator. This is shown in Figure 2.27, where the speed of the moving contact line U as a function of dimensionless time T_C reaches a turning point where it starts to decrease steeply, corresponding to the fact that the contact line has pinned to the equator of the sphere.

In related experiments, Marston et al. [96] found that a falling sphere entraps a small amount of air at the south pole due to the air pocket which forms because of the lubrication pressure in the gas layer between the sphere and the liquid surface. This phenomenon is due to the air pocket which forms because of the lubrication pressure in the gas layer between the sphere and the liquid surface prior to impact. As the liquid surface deforms, a

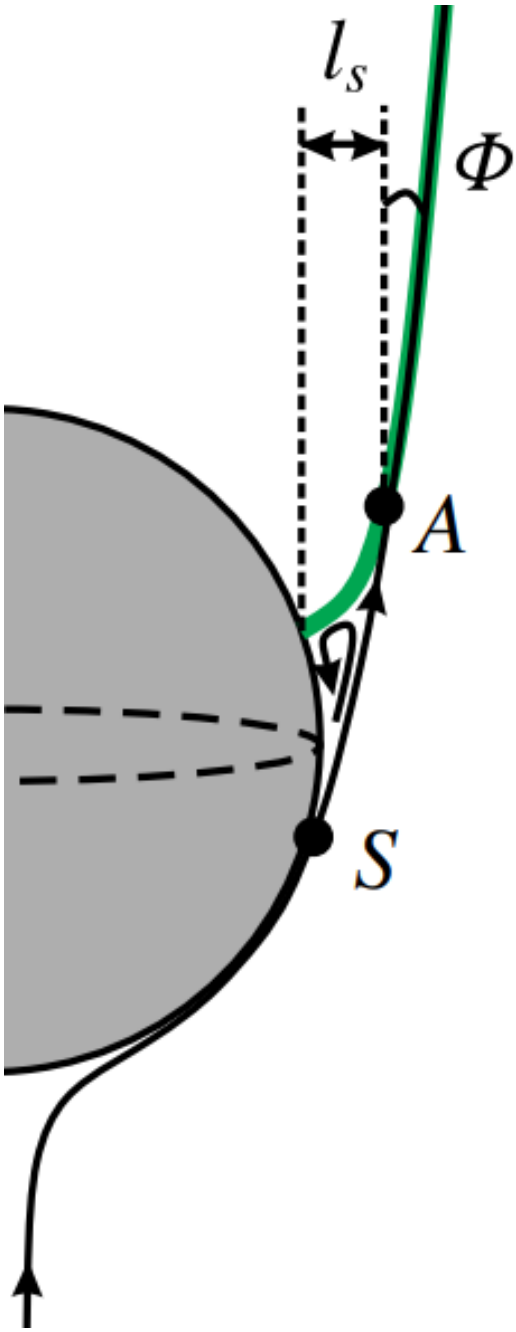

Fig. 2.25 Sketch of the characteristic flow patterns for a sphere. The black curve with arrows is the surface streamline which starts at the symmetry axis and merges with the interface (the green curve) at the point A [94].

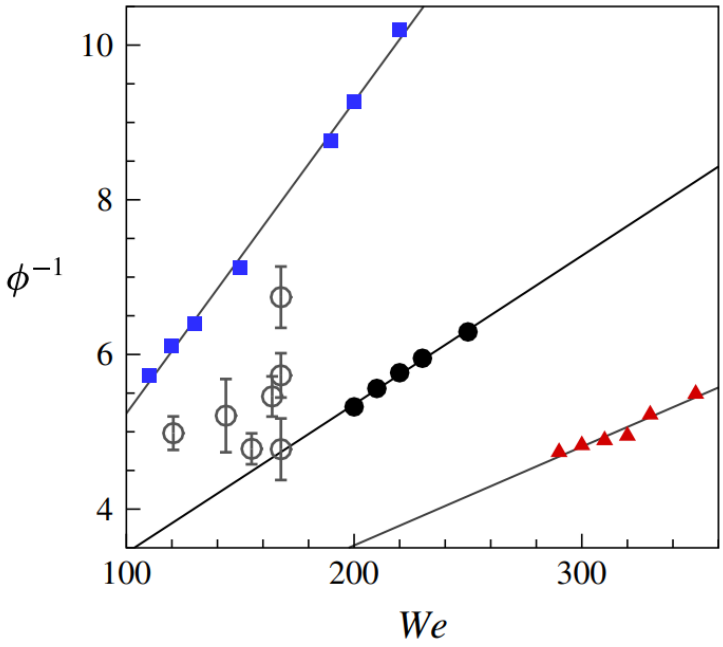

Fig. 2.26 Position of the pinned contact line as a function of Weber number and contact angle. The empty circles with error bars denote experimental results, where $\theta = 100 \pm 10°$. The filled symbols denote numerical results: triangles correspond to contact angle of 90°, circles correspond to 110°, and squares correspond to 130° [94].

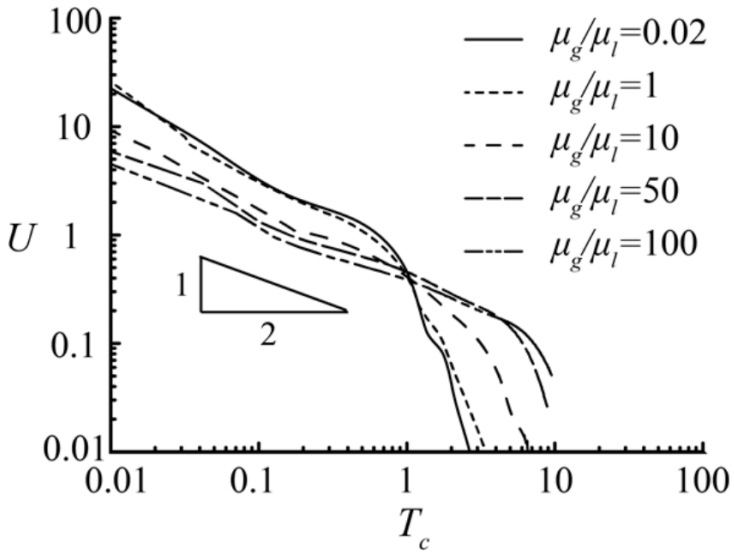

Fig. 2.27 Speed of the moving contact line U as a function of the dimensionless time T_c, where T_C is measured after the rupture of the gas film. Five different viscosity ratios μ_g/μ_l are used in a range from 0.02 to 100. In all cases, a slope of $-1/2$ is observed in the early stage of the film retraction. After this, the speed decreases steeply, corresponding to the fact that the moving contact line has pinned at the equator [95].

thin sheet of air is produced which contracts to a bubble at the south pole of the sphere. Moore [97] has incorporated the presence of the air film between the sphere and the liquid surface into the classical Wagner model of impact theory, showing that prior to impact viscous forces in the air deform the free surface and cushion the impacting body, reducing the forces which it experiences.

2.5 Contact Line Instabilities

In the previous section, we have discussed the dynamics and eventual pinning of the contact line in the case of a sphere impacting on a liquid surface. One might ask if this contact line can develop instabilities. It is known that interfacial instabilities may form by entrainment of air at the wetting front of impacting droplets on smooth liquid films [98]. Contact line instabilities under perturbation also occur for the classic case of a thin liquid film flowing down an inclined plane [99, 100]. Experiments of Quéré [101] and Sedev and Petrov [102] tested the stability of forced advancing contact angles under conditions of partial wetting. It was found that if a solid plate is plunged into a liquid to be coated via an advancing contact line, the contact line may remain stationary at speeds of the order of several metres per second. Nieh et al. [103] considered the case of a liquid droplet which spreads on a solid substrate. For liquids of low viscosity, the droplet spreads very quickly and the contact line acquires a scalloped shape, similar to that observed in [3]. It was found that polymer solutions containing below 5% polymer (ie. low viscosities) that droplets exhibited very rapid spreading and contact line instabilities. López et al. [104] performed a linear stability analysis showing that at large velocities, inertial forces exert a destabilising influence on the contact line.

Eggers [105] studied a solid plate plunging into or being withdrawn from a liquid bath in order to demonstrate the difference between the local behaviour of advancing and receding contact lines. A schematic of the experiment in the case of the advancing contact line is shown in Figure 2.28. A hydrodynamic model was used which neglects the presence of the ambient gas. In this model, an advancing dynamic contact line is always stable and persists to arbitrarily high speeds. Neogi [106] considered unstable contact lines for spontaneous spreading of a droplet on a solid substrate. It was observed that the spreading droplet has a large amount of curvature localized to the vicinity of the contact line, where linear stability analysis showed that this curvature may destabilise the contact line region. In Figure 2.29, a sketch of the droplet is shown along with an enlarged view of the region of interest.

If the droplet is perturbed from a local thickness $\overline{h}$ to $\overline{h}+h'$, the perturbation adds a Laplace pressure ΔP which is proportional to a sum of two terms

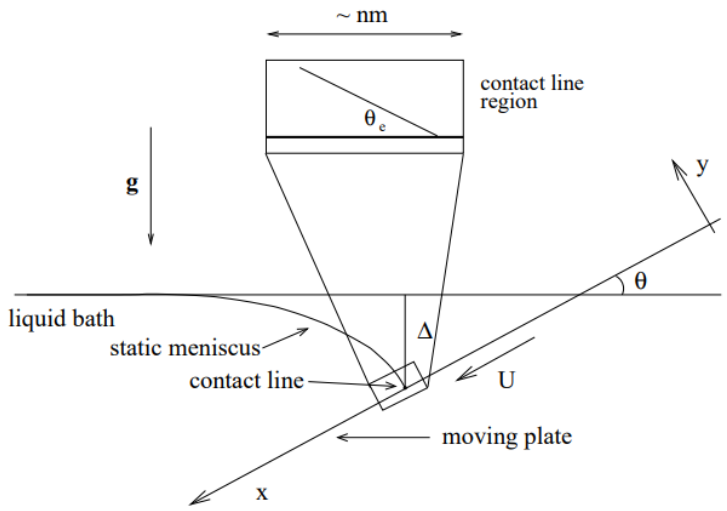

Fig. 2.28 A schematic of the setup: a plate is pushed with speed U into the fluid at an angle θ. The depression of the advancing contact line relative to the level of the liquid bath is Δ. The advancing contact line is stable at any speed [105].

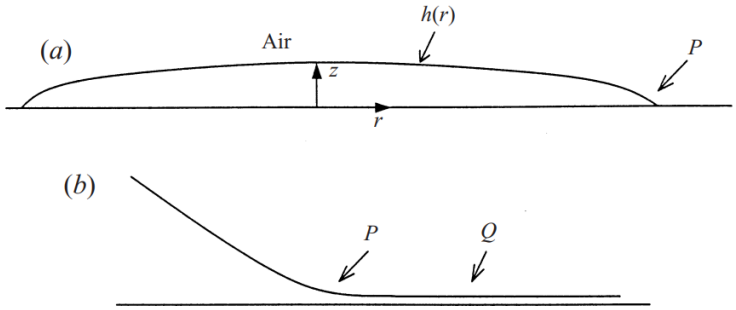

Fig. 2.29 Shape of droplet and enlarged view of the region of interest [106].

$$\Delta P \propto \nabla^2 h' + (4\overline{H}^2 - 2\overline{K})h', \tag{2.26}$$

where ∇^2 is the Laplace-Beltrami operator and $\overline{H}$ and $\overline{K}$ are the mean and Gaussian cuvatures of the base droplet profile. The first term is commonly accounted for in linear stability analyses [107]. Since the mean and Gaussian curvatures vanish when the base droplet profile is a flat film, the second term will only appear in the case of a wetting liquid, where the droplet will have a large curvature close to the apparent dynamic contact line. It follows that this instability is not observed for spreading of droplets of non-wetting liquids. As larger curvatures are expected for forced spreading at high impact speeds, these cases should frequently be accompanied by unstable contact lines as the speed increases.

We have so far not said much about the effects of surface roughness on solid-liquid impacts. The main reason that almost all experimental work on sphere-liquid impacts

focuses on smooth spheres is that surface roughness is assumed to influence water entry behaviour in a way which is similar to that of contact angle, hence introducing roughness would complicate the analysis even further [72]. This was confirmed by Zhao et al. [108], who who showed that dynamic wetting on hydrophilic rough surfaces can be similar to wetting of hydrophobic surfaces and surface roughness may promote destabilization of a moving contact line on a hydrophilic surface and hence cavity formation during impact. Beyond the balance of forces where a stable wetting interface, wetting failure occurs, where the promoting effect occur whens the wetting speed is high to create a gas-liquid-solid interface close to the moving contact line. The effect is shown in Figure 2.30, where it can be seen that there is a contact line instability at the roughened patch compared to the smooth part of the sphere, which has a stable moving contact line.

In Figure 2.31, the threshold speed for cavity formation is plotted against both static contact angle and surface roughness R_z. A theoretical explanation is that surface roughness changes the capillary driving force in the inner region (shown schematically in Figure 2.32). A rough surface is approximated as a smooth surface patterned with capillaries, where the characteristic depth h and diameter L of capillaries are determined experimentally and statistically. Close to the moving contact line, an inner and an outer region are defined depending on the transition length h_c. In the outer region, the profile of the film is dominated by external forces and capillarity, and the dynamic contact angle θ_d is observed. In the inner region (also shown in Figure 2.32), the interface is mostly dominated by capillarity and viscous friction frictions, meeting the solid at a truncated length scale h_m with a microscopic contact angle θ_m.

When the liquid film moves on the surface, the wetting front advances parallel to the surface of the sphere with velocity V_f and also fills the capillaries in the vertical direction with a speed V_c. Figure 2.32 implies that the moving contact line travels along a gas-liquid-solid composite surface, decreasing the capillary driving force from $\gamma(\cos\theta_e - \cos\theta_d)$ to $\gamma(\cos\theta_{CB} - \cos\theta_d)$, where θ_e is the static contact angle, θ_d is the dynamic contact angle, and θ_{CB} is calculated by the Cassie-Baxter equation [101]. Since the viscous friction force is only altered slightly due to the fact that the slip length induced by surface roughness is not more than 5 μm, the imbalance of the driving and friction forces induces a contact line instability and the threshold speed for cavity formation is lowered accordingly.

Huang and Gates [109] considered the effect of roughening hydrophobic, rather than hydrophilic, surfaces on the apparent contact angle around a liquid drop. The analysis is complicated by the fact that the three-phase contact is a complex, three-dimensional line which varies depending on the dimensions of the roughness and its spatial heterogeneity, which can cause the contact line to have a varying height above the horizontal substrate. The results showed that the apparent contact angle varies around the outside of the droplet due to the roughness of the surface which makes first contact with the droplet and that both

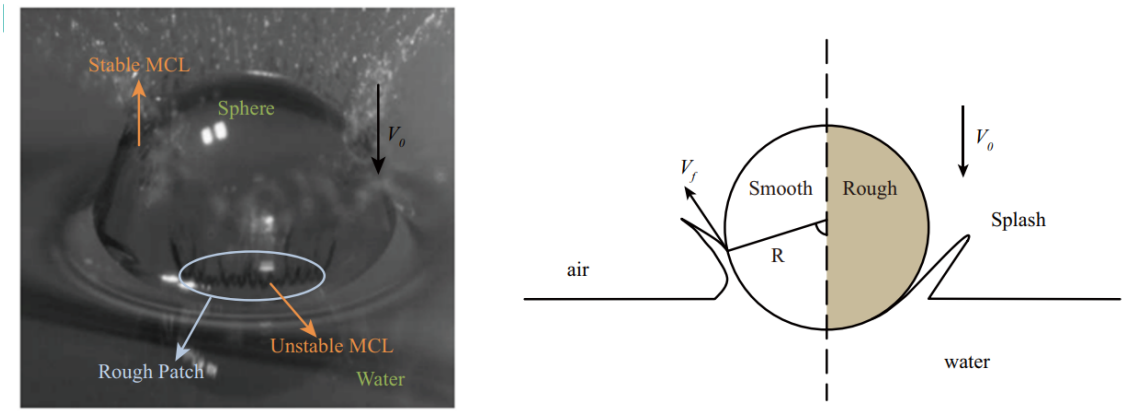

Fig. 2.30 Splash generated by a partly roughened glass sphere impacting a body of water with speed 3.6 ms^{-1}. Left: photo showing stable and unstable moving contact lines. Right: schematic showing that on a half-roughened sphere, the film detaches from the rough patch and a cavity is induced. V_0 and V_f are the impact velocity of the sphere and velocity of the wetting front, where $V_f \approx \zeta V_0$ [108].

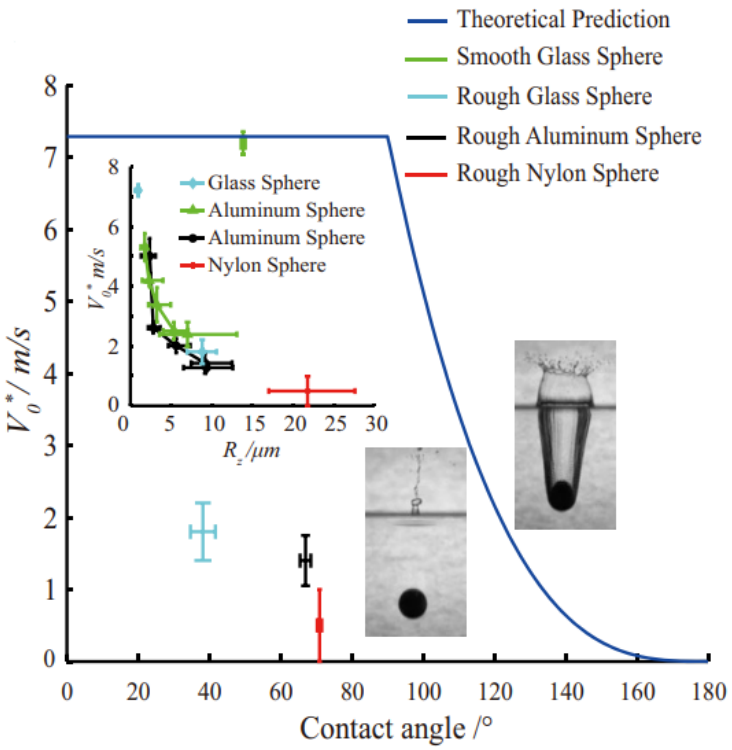

Fig. 2.31 Threshold speed for cavity formation versus static contact angle and surface roughness R_z [108].

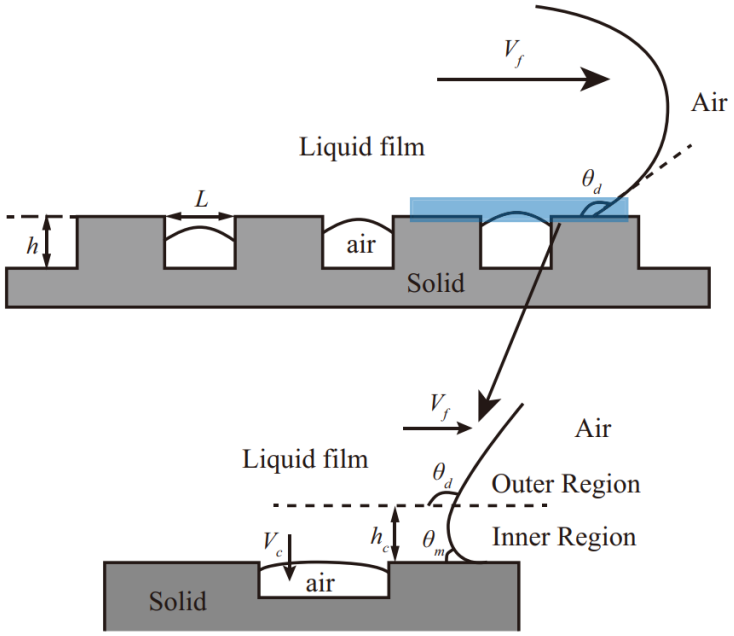

Fig. 2.32 Top: a rough surface is approximated as a smooth surface patterned with capillaries, where the characteristic depth h and diameter L of capillaries are determined experimentally and statistically. Bottom: close to the moving contact line, an inner and an outer region are defined depending on the transition length h_c [108].

the wetting models of Wenzel and Cassie and Baxter tend to overestimate the apparent contact angle of droplets on roughened surfaces.

2.6 Wetting Theory

We will finish with a brief description of wetting theory. Although this theory is mentioned several times in the previous sections, we have postponed this discussion until the final section in order to focus on applications. The subject of wetting and spreading of liquids has been described many times in the literature [110, 111]. A droplet spreads out to form a film when placed on a solid substrate, whereas a substrate covered with a film may dewet given some change in the parameters of the system. In the classic problem of a solid plate plunging into or being withdrawn from a liquid body, the dewetting case corresponds to the withdrawal of the plate. In this case, a threshold speed exists above which the triple-phase contact line cannot remain stationary and the solid cannot remain dry [112].

Wetting refers to the ability of a liquid to stay in contact with a solid surface. The wettability in a certain physical problem depends on the liquid and the solid and is generally quantified by the static contact angle θ_0 (the angle with which the liquid-gas interface meets the liquid-solid interface).

Wetting refers to the ability of a liquid to stay in contact with a solid surface. The wettability in a certain physical problem depends on the liquid and the solid and is generally quantified by the static contact angle θ_0 (the angle with which the liquid-gas interface meets the liquid-solid interface). A macroscopic explanation of wetting is as follows: if a droplet of liquid spreads easily over a flat solid surface, then the adhesive forces involved in the intermolecular interactions are stronger than the cohesive forces (it is chemically favourable for surfaces composed of different particles to stick together). If a droplet has difficulty spreading, then the cohesive forces are stronger (it is chemically favourable for molecules of the same type to stay together). In both cases, the favourability for wetting is characterised by the static contact angle via the Young equation (or some modification thereof). After rearranging for $\cos\theta$, the most basic possible version of the Young equation is as follows:

$$\gamma_{SG} - \gamma_{SL} - \gamma_{LG}\cos\theta_C = 0, \tag{2.27}$$

where θ_C is the contact angle in equilibrium, γ_{LG} is the liquid-gas surface tension, γ_{SG} is the solid-gas surface tension and γ_{SL} is the solid-liquid surface tension. A low contact angle below 90° generally indicates favourable wetting, a contact angle roughly between 90° and 150° indicates a hydrophobic surface which repels water, and a contact angle above 150° indicates that the surface is superhydrophobic and that wetting is impossible. In reality, the angle which we describe is only the static contact angle and in applications one usually considers a larger dynamic contact angle which we have mentioned in previous sections [113].

It should be clear that this fits into the work of Duez et al. [89], where wettability (or susceptibility to becoming wetter) of the sphere corresponds to contact angle. As discussed previous, sphere with different wettabilities exhibit completely different impact behaviours, with an air cavity forming for a hydrophobic sphere at a certain threshold speed and no cavity at the same speed when a hydrophilic sphere was used. An interpretation was this fact was proposed in terms of the stability of the contact line. In the case of a hydrophobic sphere, the gas can be viewed as the wetting phase and the solid sphere moves toward the liquid viewed as the non-wetting phase. A critical speed exists above which the line where all three phases meet becomes unstable, which is reached as the dynamic contact angle θ_d goes to 180° [61, 112]. Note that the dynamic contact angle θ_d for a moving triple line is always larger than the static contact angle θ_0, which only depends on the properties of the sphere.

In this work, we are interested in the possible influence of the ambient gas for wetting in the problem of a sphere impact. A related configuration where the gas does play a role in wetting is that of a dipping or coating flow, where a solid strip is dipped into a liquid

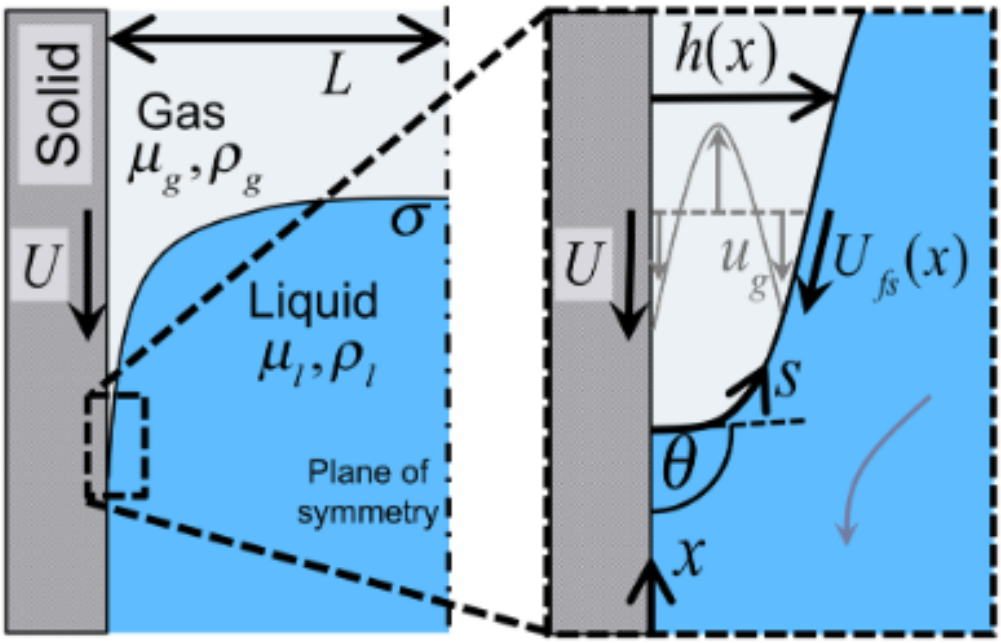

Fig. 2.33 Flow configuration (left) and close-up of the thin film region (right). It can be seen that the free surface bends to attain its contact angle θ [115].

at a steady rate. All coating flows have a dynamic wetting line which forms where the liquid makes a dynamic contact angle with the moving solid surface. Benkreira and Khan [114] performed experiments which demonstrate that air entrainment in a dip coating flow can be suppressed under reduced pressures and attributed this effect indirectly to the mean free path of the gas. Gas kinetic effects are significant in dynamic wetting problems at low speeds, because the maximum speed at which the liquid can wet the solid surface is controlled by the speed at which the wetting gas lubrication film in front of the moving contact line is displaced. The height of these films is typically extremely thin (of the same order as the mean free path of the gas) and as a consequence dip coating flows can be successfully described by models which incorporate kinetic effects. In Figure 2.33, we show the flow configuration for such a dip coating flow.

Sprittles [115, 116] developed such a model which uses kinetic theory in the gas film as described by the Boltzmann equation and combined this with regular hydrodynamics in the liquid phase as described by the Navier-Stokes equations . Simulations were performed in a finite-element framework which identified situations in which regular fluid dynamics cannot predict the maximum speed $U_{\max}$ at which a liquid-gas free surface can wet a solid substrate. The calculations showed that a conventional no-slip model with a fixed slip length completely misses the experimental results of Benkreira and Khan [114] for $U_{\max}$ as the pressure of the gas is reduced. On the other hand, a model which uses kinetic theory for the gas phase diverges from slip models where the slip at the gas-solid and

gas-liquid interfaces is proportional to the mean free path once the pressure is reduced by a factor of 10. The model which uses Boltzmann theory to describe the gas film has better agreement with experimental data on dip coating flows. This confirms once again that in dynamic wetting problems one cannot neglect kinetic effects in the gas. In the coating problem, incorporating effects of the gas allows one to predict experimentally observed dependencies of $U_{\max}$ on the viscosity of the liquid and the pressure of the gas.

More recently, Keeler et al. [117] studied a computational model of dynamic wetting with molecular dynamics and applied it to the displacement of an externally driven liquid plug between two partially wetted parallel plates. It was found that in forced dewetting the contact angle is a function of the speed of the contact line, with the true contact angle θ_{cl} emerging as part of the solution. The maximum dewetting speed U^* was interpreted as a fold bifurcation in the steady phase diagram and it was observed that the apparent contact angle (the experimentally visible contact angle at the bifurcation) is non-zero, in contradiction with predictions from studies based on the lubrication model of the flow close to the contact line.

Chapter 3

Role of Ambient Gas in Cavity Formation

In this section, we present our novel experimental results. To summarise briefly, we use high-speed photography to investigate the influence of the surrounding gas on cavity formation following the impact of a smooth dry wettable sphere on the free surface of a liquid body. We begin by varying properties of both the solid and the liquid, finding agreement with existing experimental data on threshold speeds for cavity formation. We then investigate the influence of the surrounding gas on cavity formation by varying the pressure of the gas and also using three different gases (air, helium, and argon). The use of different gases allows us to isolate the effect of the mean free path. In particular, we observe that cavity formation following a sphere impact on a liquid surface can be completely suppressed by reducing the pressure of the gas. This is the first time that the transition from a cavity to a no cavity event has been effected only by changing the properties of the ambient gas. We find that the most important parameter for influencing cavity formation is the density of the ambient gas and that the mean free path of the gas has negligible influence.

3.1 Experimental Set-up

The experimental set-up is shown schematically in Figure 3.1. The target liquid container was placed on a stand of adjustable height and the sphere was held above the container by an electromagnet connected to a power supply. The electromagnet was fixed into a Perspex block which sits on top of a cylindrical tube around the container, forming a vacuum chamber. Once the tube was sealed at top and bottom, a vacuum pump (Leybold) connected to the bottom of the chamber was switched on to reduce the ambient pressure inside the tube to a level which was read by a pressure gauge which was also connected

to the chamber. The tube had an inner diameter of 18.5 cm and thickness 0.6 cm and the liquid container had a length of 10.1 cm, width 8.4 cm and height 13.2 cm. To ensure negligible influence due to wall effects, before each drop the sphere was lined up with the middle of the liquid body to ensure that even the largest sphere with diameter 1.5 cm was always at a distance of around six sphere radii away from the closest wall. The ambient pressure was varied between 101 kPa (atmospheric pressure) and 0.14 kPa. In certain experiments, argon and helium gas were also pumped into the vacuum chamber. In the case of air, the pressure is measured using an in-built pressure sensor. This sensor was inaccurate for other gases apart from air so when using other gases a manual manometer was used which was calibrated to give accurate readings. To ensure that there was no mixing of gases, we made sure to evacuate the chamber of all atmospheric air before starting to introduce argon or helium gas until the required pressure was reached.

Only smooth spheres were used in the experiments and we did not investigate the influence of surface roughness. It has recently been shown, however, that surface roughness can promote destabilisation of the moving contact line on a hydrophilic surface and hence wetting failure and cavity formation [108]. The link between wetting failure and surface roughness is quite complicated and the analysis can depend on the limit which is taken (for example, the superhydrophobic limit) [118]. The overall effect of wetting failure promoted by surface roughness depends on the impact velocity being high enough to create a composite gas-solid-liquid interface close to the moving contact line (typically beyond 2.9 ms^{-1}, a speed which we do not exceed in our experiments).

We tested that the effect of ambient gas pressure on the threshold speed was not affected by roughness by using identical chrome steel spheres with the same diameter, but altered surface roughness. The surface roughness was achieved by rubbing with abrasive sandpaper and then measured using white light interferometry, which can be used to image rough surfaces as long as the roughness is kept within certain limits [119, 120]. It was found that the spheres had a mean square roughness below 1 μm [121]. This failure to influence wetting was attributed to the fact that the mean square roughness even for the roughened sphere was well below the thickness of the viscous boundary layer, which is estimated to reach $\mathcal{O}(100\,\mu\mathrm{m})$ at the equator. However, the theory of Zhao et al. [108] suggests that the roughness can begin to cause a drop in the threshold for cavity formation of a hydrophilic sphere at around 5 μm. A study of the combined influence of surface roughness of oleophilic spheres and the properties of the ambient gas on cavity formation would be a natural next step on the experimental side, although in this case the mechanisms involved would likely be much more complicated.

The sphere was then released by switching off the electromagnet at the power supply and allowed to fall freely under the influence of gravity towards the liquid. The impact of the sphere on the liquid was captured with a Photron FASTCAM SA-X2 high-speed

video camera at a frame rate of 12 500 fps. Backlighting was provided by a single light source (Phlox) of luminance 178 256 cd/m^2 and uniformity 99.44%. The recordings were triggered manually and saved to a PC for analysis. A cavity is judged to have formed when there is a dark 'tail' or 'blob' attached to the sphere which contrasts with the background, even if the blob is small. A no-cavity case is judged to have occurred when no blob can be distinguished on the top of the sphere. The ability to distinguish whether there is a blob is limited by the spatial resolution of the camera, which is 0.02 mm/pixel. The measurements were performed two or more times for each physical parameter, and their average value was used as the representative value. The visual limit on distinguishing the appearance of a cavity plus uncertainties in the experimental conditions leads to an uncertainty of 0.4 ms^{-1} in the difference between impact speed required for a cavity to form as opposed to no cavity, which in turn causes some overlap at the line which we will show in Figure 3.4 which splits the data set into a cavity and no-cavity regimes. However, the lines dividing regimes for impact problems are never taken to be exact due to experimental uncertainties and this overlap is standard practice in the experimental literature on droplet and sphere impacts (see, for example, Figure 2.4 and Figures 2(a)-(d) in [72]).

The spheres were made of untreated chrome steel with density of 7.8 g/cm^3 and static contact angle $\theta \approx 20-25^\circ$ such that they can be considered to be oleophilic. The mean square roughness of the spheres was measured using a Bruker Contour profilometer at 0.3 μm, well below the thickness of the viscous boundary layer, which reaches $\mathscr{O}(100\,\mu\text{m})$ at the sphere equator (more information on these measurements can be found at [121]). Typical image sequences acquired when a sphere of diameter 15 mm plunges into the oil at atmospheric pressure, at 0.53 bar, and at 0.5 bar are shown in Fig. 3.5, demonstrating that reduced pressures can suppress cavity formation.

To avoid contamination, the sphere was washed after each experiment with dilute ethanol and then washed twice with deionised water and dried with Kimtech Science wipes. The liquids used were all low-viscosity silicone oils. It was determined that water was not suitable due to having a very low boiling point at the low pressures which would be needed for the experiment. We do not go to extremely low pressures in our experiments, as it is expected that a cavity would form which is due to cavitation bubbles and not due to the motion of the splash above the free surface. Onset of cavitation is typically predicted using the cavitation number Ca, which for sphere-liquid impacts is defined to be

$$\text{Ca} = \frac{P_{\text{amb}} - P_v}{\frac{1}{2}\rho v^2}, \tag{3.1}$$

where P_{amb} is the pressure of the ambient gas, P_v is the liquid vapour pressure, and $\frac{1}{2}\rho v^2$ is the dynamic pressure drop of due to high flow speed v of the liquid with density ρ [122]. The vapour pressure for the silicone oils which we use only depends on the temperature

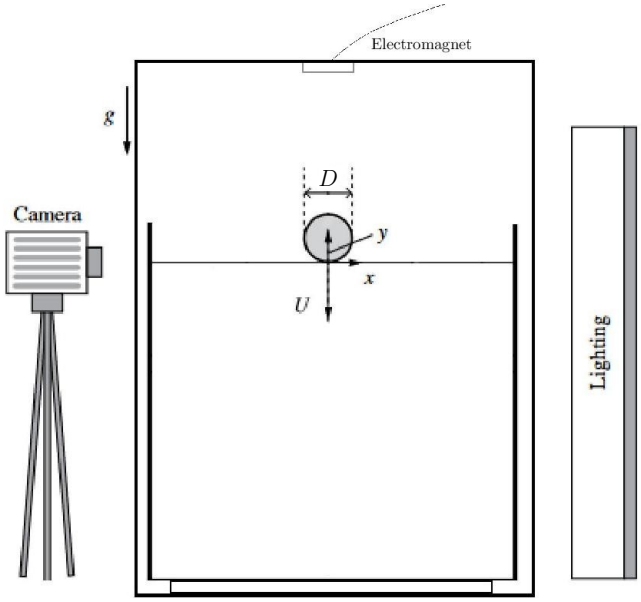

Fig. 3.1 Schematic of experiment (not to scale). The x and y coordinate axes are shown on the sphere and the wire at the top denotes that the electromagnet is attached to a power source which is switched off to release the sphere. Note also that the experiment is inside a closed chamber which can be evacuated with a vacuum pump.

and is extremely low at standard room temperature, so we will set it to zero for the purposes of estimates, which leaves us with [123, 124]

$$\mathrm{Ca} = \frac{P_{\mathrm{amb}}}{\frac{1}{2}\rho v^2}. \tag{3.2}$$

The value at which cavitation onset occurs is not always easy to calculate and can depend on the characteristic velocity which is used. Since it is believed that the characteristic speed in experiments which involve dynamic wetting should be the speed of the contact line or the wetting front of the liquid which rises around the sphere, we will assume that the characteristic velocity is the velocity of the contact line. In this case, experiments of Speirs et al. [122] suggest that when this velocity is used, cavitation onset should fall in the range where Ca is between $\mathscr{O}(10^{-4})$ and $\mathscr{O}(10^{-5})$. If we assume the impact speed of the sphere is 2 ms^{-1}, then the contact line speed (or speed of the wetting front) v is approximately 6 ms^{-1} by work of Duez et al. [89].

Using as input the above value for the density of the silicone oil, we find that for $P_{\mathrm{amb}} = 50$ Pa, the cavitation number is $\mathrm{Ca} \approx 3.2 \times 10^{-4}$. Values of $P_{\mathrm{amb}} = 25$ Pa, $P_{\mathrm{amb}} = 5$ Pa and $P_{\mathrm{amb}} = 1$ Pa imply cavitation numbers $\mathrm{Ca} \approx 1.6 \times 10^{-4}$, $\mathrm{Ca} \approx 3.2 \times 10^{-5}$ and $\mathrm{Ca} \approx 6.4 \times 10^{-6}$. This suggests that for 50 Pa, expanding bubbles will not form at the top of the sphere, whereas in a range between 25 and 1 Pa, expanding bubbles appear which lead to cavity formation. In Figure 3.2, we perform experiments confirming this

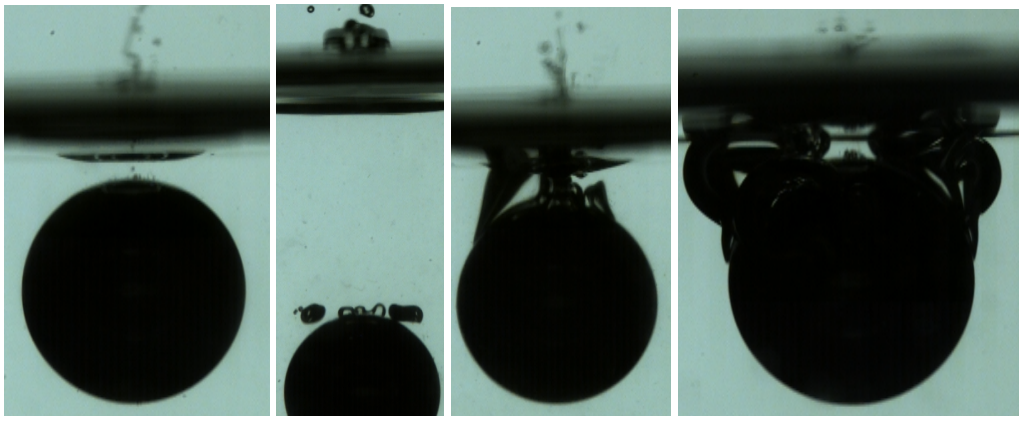

Fig. 3.2 Sphere impacts in air at speed 2 ms^{-1}, liquid viscosity $\mu_L = 1.74$ cP, and varying pressures: $p = 50$ Pa, $p = 25$ Pa, $p = 5$ Pa, and $p = 1$ Pa. The radius of the sphere is 7.5 mm.

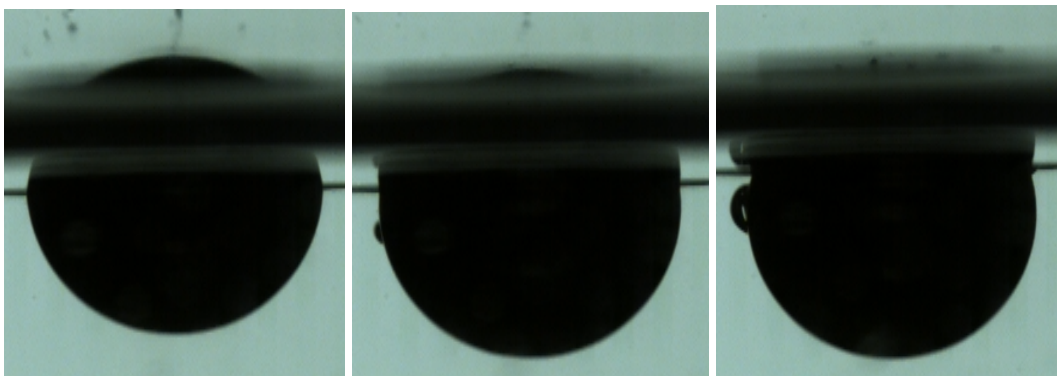

Fig. 3.3 Sequence of times prior to submergence of the sphere at $p = 1$ Pa. It can be seen that a cavitation bubble forms before the pole of the sphere has submerged and hence is not due to air entrainment. The liquid viscosity and sphere radius are as above.

prediction. Note that no cavity forms at 50 Pa, but that at $p = 25$ Pa , bubbles form which follow behind the sphere. This effect persists at $p = 5$ Pa and at $p = 1$ Pa. In order to make clear that the bubbles under discussion are entrained from the atmosphere and are formed in the liquid, we show in Figure 3.3 a sequence of events at $p = 5$ Pa. It can be seen that the cavitation bubble first forms on the side of the sphere before the sphere has even submerged and so is not due to air entrainment.

Silicone oil with viscosity $\mu_L = 4.35$ cP was so viscous that a cavity was always observed with no transition between cavity and no-cavity regimes. For this reason, we used silicone oils with viscosities $\mu_L = 0.87$, 1.74, and 2.61 cP. The oil density varies little with viscosity, being $\rho_l = 0.9$, 0.87, 0.9 g cm^{-3}, respectively, with surface tensions σ in a range between 15 and 20 mN m^{-1}. The sphere diameter was ranged between 2, 8, and 15 mm and entry speeds V were between 1 and 3.5 m s^{-1}. Three different gases were used for the ambient gas (helium, air, and argon) with molecular masses $M = 4$, 29, and 39

Daltons, respectively). Since the mean free path of the gas λ_g depends on the molecular mass, this allows us to separately isolate the effect of changing the density and the mean free path of the gas.

3.2 Results

We will present our quantitative results shortly but qualitatively we find that decreasing the pressure of the atmospheric gas can suppress the formation of a splash crown and a cavity. We will first show this in Figure 3.4, where one sees a difference between splashing at atmospheric pressure and splashing at a fraction of the usual atmospheric pressure. However, although Figure 3.4 shows a clear difference at different pressures, it could be the case that the transition from cavity to no-cavity is somewhat sudden, and that one reaches a turning point as the pressure is lowered where some balance of forces is modified so that a cavity does not form. This is in contradiction with the droplet splashing case studied in [17], where lowering the pressure gradually decreases the amount of splashing until there is none at all. To demonstrate that there is also a gradual change in the sphere impact case, we show a typical image sequence acquired when a sphere of diameter 15 mm plunges into the oil at atmospheric pressure and at 0.53 and 0.5 bar is in Fig. 3.5 (the impact speed is the same as that used for Figure 3.3). In Figure 3.4, we also include the times for each image, where impact is taken to begin at $t = 0$ s.

The experimental results are shown as points in Fig. 3.6 in the parameter space of the capillary number $\mathrm{Ca} = \mu_L V/\sigma$ and the gas density $\rho_g/\rho_{\mathrm{atm}}$, where σ is the liquid-gas surface tension. No-cavity events are plotted with blue markers and the impacts where a cavity was formed are shown in red. Note that in the parameter range tested, the threshold speed for cavity formation does not significantly depend on the sphere size.

Our main qualitative result is that the density of the gas is the most important parameter in influencing whether or not a sphere forms a cavity during an impact on the free surface of a liquid, with negligible influence from the molecular mass. The molecular mass of the gas and the pressure seem to have no effect provided that the density is kept constant, as confirmed by Fig. 3.7 where the mean free path is plotted at the horizontal axis, which is in stark contrast to experiments on droplet splashing [17]. It can be seen that the threshold speed plateaus when the gas density exceeds 0.6 atmospheric density and that it plateaus again when the gas density is lower than 0.2 atmospheric density.

In all cases, the transition between cavity and no-cavity regimes occurs in a threshold manner and is prone to instabilities. This is confirmed by occasional observations of no cavity cases at unusually high entry speeds beyond 2.5 ms^{-1} in Fig. 3.6. To demonstrate what we mean when we refer to the flow instability at high impact speeds and low gas

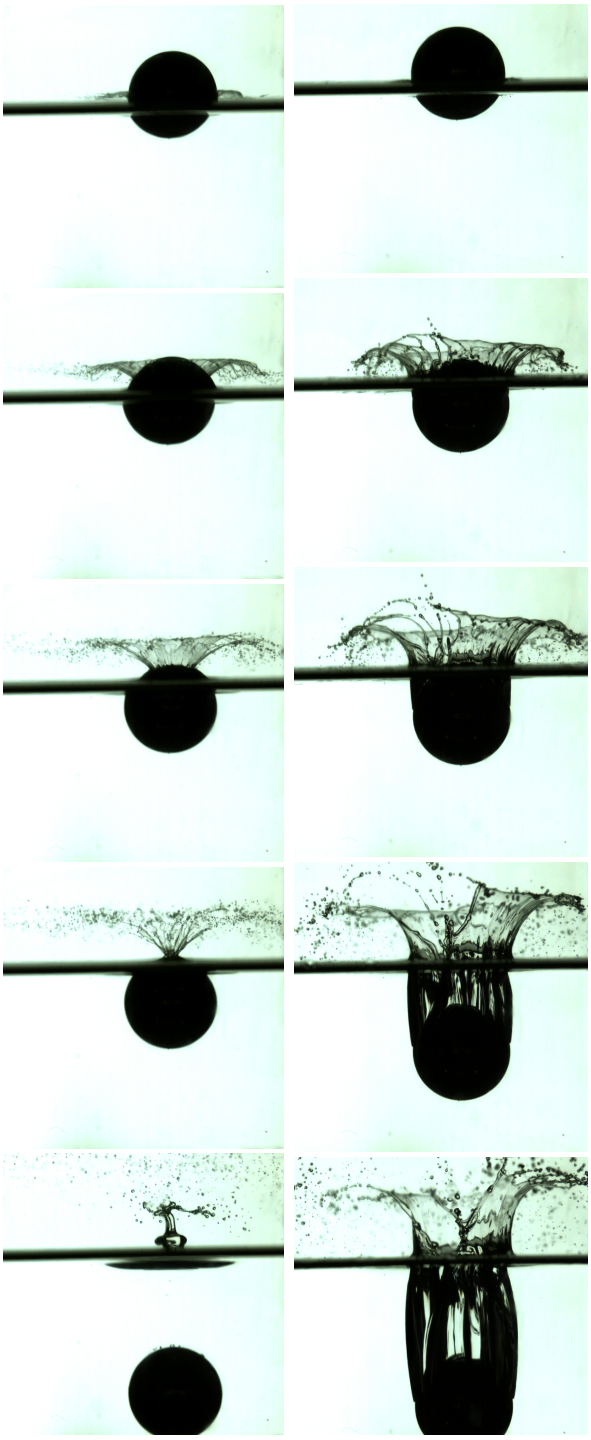

Fig. 3.4 Suppression of cavity formation at reduced atmospheric pressure. The left-hand images show a fraction of atmospheric pressure and the right-hand images show splashing at usual atmospheric pressure. The impact speed in both cases is $V = 2$ ms^{-1}, the liquid viscosity is 1.74 cP and the sphere radius is $R = 7.5$ mm.

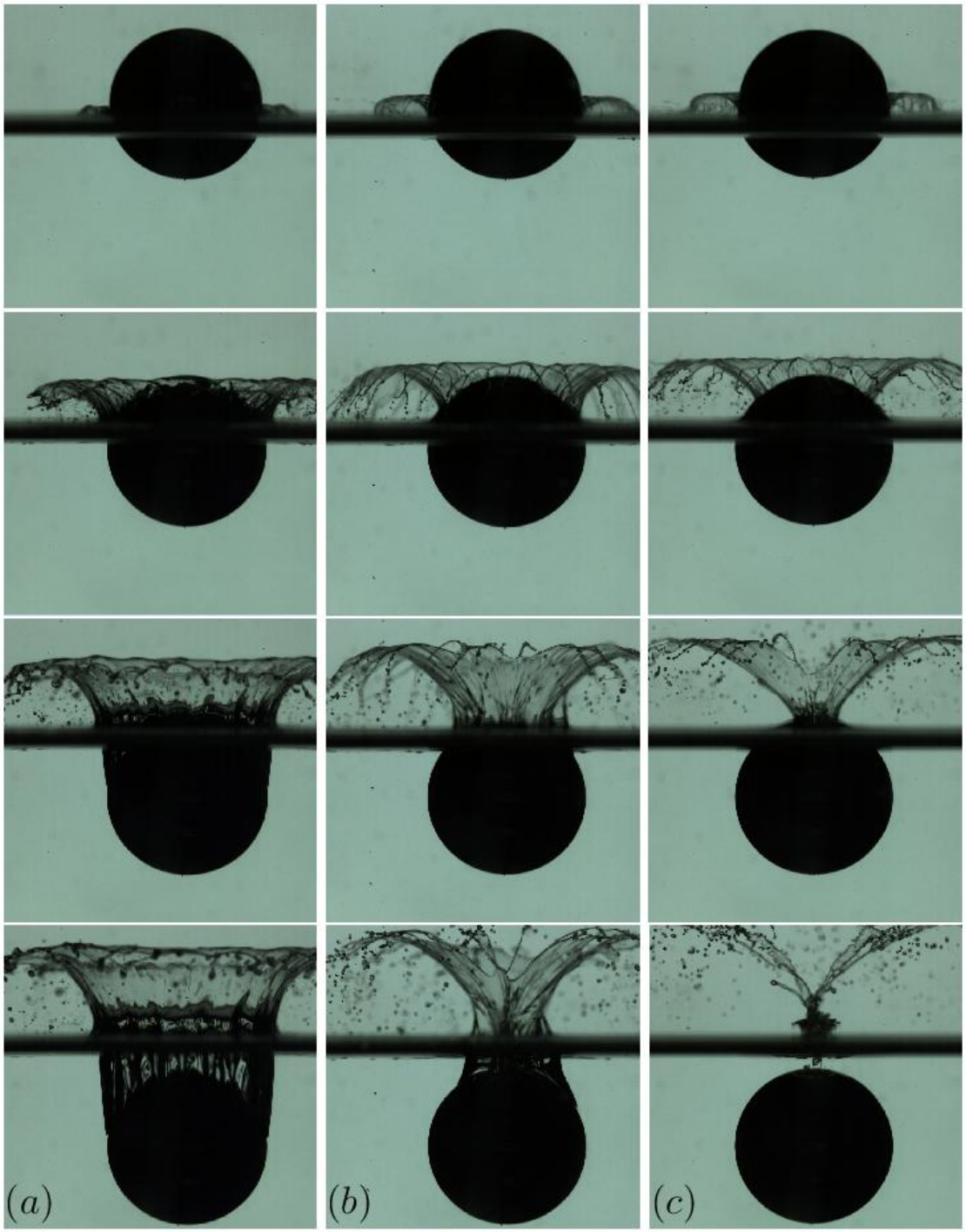

Fig. 3.5 Chronophotography of a sphere with radius 7.5 mm plunging into 1.74 cP silicone oil at $V = 2$ ms^{-1} at times 1.6, 3.2, 4.8, and 6.4 ms after touchdown. The pressures are (a) 1 bar, (b) 0.53 bar, and (c) 0.5 bar, respectively. Videos #1, #2, and #3 in the supplementary material.

densities, in Fig 3.8 we film from above with a sphere dropping at Ca above 0.3 and gas density below 0.2 and show that there is a flow instability leading to a splash formation even though the flow on the right-hand side of the sphere seems to be rising up towards the pole. It seems likely that it is this effect which is responsible for the plateau in the threshold speed curve once one reaches $\rho_g = 0.2$. In both the cavity and no-cavity case, it can be seen that a curtain of liquid (which we will refer to as the splash curtain) forms after impact and rises up around the sphere (a top-down view of the splash curtain is shown in Figure 3.9).

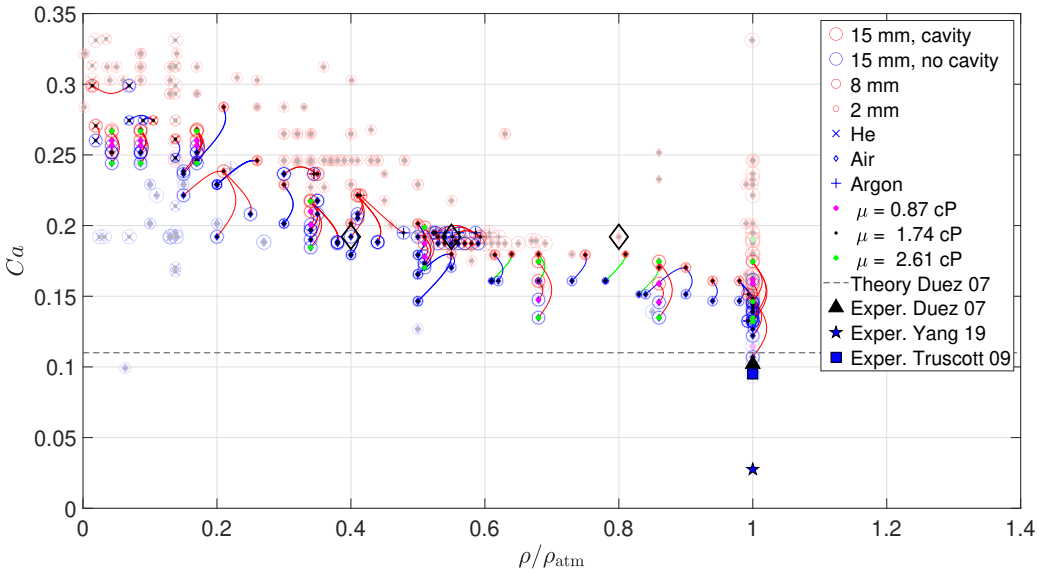

Fig. 3.6 Diagram of cavity/no cavity regimes at varying gas density ρ_g and capillary number Ca for spheres of diameters of 2, 8, and 15 mm, gases with molecular masses of $M_{\mathrm{He}} = 4$, $M_{\mathrm{Air}} = 29$, and $M_{\mathrm{Ar}} = 40$, and three silicone oils of viscosities $\mu_L = 0.87$, 1.74, and 2.61 cP. Cavity/no cavity pairs with similar sphere size, oil viscosity, and gas are connected by a line to indicate uncertainty of the cavity/no cavity threshold (red, blue, and green lines are used for the 15, 8, and 2 mm spheres, respectively. Black diamonds indicate regimes used to plot Fig. 3.5. The black triangle and the black dashed line correspond to the experimentally observed transition point and the theoretical prediction from [89]. The blue pentagram and blue square indicate no-cavity cases found in experimental data of Yang et al. [125] and Truscott and Trechet [126].

3.3 Discussion

In this chapter, we conducted an experimental investigation of the role which the properties of the ambient gas play in cavity formation for sphere impacts on liquid bodies. This presents an interesting addition to the large existing literature on sphere-liquid impacts,

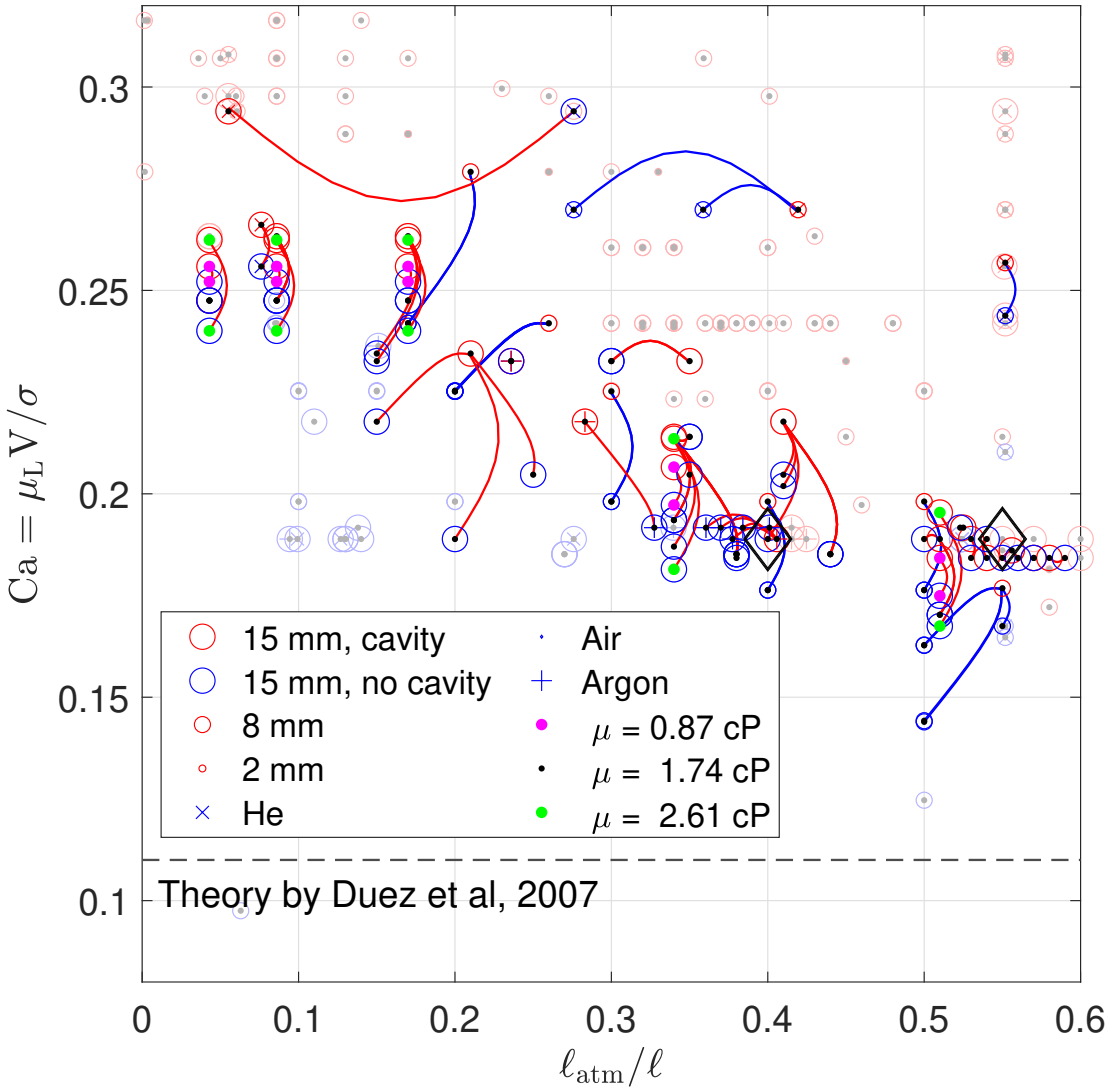

Fig. 3.7 Diagram of cavity/no cavity regimes similar to that in Fig. 3.6 with the inverse mean free path ℓ_atm/ℓ at the horizontal axis. Note that, although a trend related to the change in mean free path is present, a number of experiments with He prevents us from plotting an unequivocal divider between cavity and no cavity regimes.

where one typically considers only the properties of the solid or the liquid. The case where the ambient gas pressure is standard atmospheric pressure corresponds to experiments conducted in existing studies. Our finding that the threshold speed for cavity formation does not depend on the diameter of the sphere in a range of diameters between 2 and 15 mm is consistent with the experimental results of Speirs el al. [72] and Duez et al. [89], where independence of threshold speed on sphere diameter was reported for a similar range of diameters. Unlike the work of [89], we did not vary the contact angle of the sphere

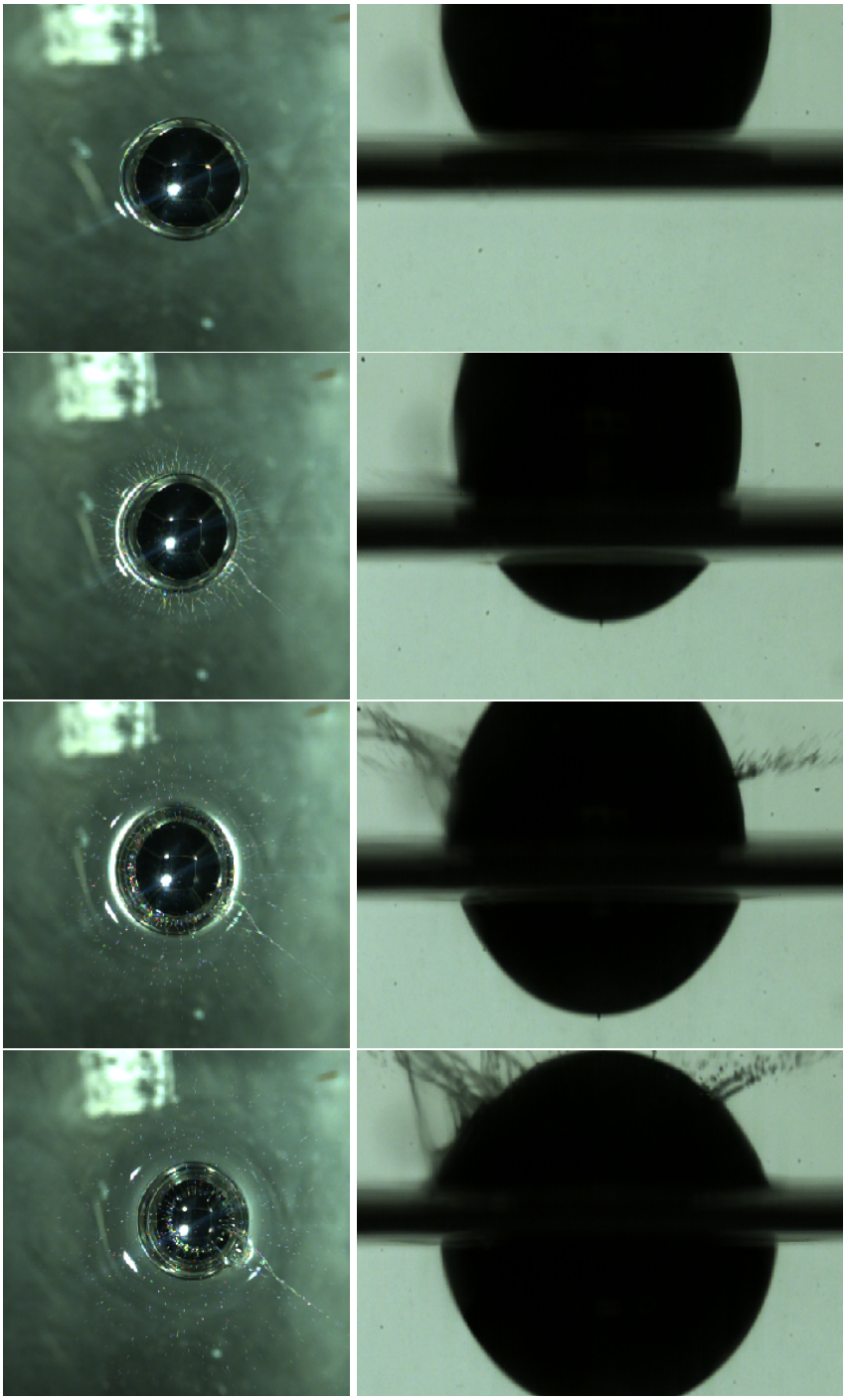

Fig. 3.8 Filming from above (left) and the side (right) to show cavity formation due to flow instability and perturbations at high capillary number and low gas density. The impact speed is $V = 2.9$ ms^{-1}, the ambient gas is helium, the sphere radius is $R = 7.5$ mm, the liquid viscosity is 1.74 cP and the pressure is 0.5 times atmospheric pressure. Note the asymmetry of the cavity: on the right-hand side, the liquid is travelling up around the sphere towards the pole, whereas on the left-hand side an instability causes liquid to depart away from the sphere so that a cavity eventually forms.

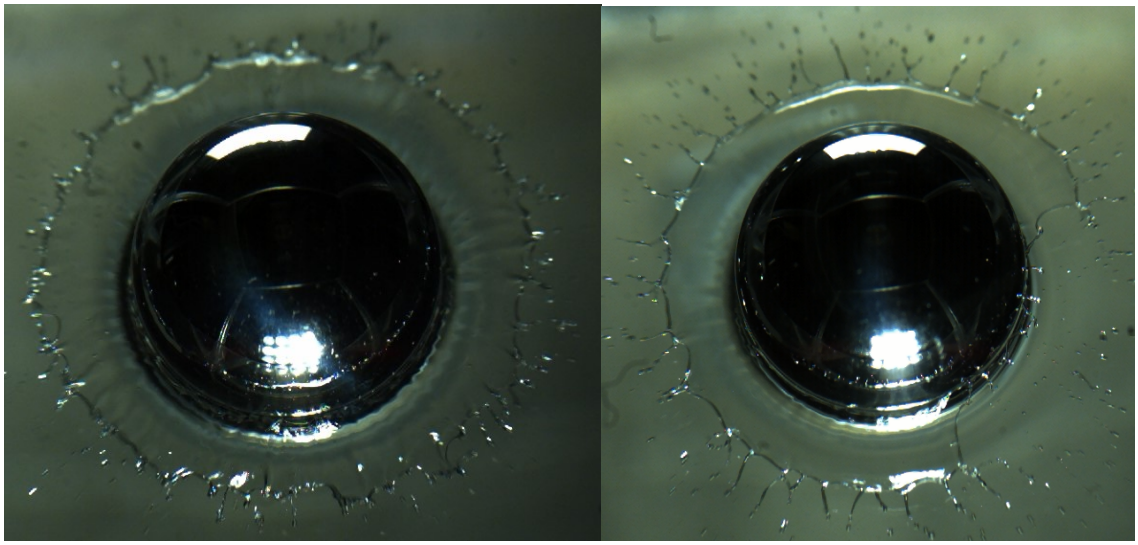

Fig. 3.9 Left: Impact of a sphere with radius 7.5 mm at speed 1.7 ms^{-1} in air at atmospheric pressure. Right: Impact of a sphere with radius 7.5 mm at speed 1.5 ms^{-1} in air at atmospheric pressure. The liquid viscosity in both cases is 1.74 cP.

and only considered spheres with low contact angles. For this reason, our comparison with experimental data on cavity formation at atmospheric pressure was restricted only to hydrophilic spheres. Such data can be found in experimental work of Yang et al. [125], Truscott and Trechet [126] and Duez et al. [89] and was found to be consistent with the results which we obtained at standard atmospheric gas density. Finally, the viscosity of the liquid was varied and it was found that the threshold speed had an inversely proportional dependence on viscosity at atmospheric pressure, in agreement with the model and experimental results of Duez et al. [89]. It was also confirmed that this scaling due to viscosity holds when the gas pressure is decreased.

Having obtained data at regular atmospheric conditions which were consistent with existing studies, the ambient gas density was varied. It was found that decreasing the ambient gas density increases the threshold speed for cavity formation, up until one-fifth atmospheric gas density, where the threshold plateaus. This is a surprising result, since previous studies have only considered properties of the liquid and the solid, neglecting the properties of the gas. In fact, the theoretical model developed by Duez et al. [89] states that cavity formation only depends on the contact angle and the ratio σ/μ_L and it was observed that lowering the ambient gas pressure had no effect on threshold speed.

Since changing the ambient gas density alters the mean free path of the gas, it was necessary to investigate whether this effect is due directly to the density of the gas or instead to kinetic effects related to the mean free path. This possibility was investigated by repeating the experiments using three different gases of varying molecular mass. It was found that changes to the molecular mass had a negligible effect on the threshold

speed, hence we concluded that changes to the density of the ambient gas have a direct influence on cavity formation. The influence of both the density and the mean free path of the gas is discussed in more detail in Chapter 4. We also describe further experimental measurements. These are intended to support a theoretical explanation which we propose in Chapter 5.

Chapter 4

Experimental Results and Optical Measurements

In this chapter we discuss the remainder of our experimental results. We discuss the influence of the mean free path before moving on to geometry of the splash crown for spheres of varying sizes, observations of contact line pinning and instabilities at low gas densities. We then discuss in detail the optical measurements which were performed to estimate the thickness of the splash crown. These results are intended to inform a theoretical model for the influence of the gas in cavity formation which will be described in Chapter 5 and in some cases are used to remove other possible models which differ from our explanation.

4.1 Role of Mean Free Path

To understand the effect of varying the ambient pressure, in Fig. 4.1 we compare images of a no-cavity event at the same gas density using two different gases (air and helium). It can be seen that the speed with which the liquid sheet rises up around the sphere is similar with no variation when the molecular mass of the gas is changed. We note that although the speed of the liquid sheet is not changed, the appearance of the crown and the ejection of secondary droplets varies. We next consider in Fig. 4.2 images of impact for varying gas density, one slightly below the cavity/no-cavity threshold and one slightly above. By comparing Fig. 4.2 (left) with Fig. 4.2 (right), it can be seen that the speed of crown propagation towards the pole is lower for increased gas density. When the gas density is sufficiently high (Fig. 4.2 (left)), polar propagation of the crown slows down far enough for the contact line to not meet at the pole of the sphere and it instead goes below the liquid surface so that a cavity forms.

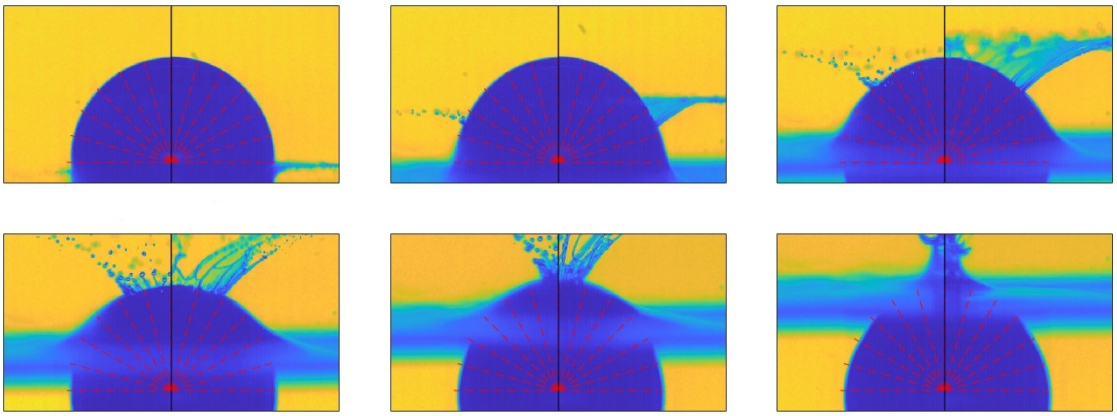

Fig. 4.1 Testing the influence of mean free path. Comparison of an impact in air at $p = 140$ mbar (left-hand side of each image) and in helium at $p = 950$ mbar (right-hand side). Both cases correspond to the same gas density of 0.14 atmospheric density. The sphere has radius 7.5 mm, the liquid viscosity is 1.74 cP and the impact speed is $V = 2.06$ ms^{-1}. Time separation between frames is 1 ms. Videos #4 and #5 in the supplementary material.

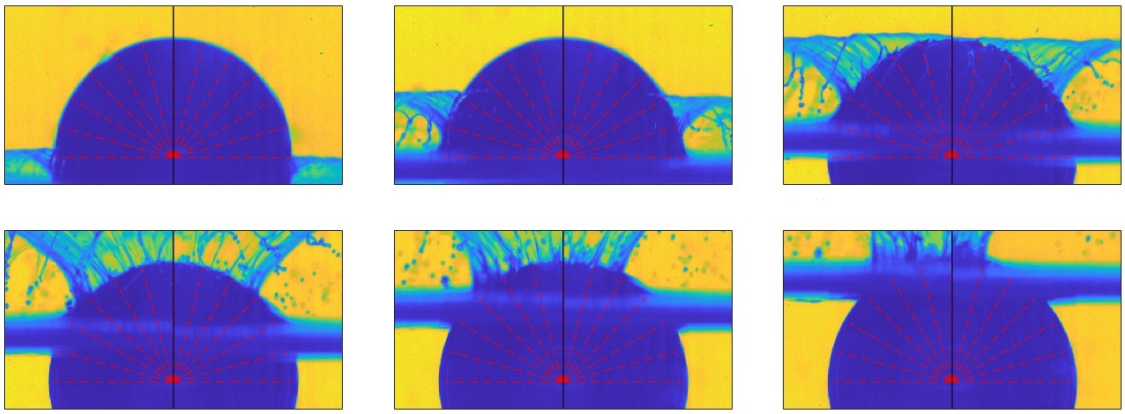

Fig. 4.2 Testing the influence of gas density. Comparison of an impact in air at density of 0.525 atmospheric density (left-hand side) and in air at density of 0.5 atmospheric density (right-hand side). The sphere has radius 7.5 mm, the liquid viscosity is 1.74 cP and the impact speed is $V = 2.06$ ms^{-1}. Time separation between frames is 1 ms. Parameters are chosen close to the threshold so that an increase in gas density of 5% leads to cavity formation. Videos #2 and #3 in the supplementary material.

.

Inspection of Fig. 3.4 suggests that whether a cavity occurs appears or not is determined by processes which occur above the free surface of the liquid body and above the equator of the sphere. This was confirmed by filming the experiment from beneath the free surface to measure the growth rate of the wetted circle below the equator, similar to experiments by [82]. In Figure 4.3, we show that in both cases evolution of the wetted region of the sphere is similar at the lower hemisphere. The black dashed line indicates the free-fall trajectory which would be expected for the displaced liquid from geometric considerations, indicating that within experimental uncertainties there is no influence on the motion of the contact line from trapped air in the pre-impact layer between the solid and the liquid and that cavity formation is not due to gas entrapment. We therefore eliminate the possibility that the observed shift of the threshold entry speed is related to gas trapped in the layer between the sphere and the liquid body and instead argue that the difference is due to the modification of the dynamics of the splash crown above the equator by the surrounding gas.

Another related possibility which one might consider is whether the gas flow around the sphere as it falls towards the liquid surface has an influence on the splash crown. To check this, in Fig. 4.4 we show a laser sheet visualisation with smoke as the seed material and air at atmospheric pressure. The resulting flow visualisation is as expected, with the presence of a wake behind the falling sphere which then flows out of the sealing crown and forms a pair of vortices either side, so we also rule this out as playing a role in cavity formation in our experiments.

The remaining explanation is that advance of the root of the crown (and hence the contact line) is where the gas plays its role, separating the experimental data into cavity and no-cavity regimes based on variation of gas density. By comparison of Fig. 4.1 and Fig. 4.2, we observe that the liquid-solid angle at the root of the crown is close to 90° at low gas density and decreases at higher gas densities. One should distinguish here between the advancing (apparent) contact angle at the liquid-solid boundary and the angle which the crown sheet makes with the surface of the sphere, which is defined by the ratio between the speed of the crown root and the polar velocity of liquid feeding into the crown. It follows from the equality of arc length and tangent length for sufficiently small arc angles that when the speed of the crown root and the polar velocity are the same, this angle is 90°. If this angle falls below 90°, the speed of the advancing contact line decreases. Close to the threshold speed, the ambient gas slows the speed of the contact line by up to 50%, resulting in a 50% decrease in the threshold speed as seen in Fig. 3.6.

The process by which the crown speed is slowed down by the presence of ambient gas is shown in more detail in Fig. 4.5, where we plot a spatiotemporal image illustrating propagation of the crown towards the pole. The image was created by stacking the semi-circular strips adjacent to the sphere at sequential instants of time. The dashed sinusoidal

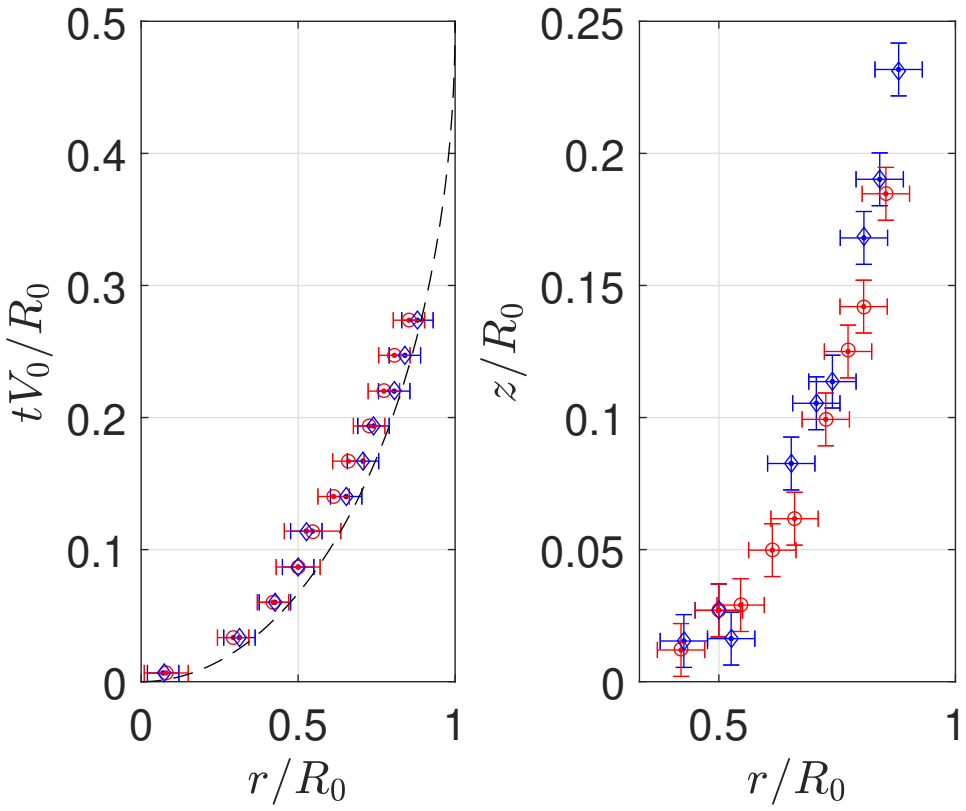

Fig. 4.3 Growth rate for wetted part of sphere against time. The dashed black line shows the radius of the cross-section of the sphere at the level of the liquid. Red markers correspond to the experiment where cavity was formed (air at 1000 mbar), blue markers to the experiment with no cavity (air at 150 mbar). The impact speed is $V \approx 2.3$ ms^{-1} and the liquid viscosity is $\mu_L = 1.74$ cP in both cases.

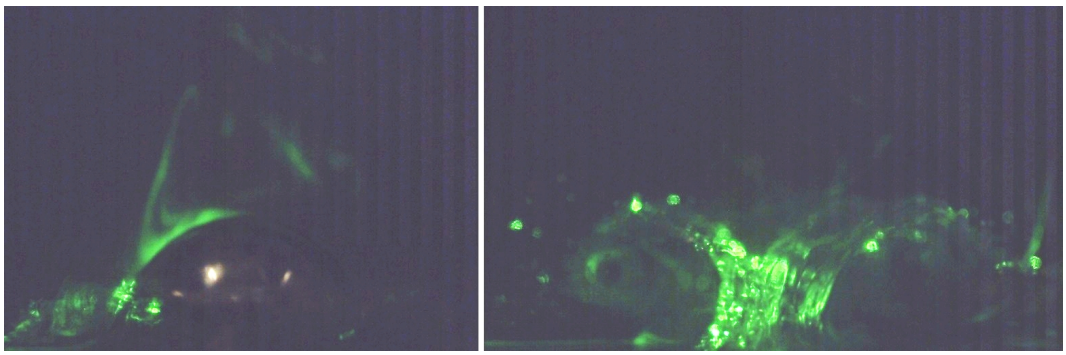

Fig. 4.4 Oil vapour and lasersheet visualisation of the gas flow behind a falling sphere (left) and the vortices formed behind the splash crown. The impact speed is $V \approx 1.6$ ms^{-1}, the liquid viscosity is 1.74 cP and the ambient gas is air at atmospheric pressure. The bottom of the image coincides with the free surface of the liquid. Video #8 in the supplementary videos.

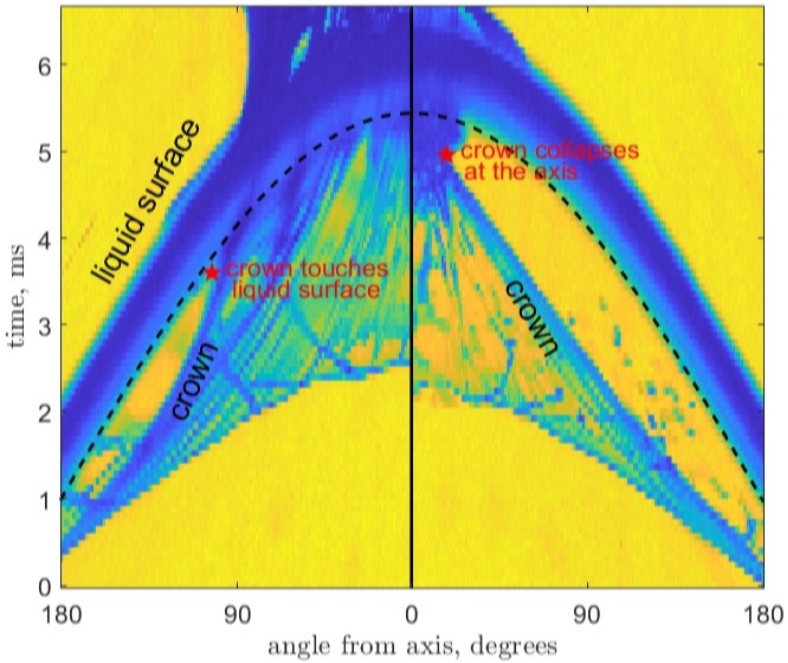

Fig. 4.5 Spatiotemporal image of the curtain propagating towards the pole in the experiments shown in Fig. 4.2 (left-hans side is air at $p = 525$ mbar and right-hand side is air at $p = 500$ mbar). The dashed line indicates the position of the free liquid surface. At lower gas density (right), the crown deceleration is not sufficient to prevent collapse at the pole. At higher gas density (left), deceleration is higher and the liquid surface overtakes the crown, forming a cavity.

arch represents the advance of the horizontal liquid surface along the sphere and its shape is dictated by basic geometric considerations. The root of the crown is seen to decelerate and is either overtaken by the liquid surface or collapses at the pole. In the first case, a cavity forms and in the latter case, the liquid surface closes at the top with no cavity as a result.

Since the difference in cavity and no-cavity cases occurs above the equator of the sphere and is determined by the dynamics of the thin splash crown, it is important to be able to obtain an estimate for this thickness [3]. For this purpose, blue dye was added to the liquid body. The thickness of the liquid sheet was measured using the ratio of the red pixel value to the total brightness. The measurements were calibrated using a wedge-shaped cuvette with known thickness (more information will be provided in Section 4.5). In Fig. 4.6, visible images of the splash are shown together with the corresponding colour maps on the right-hand side for thickness in μm. Red, green and blue pixel values were obtained for individual pixels using the Image Processing Toolbox available in MATLAB. The corresponding values for hue, saturation and brightness are then found in the same toolbox using standard formulae. In Figure 4.6, the raw optical image is shown along with the corresponding contour plot when value is found for every point in the image.

Combinations of different types of value can also be calculated and it was found that the red pixel value evaluated with image analysis at each pixel in the image divided through by the brightness (or value V) for that same pixel gives a clear variation across the entire length of the cell which can be compared with the images of the splash curtain obtained in experiments (shown in Figure 4.7).

Considering the variation of colour between the sphere and the edge of the splash crown, we estimate that the thickness is between 100 and 200 μm. If we take into account that the image is obtained by viewing through two layers of liquid, we estimate that the thickness of the liquid sheet is between 50 and 100 μm. Aristoff and Bush [90] previously suggested that the splash crown for water should have a thickness of approximately 200 μm, but this value was only chosen as it provided a best fit for their experimental data. The value which we provide is also consistent with the value of $\mathcal{O}(10\ \mu\text{m})$ which was proposed by Marston et al. [3] close to the top of a water splash crown. This value was determined using the Taylor-Culick velocity and the criterion that We ≈ 1 at the top of the crown where the liquid sheet disintegrates. We note that the estimate of the thickness is an order of magnitude estimate in both cases.

To this order of accuracy, it is not necessary to take into account deviations due to diffraction effects or curvature of the splash curtain, since the small areas which we consider are close to flat. The images used in Figure 4.6 were also not filtered during image processing. Furthermore, although there is a certain amount of spatial variation in the splash crown due to the presence of ribs or buckles, this may be neglected at the order at which we work. The presence of buckles in the splash curtain was similarly neglected by Marston et al. [3] when estimating thickness of liquid sheets. It can also be seen from Figure 4.6 that the thickness of the liquid sheet does not vary substantially when the curtain is viewed around the sphere or above the top of the north pole, so that time-dependence of the curtain is neglected in our estimate at the timescale with which the process occurs. Although the method outlined here involves many approximations, we can be confident of its accuracy to first order because of the consistency which we obtain with several previous estimates which used different methods [3, 90].

Finally, one might ask if the value obtained for the sheet thickness is only valid for the specific sphere diameter which was used for Figure 4.6. Evidence that the thickness is diameter-independent was found by Marston et al. [3], who obtained the following expression for the thickness δ of the splash crown

$$\delta = \frac{2\sigma}{\rho V_{open}^2}, \tag{4.1}$$

where V_{open} is the speed at which holes open in the crown during rupture of the crown walls. In reality, this method is only effective for estimating the thickness at the top of the

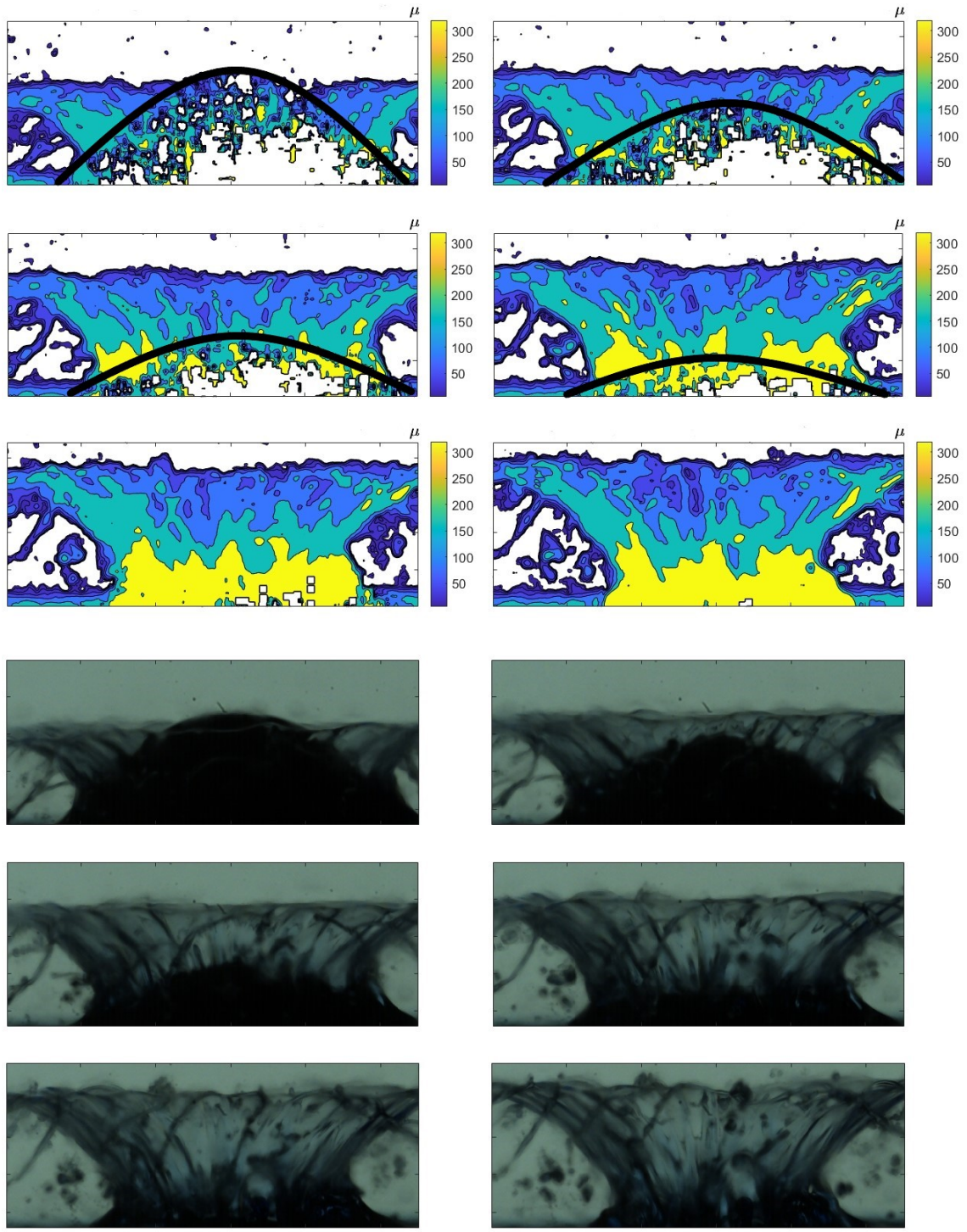

Fig. 4.6 Sheet thickness estimated using dyed oil. The contour maps for the sheet thickness are shown with the corresponding optical images. The experimental conditions are atmospheric pressure, impact speed $V = 1.6$ ms^{-1} and liquid viscosity $\mu_L = 1.74$ cP. The thickness across the main part of the splash curtain between the sphere and the edge of the liquid sheet can be estimated to be between 100 and 200 μm. Since light passes through the sheet twice, the thickness of the curtain is estimated to be between 50 and 100 μm. The dark circle in the upper images indicates where the sphere is blocking the splash curtain such that any data in these regions should be disregarded.

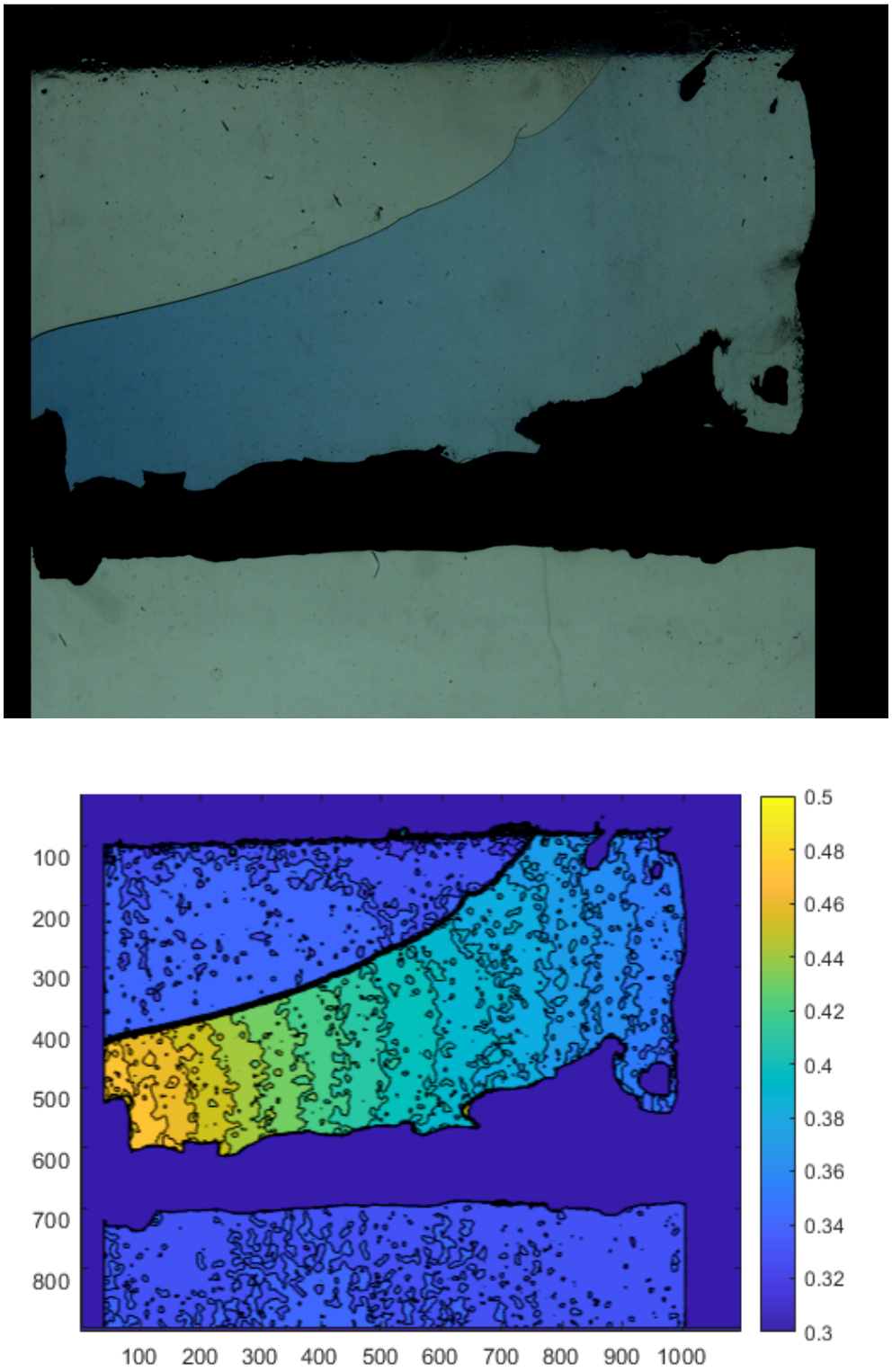

Fig. 4.7 Cuvette with known thickness (upper) and contour plot to show values of red pixel value divided by total brightness (lower).

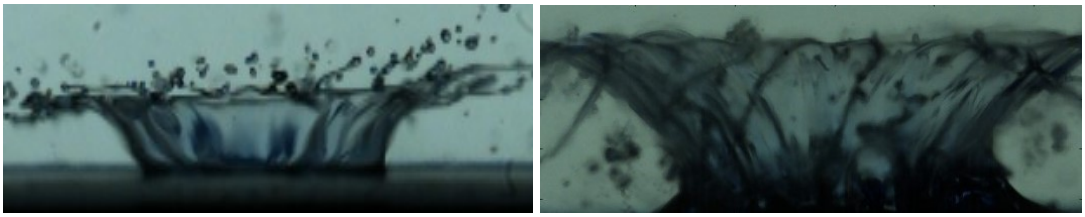

Fig. 4.8 (Left) splash curtain for a sphere of radius 4 mm and (right) splash curtain for a sphere of radius 7.5 mm. The liquid viscosity is 1.74 cP and the gas used is air at ambient pressure. A patch of coloured curtain has the same average green pixel value up to 4 units, leading us to argue in conjunction with the estimate of Marston et al. [3] that the thickness of the splash curtain is diameter-independent for the range of diameters which we consider.

crown, since this is the part where holes typically open. As a check, in Figure 4.8 we show the splash curtain using dyed oil and spheres with diameter 8 and 15 mm. Calculating the average green pixel value for a small flat patch on the curtain, we find that in both cases the average value is the same within 4 units. In combination with the expression for the thickness estimated by Marston et al. [3], this is sufficient to argue that the thickness of the splash crown is diameter-independent across the range of sphere diameters which we use in our experiments up to the order of magnitude considered.

4.2 Sphere Diameter

In Chapter 2, we have argued that the threshold speed for splashing across a range of sphere diameters is due to the fact that the formation of a splash curtain for all diameters used. In Figures 4.9 and 4.10, we show an event beneath the threshold speed for cavity formation at atmospheric pressure with sphere diameters between 2 and 15 mm. In Figures 4.11 and 4.12, we show an event above the threshold speed for cavity formation at atmospheric pressure with sphere diameters between 2 and 15 mm. It can be seen in Figure 4.10 that for large spheres, almost exactly the same process is seen, so this process scales well when going from 15 mm to 8 mm. In Figure 4.9, the quantity of liquid which is displaced is much smaller, but the picture for 4 mm also looks very similar to the picture for 2 mm.

Similarly, in Figure 4.10 the splash curtain looks to be the same for 8 and 15 mm. In Figure 4.11, the splashing processes for 2 and 4 mm look similar to each other, although in this case a much smaller quantity of liquid has been displaced. As shown in Figure 4.8, it is possible to estimate the thickness of the liquid sheet for spheres of diameter 8 and 15 mm. In the experimental data set, spheres of diameter 2 mm were used as the minimum sphere size in order to show that our results extend to small spheres which are used elsewhere in the literature on sphere impacts [90]. For the images discussed here, we also use spheres with diameter 4 mm although this intermediate sphere size was not used for our data set.

Fig. 4.9 Left: Impact of 2 mm sphere at speed 1.5 ms^{-1} in air at atmospheric pressure and liquid viscosity 1.74 cP. Right: Impact of 4 mm sphere at speed 1.5 ms^{-1} in air at atmospheric pressure. Although it is difficult to see at such small sphere sizes, it can be observed that the liquid is rising up around the sphere towards the pole.

Fig. 4.10 Left: Impact of 8 mm sphere at speed 1.5 ms^{-1} in air at atmospheric pressure and liquid viscosity 1.74 cP. Right: Impact of 15 mm sphere at speed 1.5 ms^{-1} in air at atmospheric pressure. Note the similarity of the thin liquid sheet in both cases.

The main reason for this is that the splash curtain which we mentioned in Chapter 3 can be imaged and visualised more easily for this larger sphere size.

4.3 Contact Line Pinning

As discussed in Section 2.4, contact line pinning during cavity formation has been discussed many times in the literature [91]. In Figure 4.13, we show observations of filming beneath the sphere for cavity and no cavity events at the same speed. Figure 4.13 (left) gives a good visualisation of contact line pinning and Figure 4.13 (right) shows the formation of a hole beneath the free surface where the splash crown has sealed at the pole of the sphere.

Fig. 4.11 Left: Impact of 2 mm sphere at speed 1.8 ms^{-1} in air at atmospheric pressure and liquid viscosity 1.74 cP. Right: Impact of 4 mm sphere at speed 1.8 ms^{-1} in air at atmospheric pressure. Although it is difficult to see at such small sphere sizes, it can be observed that the fluid is departing away from the surface of the sphere as it rises upwards so that a cavity eventually forms.

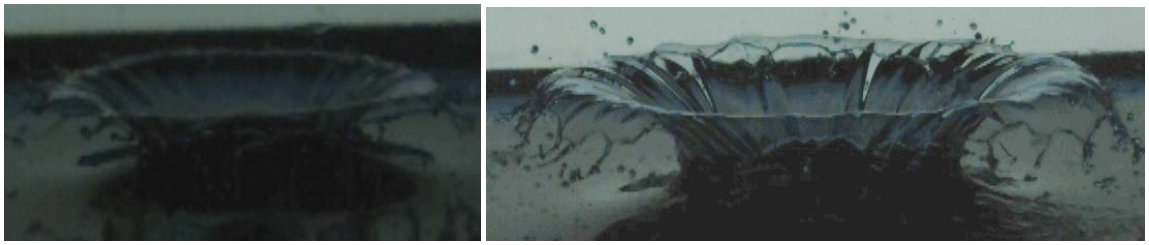

Fig. 4.12 Left: Impact of 8 mm sphere at speed 1.8 ms^{-1} in air at atmospheric pressure and liquid viscosity 1.74 cP. Right: Impact of 15 mm sphere at speed 1.8 ms^{-1} in air at atmospheric pressure. The similarity of the splash crown at these large sphere sizes suggests that the mechanism for cavity formation does not differ over this range of diameters.

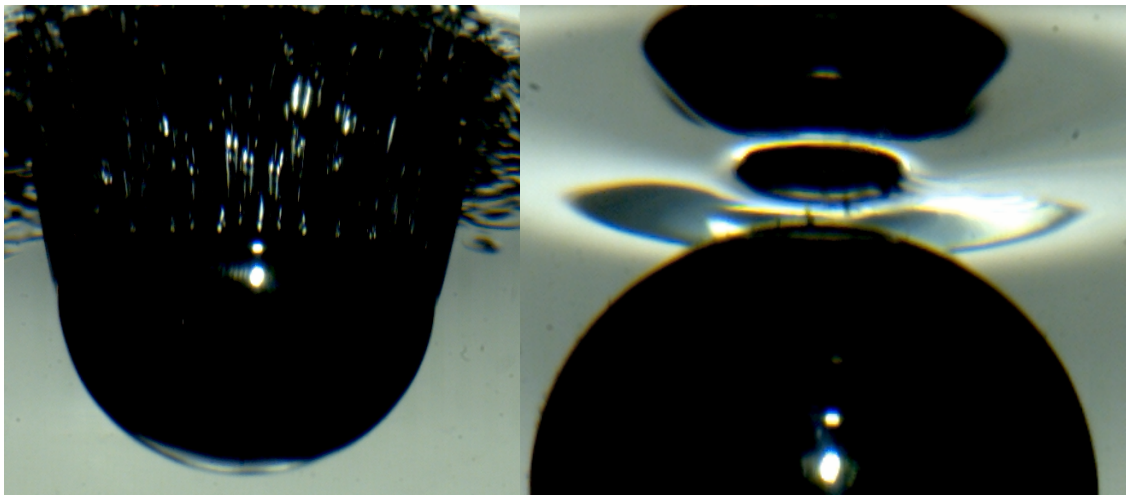

Fig. 4.13 Left: Impact of 15 mm sphere at speed 2.5 ms^{-1} in air at atmospheric pressure and liquid viscosity 1.74 cP. Right: Impact of 15 mm sphere at speed 2.5 ms^{-1} in air at one fifth atmospheric pressure. In the first case, contact line pinning at the equator can clearly be seen, leading to cavity formation. In the second case, it can be seen that fluid has gathered at the pole and cavitation bubbles have formed.

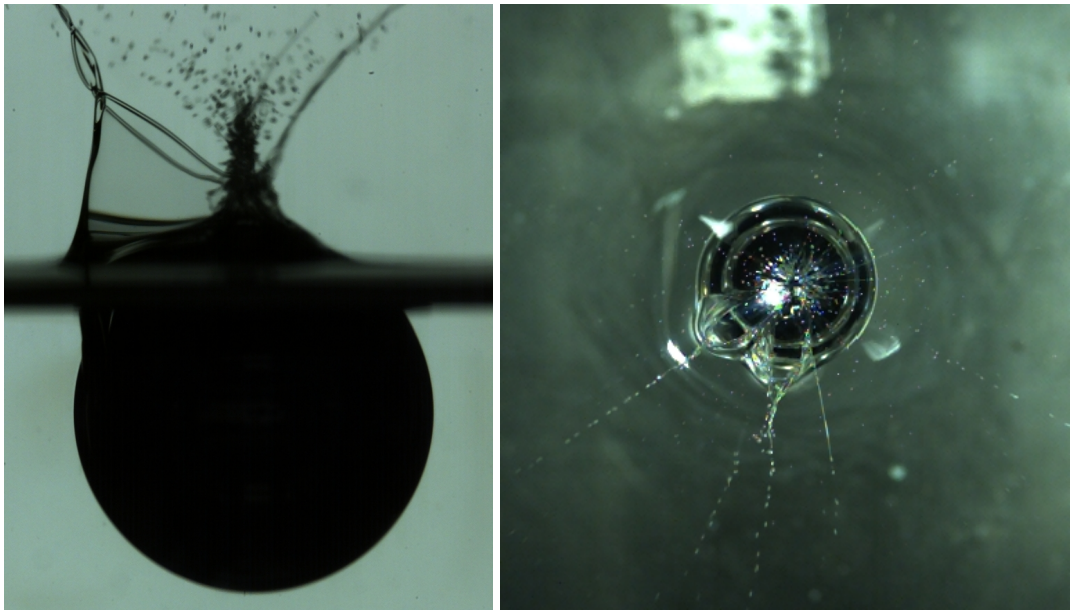

Fig. 4.14 Asymmetric splash at low gas density at higher impact speed: Formation of cavities on one side while the most of circumference is cavity-free. $V \approx 2.8$ ms^{-1}, $\mu_L = 1.74$ cP, the gas used is helium, $p = 138$ mbar (left) and $p = 200$ mbar (right). Videos #6 and #7 in the supplementary videos.

4.4 Instabilities at Low Gas Density

An interesting feature of our experimental results which can be seen in Fig. 3.6 is that the threshold hold speed forms a plateau once one goes below a density of one-fifth atmospheric density. We suggest that this plateau at low gas densities is due to the fact that in this regime the surrounding gas does not slow the crown and that there are instead instabilities such that a cavity almost always forms for sufficiently fast impacts on the liquid surface. In Fig. 4.14, the case where the crown gathers at the pole is shown for low gas density. However, the contact line propagation becomes unstable at a certain point on the equator and the flow separates, creating an asymmetric cavity.

Effects on cavity formation from spinning motions of the sphere are generally not important at the relatively low impact speeds which we work with [126], so we suggest that the formation of an asymmetric cavity at low gas densities is due to instabilities of the flow. A piece of evidence for this is that at high threshold speeds of 2.9 ms^{-1} and $\rho/\rho_{atm} = 0.2$ kg m^{-3}, there is one occurrence of a no cavity event in Figure 3.5 which is so high above the threshold speed it cannot be due to experimental uncertainties. This suggests that the plot should continue to slope upwards but plateaus because lowering the gas density cannot overcome the instabilities. In Figure 4.14, we show images of the instabilities. A wedge-shaped bubble forms as fluid departs the sphere and notably, one sees that more than one bubble can form on the side of the sphere. For comparison, we

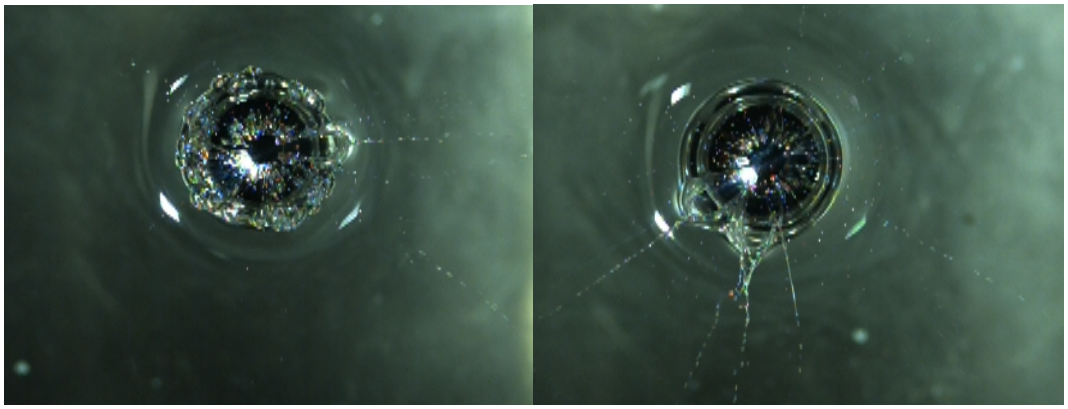

Fig. 4.15 Left: Sphere impact at 0.12 times atmospheric pressure, impact speed 2.9 ms^{-1} and viscosity 1.74 cP. Right: Impact at 0.2 time atmospheric pressure and impact speed 2.9 ms^{-1}. In the first image, it can seen that the instability causes to liquid to depart from the surface at one point, whereas in the second image, the liquid departs at more than one point.

show in Figure 4.15 (left) one bubble as viewed from above, whereas two bubbles can be distinguished in Figure 4.15 (right).

The instability which we observe is obviously distinct from the usual contact line instability, since it is only present at one or several localised points around the equator of the sphere. We suggest that it is instead a type of ribbing instability which is known to occur when a cylinder rotates on the free surface of a liquid body [127–129]. Above a critical value of the capillary number, the two-dimensional flow is unstable and the stable state appears to be a steady, three-dimensional flow whose thickness is periodic in the transverse direction. As evidence for this, we note that Marston et al. [3] found that the number of buckles N in a splash crown follows a relation $N \sim D^{3/4}$.

Using as input $D = 15$ mm, we obtain $N \approx 7.6$ which matches the fact that around 8 bubbles would fit around the sphere in Figure 4.14 (right). Since the pattern of buckles which appear in the buckling instability of the splash crown is known to be connected to the periodic saw-tooth pattern of the contact line (except for the case of Leidenfrost spheres), we suggest that the instability which we see at low gas densities is due to onset of a ribbing instability for the contact line which causes formation of a cavity . We are not able here to provide a theoretical criterion to determine a critical capillary number for onset of the ribbing instability. Such a criterion has been found for two cylinders rotating towards each other on a liquid surface, but in that case the critical number depends on the diameter of cylinder and the contact line is negligible since the cylinders are partly submerged [128].

4.5 Optical Measurements of Liquid Sheet Thickness

We now describe the theory and background behind our optical measurements in more detail.

4.5.1 Introduction

A topic of central importance in industry and fluid dynamics is the possibility of experimentally measuring thicknesses of liquid films on the microscale. This is generally a very difficult task and countless techniques have been proposed over the past hundred years based on various physical principles and depending on the flow [130, 131]. Existing experimental methods are sophisticated and can be broadly divided into four classes: acoustic, nucleonic, electrical (including conductance-based and capacitance-based methods) and optical (including interface detection, light attenuation, and laser displacement) [131]. Optical methods are relatively straightforward and simple compared to the other possibilities, so unsurprisingly there have been many proposals for optics-based techniques to measure film thicknesses. These include techniques based on optical interferometry, fluorescence methods, diffusing light photography, and light absorption methods [132–136].

In this section, a simple optical method is proposed for estimating thickness of a silicone oil film below 1 mm using coloured dye. In Section 4.5.2, the experimental set-up is described and in Section 4.5.3, the results are analysed to show that a relation can be obtained between liquid thickness and certain of the RBG and HSV variables. Our method is quite close to that of Kim and Kim [136], but note that their method uses photochromic dyes which are activated via irradiation with a laser, whereas the experiment proposed here does not require lasers or fluorescent dyes. However, the method described here is only useful for estimating the thickness and cannot be used to perform accurate measurements [137].

4.5.2 Experimental Set-up

Two transparent glass slides with height 7.7 cm, width 5.1 cm and thickness 0.1 cm are fixed so that they stand upright. The gap thickness between the top of the slides is measured to be 1 mm and the thickness decreases linearly as one goes to the bottom of the slides, where the gap thickness is measured to be 0.1 mm. The images captured were taken using a Photron FASTCAM SA-X2 high-speed video camera in snapshot mode, but a more basic camera can be used. Backlighting is provided by a single light source of luminance 178,256 cd m^2 and uniformity 99.44%. The experimental set-up with the light and camera is shown in Figure 4.16. The total gap thickness is then filled with 2 cSt silicone oil which has been dyed using Solvent Blue 14. The spacing between the top of the slides is fixed

Fig. 4.16 Experimental set-up showing camera and pair of glass slides.

and the slides are glued in place, as otherwise surface tension from the liquid in the gap will pull the plates together. The slides are sealed at the bottom and sides to prevent liquid from draining out as the gap thickness is filled. The deviation in the path of a light ray at different heights due to the angle of contact at the bottom is assumed to be negligible as the plates are extremely close to being parallel.

The concentration of the dye is chosen such that a clear difference in brightness can be observed as one moves from the bottom to the top of the slides. Note that the same concentration used in the calibration with the slides must then always be used in experiments if one wishes to estimate the thickness of a liquid sheet during an impact. Here for calibration purposes 0.038 g of dye powder is dissolved in 30 ml of silicone oil. The same amount of dye must be scaled up when dying an entire liquid bath which is then used to study liquid sheets ejected during sphere impacts or similar phenomena. The measurements were performed at ambient temperature and ambient pressure.

4.5.3 Results

Figure 4.17 shows visible variation in the ‘brightness’ of the blue colouring as one moves from the bottom to the top of the cell. To begin, a strip is chosen from the bottom to the top of the plates for analysis. There is some ‘noise’ in this spectrum, but this is avoided by choosing a strip from left to right during image processing which avoids noise fragments.

The aim is to show that certain properties can be related approximately linearly to the gap thickness, at least for sub-millimetre thicknesses within certain ranges. As expected, the blue pixel value cannot be used to obtain any useful information, as seen in Figure 4.18. In Figures 4.19 and 4.20, the red and green pixel values, respectively, are plotted against gap thickness. It can be seen that the relation for the red pixel value is close to linear between 0.3 and 0.8 mm and that the relation for the green pixel value is close to linear between 0.2 and 0.7 mm. Vertical uncertainty bars indicate the variation in pixel value which may be obtained as one move horizontally across the same height on the colour strip. The thickness at different parts of the cuvette placing the two slides at angle until the gap at the top is measured to be 1 mm from a magnified image and the gap at the bottom is measured to be 0.1 mm. Since the two slides are in contact at an angle at the bottom, the variation in thickness in going from 0.1 to 1 mm is approximately linear so that the amount of dye may be related linearly to the thickness. It is estimated that the uncertainty in thickness when determined this way is of the order of 10% (included as horizontal error bars).

The RGB values are then converted to HSV values, where H is the hue, S is the saturation, and V is the value (roughly corresponding to a brightness scalar). In Figure 4.21, the value is plotted against gap thickness and it is again found that no useful information can be obtained in this case. In Figures 4.22 and 4.23, the hue and saturation, respectively, are plotted against gap thickness. It can be seen that the hue is not useful for obtaining a linear relation, or at least not in any ranges which are not already available using RGB values. However, for the saturation the relation is approximately linear over a wider range than that accessible for RGB values (between 0.2 and 0.8 mm). Since the concentration which we have used is known, one can scale the amount of dye used and apply it to a larger liquid body. The liquid sheets during impact can then be studied using high-speed photography. The calibration could also be repeated with different concentrations if necessary, which may also depend on the liquid.

In other words, a dye method can be used to estimate thickness of liquid sheets within a reasonable range below a thickness of 1 mm and a lower thickness of around 0.2 mm. Although this does not cover many much smaller thicknesses which would be of interest when studying very thin liquid films, it allows one to study a range of thicknesses which can regularly occur during study of droplet impact and sphere impact problems. Estimating the thickness of these sheets is generally a very hard problem owing to the transient nature of the phenomenon and the difficulty involved in obtaining useable images from high-speed photography. Many methods do exist for performing accurate measurements but these are sophisticated and would not necessarily be available or even viable in all laboratories.

A weakness of the method described here is that it will probably fail to give a good estimate once the liquid sheet becomes very thin. As mentioned in the Introduction, this will be problematic when considering the very top of the lamella during a sphere

impact, although it could potentially be used elsewhere on the lamella closer to the sphere. However, the method does seem to give a close to linear relationship between thickness and optical properties of a dyed silicone oil sheet as long as one stays within a reasonable range which one would expect to see in an impact or liquid jet ejection event. One future possibility for obtaining accurate measurements would be to use a confocal chromatic sensor which points at the ejecting sensor. Such a device has been used previously to measure the film flow over a transparent surface [48]. Given the cost and difficulty of more sophisticated methods, a simple optical method such as the one which we have explained here is of interest and may also prove useful in experiments. It might also be possible to refine the experiment and use it to produce more accurate measurements, in which case it could then be a competitor to other more sophisticated dye-based methods in the literature [136].

4.6 Discussion

In this chapter, we obtained further experimental information on the influence of the properties of the ambient gas on cavity formation. It was confirmed that slight changes to gas density make corresponding changes to the speed of the splash crown and that changes to the mean free path do not influence the speed of the crown. Experiments were performed to show that cavity suppression due to a decrease in gas density was not due to suppression of gas entrapment. This is consistent with previous work of Burzynski and Bansmer [49] on the related problem of droplet splashing for high Weber and Reynolds numbers, where it was found that entrapment of gas at the solid-liquid interface is not the mechanism which is responsible for splashing in these regimes. The presence of a plateau in threshold speed at low gas densities was discussed and attributed to a type of ribbing instability which could be considered in more detail in future work.

Since the only mechanism which we could find which could explain cavity suppression due to the density of the gas was the dynamics of the thin splash crown, it was necessary to perform estimates of the thickness of the crown. This was done using a optical method which was similar to but simpler than methods of Kim and Kim [136]. The method was described in detail and it was found that it can be used to estimate the thickness of the splash curtain for a 15 mm sphere to be of the order of $50-100$ μm. This estimate is roughly consistent with the value of $9-16$ μm which was found by Marston et al. [3] for the top part of a water splash crown where the sheet becomes thinner and the value of 200 μm which was suggested by Aristoff and Bush for the thickness of a water splash crown. An argument was also made that the thickness measurement is valid for all the

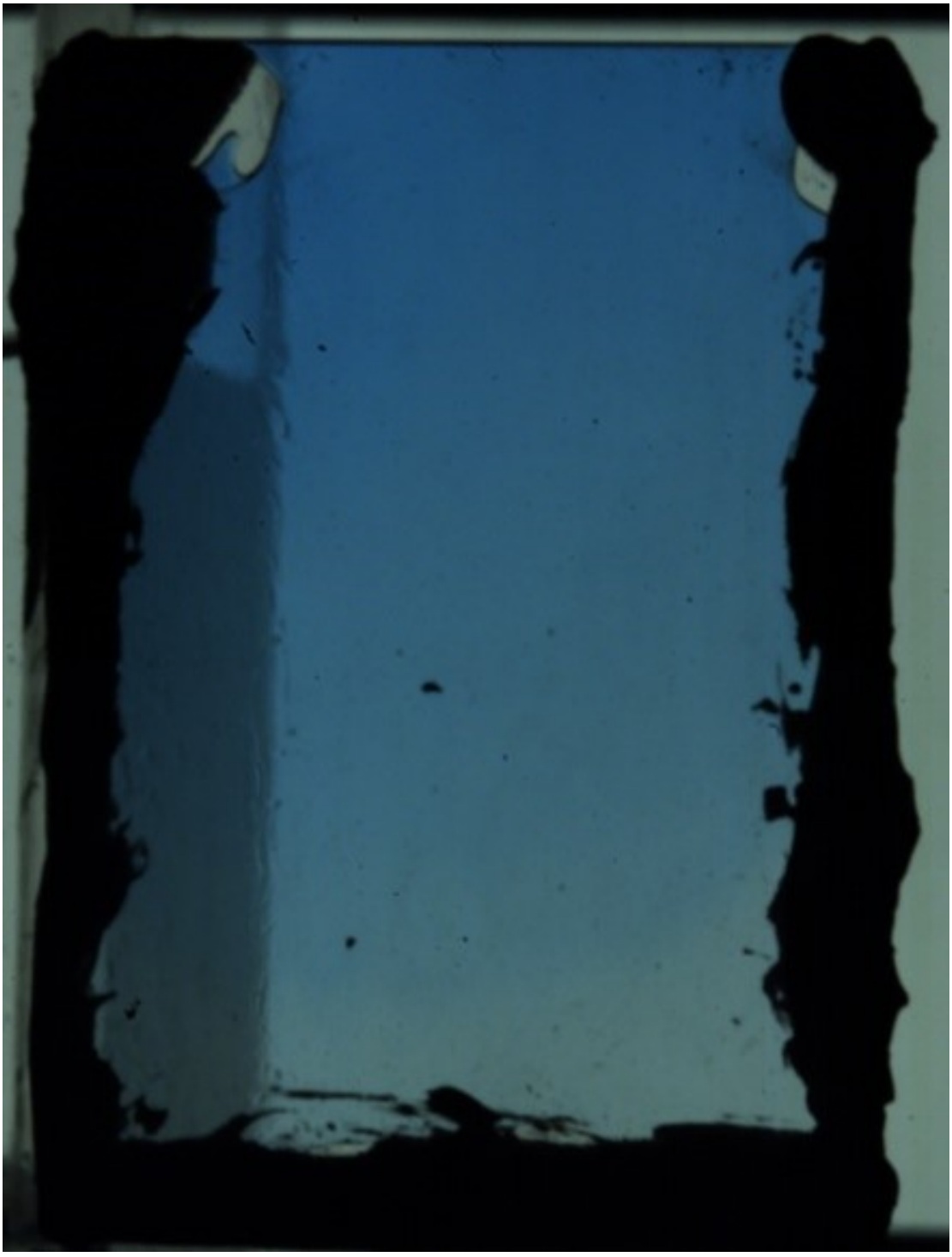

Fig. 4.17 Cell filled with dyed oil.

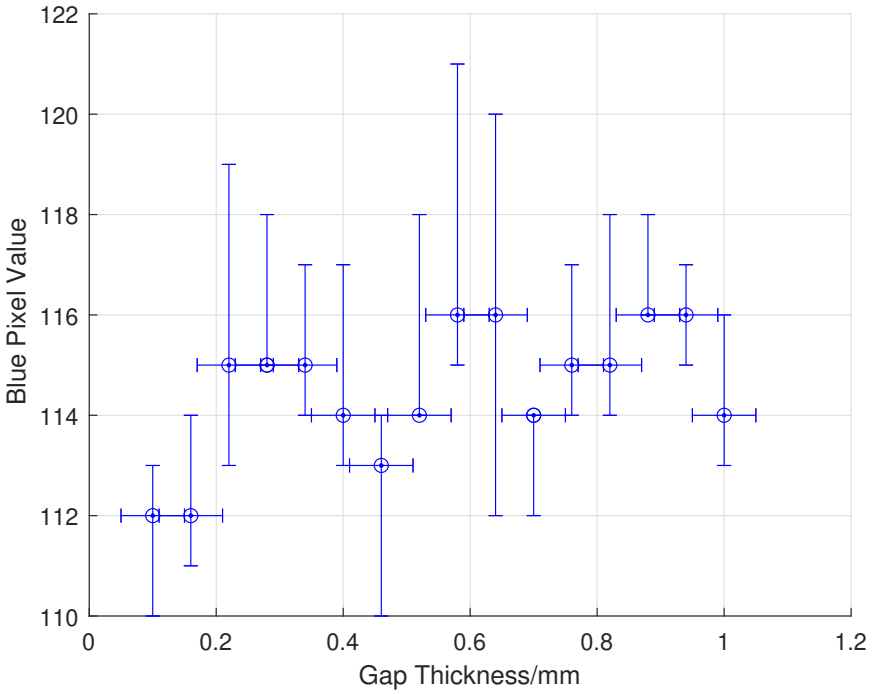

Fig. 4.18 Gap thickness against blue pixel value.

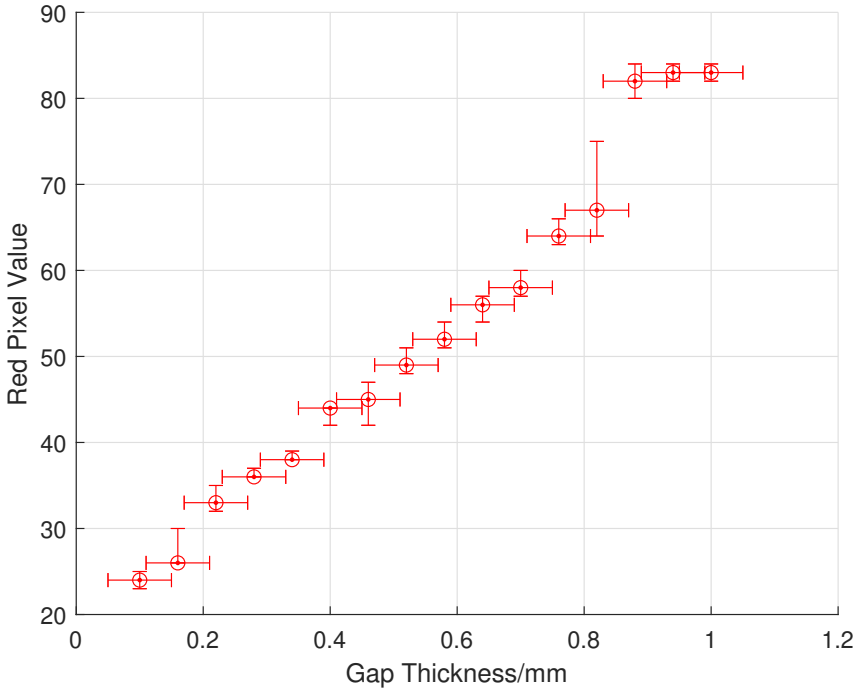

Fig. 4.19 Gap thickness against red pixel value.

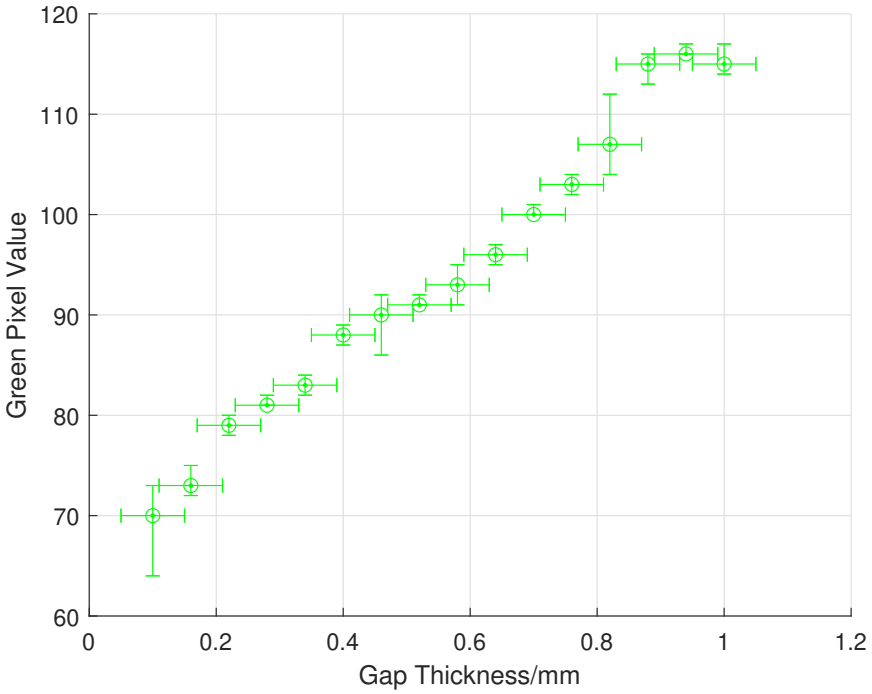

Fig. 4.20 Gap thickness against green pixel value.

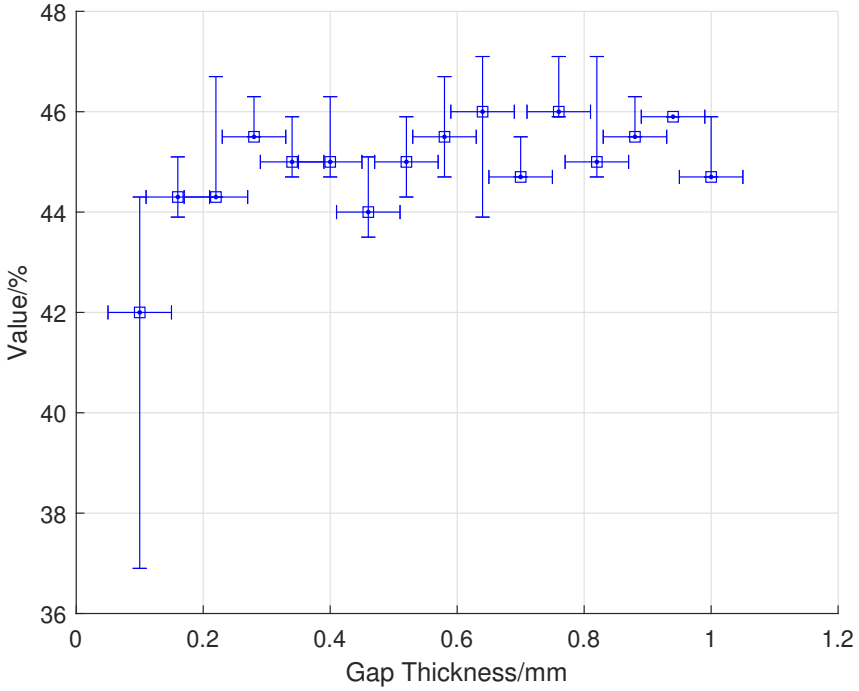

Fig. 4.21 Gap thickness against value.

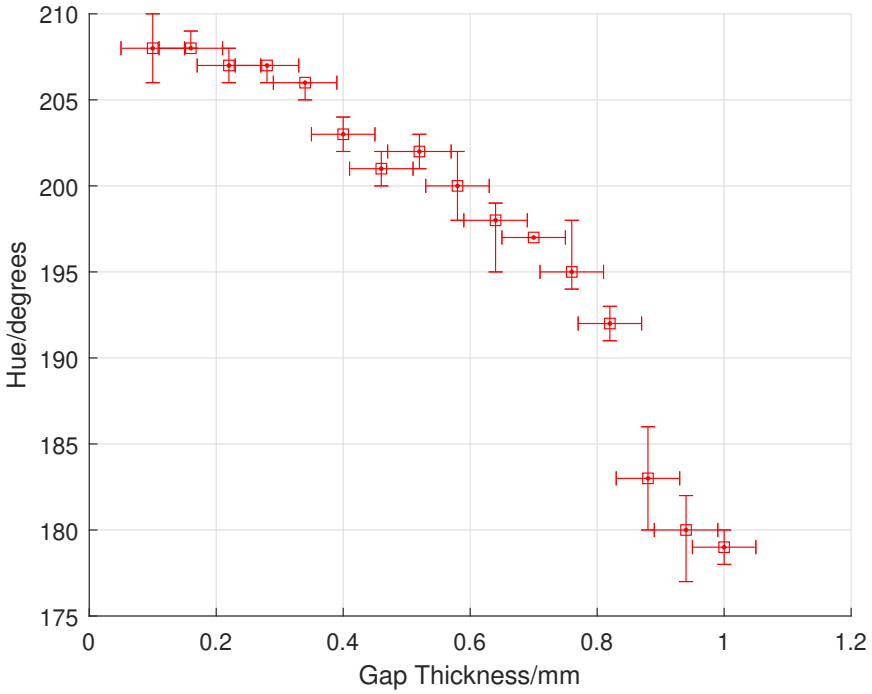

Fig. 4.22 Gap thickness against hue.

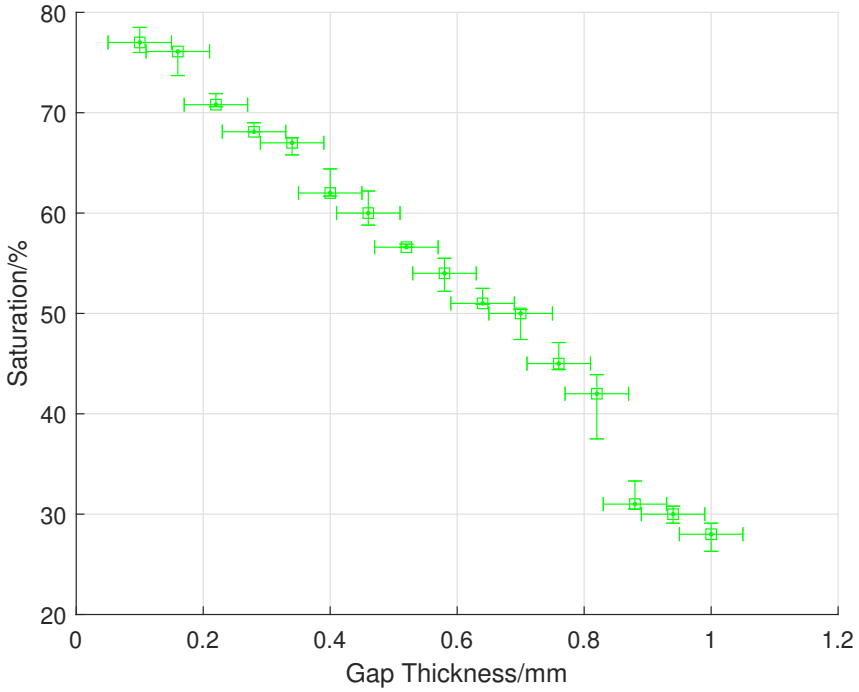

Fig. 4.23 Gap thickness against saturation.

sphere diameters used in our experiments, which is also consistent with the fact that the expression for sheet thickness of Marston et al. [3] is diameter-independent.

Chapter 5

Theoretical Interpretation and Numerical Simulations

5.1 Introduction

The discussion in the previous chapters has been mostly experimental and has not mentioned a theoretical interpretation of the results obtained. In this chapter, we will provide some estimates which support an argument that the phenomenon of cavity suppression can be attributed to the gas slowing sealing of the thin crown sheet behind the sphere. Another omission from our experiments is that we have only studied wettable spheres, not considering whether changing the gas density could have an effect on hydrophobic spheres. Although the flow structures involved during sphere-liquid impacts are complicated, developments in computational fluid dynamics have made it possible to perform accurate numerical simulations of water-entry phenomena, so in this chapter we will also carry out some preliminary simulations of the influence of gas density on water entry for hydrophobic spheres. The numerical results which we obtain support our theoretical argument for the influence of ambient gas density in the wettable case.

Since the development of sophisticated CFD techniques, there have been various numerical studies of solid impacts on liquid surfaces. Truscott et al. [138] used a boundary-element-type method to perform numerical simulations which accurately described the unsteady forces acting on spheres during free-surface water entry. Vehab et al. [139] employed a multiphase numerical model to study the physics of a frozen particle impacting the surface of a water bath. Lu et al. [140] carried out a numerical study of water entry of a semi-closed cylinder, whereas Hu and Liu [141] used a numerical method in conjunction with an interface-capturing VOF method to simulate velocity and pressure fields during water entry of a seafloor mining tool. Kleefsman et al. [142] performed numerical investigations of impacts of cylinders, cones and wedges with varying dead-rise

angles on a free body of water, comparing the resulting free surface dynamics with images from experiments and also comparing slamming coefficients with experimental results. Jalalisendi et al. [143], Xu et al. [144] and Wu et al. [145] have also performed numerical studies of unsteady flow characteristics in various three-dimensional water entry problems involving wedges and solid bodies which model ship hulls.

Returning to sphere impacts, Zhou et al. [146] used the VOF method to study the influence of entry speed and angle on water entry of hydrophobic spheres, finding that variation of both of these parameters influences the evolution of the shape of the cavity and the forces experienced by the body. Do-Quang and Amberg [147, 148] included the surface energies of the solid surface in order to capture dynamic wetting phenomena and were able to obtain very good agreement with the experimental results of Duez et al. [89]. Ahmadzadeh et al. [149] developed a three-dimensional numerical model of the solid-liquid impact using a coupled Eulerian-Lagrangian formulation. This model was successfully able to determine the shape of the cavity and the pinch-off time in agreement with the experimental results of Aristoff et al. [73].

This chapter is organised as follows. In Section 5.2, we outline an initial estimate regarding the size of the boundary layer thickness in our problem before briefly discussing the link with the Gordillo-Riboux model for droplet-solid impacts in Section 5.3. In Section 5.4, we outline the main possibilities for the dynamics of the splash crown. In Section 5.5, we present our argument for the modification of these dynamics by the presence of ambient gas. In Section 5.6, we carry out numerical simulations which enable us to investigate the role of the ambient gas in cavity formation of hydrophobic sphere impacts, finding that cavity formation in this case is not suppressed by lowering the ambient gas density. We finish with a discussion of results in Section 5.7.

5.2 Initial Estimates

A rough argument suggests that the boundary layer thickness in our problem is always much greater than the mean free path of the gas, which would seem to preclude an explanation in terms of the kinetic effects of the gas (or at least that such effects could be the dominant ones in this problem) [115]. If we assume the usual expression for a laminar boundary layer thickness δ at a flat plate, we then obtain

$$\delta \sim \sqrt{\frac{r\nu_{\text{air}}}{U}} = \sqrt{\frac{r}{U}\frac{\rho}{\rho_{\text{atm}}}\nu_{\text{air}}^{\text{atm}}}, \tag{4.1}$$

where U is the velocity of the outer flow. The mean free path of air is 68 nm in the case of ambient pressure, so if the density is varied by pulling a vacuum, the mean free path is

$$l = \frac{\rho_{\text{atm}}}{\rho} \cdot 68\,\text{nm}. \tag{4.2}$$

Substituting in representative values for r and U, one has for the ratio

$$\frac{\delta}{l} \approx 2000 \cdot \left(\frac{\rho}{\rho_{\text{atm}}}\right)^{3/2}. \tag{4.3}$$

This ratio only tends to 1 as ρ/ρ_{atm} tends to 0.006, an extremely low value which is never attained in Figure 3.5. One might initially wonder why the flow around a sphere is attached for very high Reynolds numbers in our impact case when such a steady flow on a sphere usually separates at around $\text{Re} = 20$. However, $5000/20$ is of a similar order to the ratio of the density of water to the density of air (700), which is relevant when discussing the adverse pressure gradient at the point of flow separation.

5.3 Link with Gordillo-Riboux Model

Figure 1.3 shows that there is a difference in the behaviour of the splash crown depending on whether or not a cavity forms, but it would be desirable to have some idea of the physics involved in this difference. Although the sphere impact problem is different to that of droplet splashing, there are some geometric similarities in the way that the lamella of the droplet spreads outwards and is lifted by the aerodynamic force due to the surrounding air during impact (see, for example, Figure 1 of [150]). These similarities might lead one to hope that some modification of the model of Gordillo and Riboux [18–20] might successfully be implemented for the sphere impact problem, providing a framework which can deal both with sphere impacts and droplet splashes. This is a highly non-trivial proposal, but one which would merit further study.

In particular, although the picture of Gordillo and Riboux [18] is focused on liquid drops impacting on a solid surface, the same scalings should be applicable. In the droplet impact problem at a critical impact speed, a liquid sheet or rim becomes detached from the main drop. In Fig 1.3 and in Fig 3 of [89] this seems to occur in all cases. The question is then whether the lift force away from the solid created by a gas lubrication layer is sufficiently strong to pull the liquid film back onto the sphere, with cavity formation following due to the opening up of an air gap when it is not strong enough.

At any rate, one might expect the simplifications we have just mentioned to break down at such a low gas density. It is likely that adaptation of the Gordillo-Riboux splash criterion [18] is possible along the lines which we have described, but due to the geometry of the sphere impact problem, we will take a slightly different approach which concentrates on the dynamics of the splash crown during impact and the way in which these dynamics

can be modified by the presence of the gas. It turns out that this approach does give a reasonable explanation for the influence of threshold speed on gas density which we see in the experiments, at least as a first approximation.

5.4 Dynamics of the Splash Crown

In this section, we will discuss the dynamics of the splash crown. We distinguish three main scenarios of sphere impact:

(a) The flow detaches from the sphere around the equator, forming a vertically growing crown as shown in Fig. 3.5a;

(b) The flow remains attached to the sphere, forming a crown which starts closing behind the sphere but does not reach the north pole due to being slowed down by the gas escaping from the cavity (Fig. 3.5b);

(c) The flow remains attached, forming a crown which closes at the axis behind the sphere before it is fully submerged below the free liquid surface (Fig. 3.5c).

We now proceed to sketch the dynamics of the splash crown shown in Fig. 5.1 and explain how it is altered by the ambient gas. The influence of liquid evaporation on droplet splashing at reduced pressure was previously ruled out [123, 124]. Similarly, liquid evaporation only influences contact line motion for sufficiently slow processes involving volatile liquids, so can be discounted [151]. The fact that the threshold speed only depends on density of the suggests that the effect is related to the dynamic pressure of the gas, i.e. to inertial effects. Furthermore, independence of the threshold on the radius of the sphere suggests that the effect might relate to deceleration of the crown sheet which slows propagation of the contact line.

Summarising the experimental observations discussed in Sections 3 and 4, we propose the following sequence of events on impact:

(1) The sphere displaces liquid which forms a collar as it rises up along the sphere. Viscous effects are negligible in the formation of the bulk of the collar as the liquid boundary layer thickness $\delta \sim \sqrt{\mu/\rho_{\mathrm{liq}} \cdot R/V_0} \sim 100\ \mu$m, whereas the thickness of the bulk of the collar can be estimated from Fig. 5.7 to be of the order of millimetres. We assume here that the speed of the liquid in the collar is of the same order of magnitude as the impact speed of the sphere [89, 152].

(2a) Due to surface tension, a rim appears at the leading edge of the collar, similar to that observed for vertical cylinders [82]. When the impact speed is sufficiently high, the flow separates from the sphere at the equator and a cavity forms with the crown failing to propagate along the surface as in Fig. 3.5a.

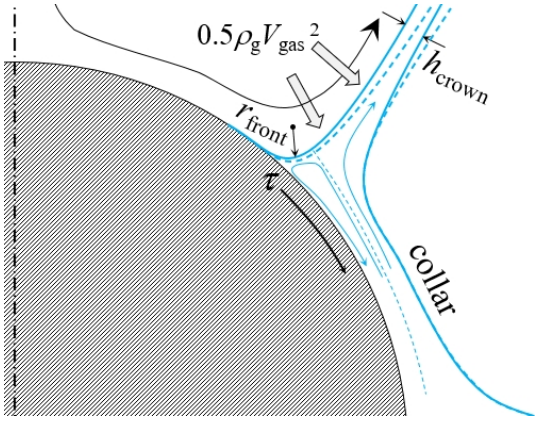

Fig. 5.1 Schematic in the frame of reference moving with the root of the crown. In the absence of the ambient gas, propagation of the front is defined by the balance between capillary pressure under the concave liquid surface and viscous forces. When the ambient gas density is high enough, it slows the crown (dashed line), which changes the shape of the curved interface and slows down propagation of the liquid front.

(2b) At lower speeds, the rim moves past the equator but starts to depart the surface due to centrifugal force. The splash crown then forms as shown in Fig. 5.1. In the absence of gas and surface curvature, the velocity of propagation of the wetting front V_{front} would be defined by the balance between the pressure created by the concave surface formed due to the sphere wettability and the viscous stress in the vicinity of the front [95, 17]:

$$\frac{\sigma}{r_{\text{front}}} \sim \frac{\mu V_{\text{front}}}{r_{\text{front}}} \Longrightarrow V_{\text{front}} \sim \frac{\sigma}{\mu} \tag{5.1}$$

which corresponds to $\text{Ca}_{\text{front}} \sim 1$ as reported in [89].

(2c) Below the threshold speed, the crown closes at the pole before the sphere is able to submerge and no cavity is observed.

To confirm the plausibility of relating the cavity formation to deceleration of the crown by the surrounding gas, we present an order of magnitude estimate of the stresses involved for impact speed $V_0 = 2$ ms^{-1} and $D = 15$ mm. The dominant term is the ambient pressure $P_0 > 5000$ Pa. This pressure provides continuity of the liquid so that the liquid displaced by the sphere moves up along the solid surface. The next term corresponds to the dynamic pressure of the liquid $P_{\text{liq}} \sim \rho_{\text{liq}} V_0^2/2 \sim 2000$ Pa. Besides this, we also have the dynamic pressure of the gas $P_{\text{dyn gas}}$. To evaluate this term, we assume that the speed of the splash crown Vfront relative to the gas V_{gas} is given by the crown speed in the frame of the sphere and add another factor of V_0 for the circulatory flow which forms behind the falling sphere. By considering Fig. 4.2, we estimate that the speed of the wetting front is of the order of double the impact speed of the sphere, so that $V_{\text{front}} \sim 2V_0$.

Measurements of the speed of the wetting front of Kubota et al. [152] confirm that this speed takes a maximum value which is always some small multiple of the impact speed. Empirical measurements indicate that the exact value for the multiplicative factor depends on how fast the sphere is travelling. Kubota et al. [152] found that in water, the maximum front speed at $V = 2$ ms^{-1} is around three times the impact speed of the sphere, whereas at $V = 2.5$ ms^{-1}, the maximum front speed rises to around five times the impact speed. This is also qualitatively predicted by the theoretical model of Duez et al. [89] for both hydrophilic and hydrophobic spheres.

From this we find that the dynamic gas pressure at which the cavity/no-cavity transition occurs is given by

$$P_{\mathrm{dyn\,gas}} \sim \rho_{\mathrm{gas}} V_{\mathrm{gas}}^2/2 \sim \rho_{\mathrm{gas}} (3V_0)^2/2 \sim 10 \text{ Pa}. \tag{5.2}$$

The radius of curvature of the advancing front r_{front} shown in Fig. 5.1 is defined by the balance of capillary force and centrifugal terms which accelerate fluid into the crown:

$$\frac{\sigma}{r_{\mathrm{front}}} \sim r_{\mathrm{front}} \rho_{\mathrm{liq}} \frac{V_{\mathrm{front}}^2}{R} \Longrightarrow r_{\mathrm{front}} \sim \frac{1}{2}\sqrt{\frac{\sigma R}{\rho_{\mathrm{liq}} V_0^2}}. \tag{5.3}$$

For sphere diameters between 2 and 15 mm, this estimate for r_{front} varies between 50 and 140 μm. The corresponding capillary pressure varies between 110 and 280 Pa.

The deceleration a_{stop} required for the crown moving at the speed of $2V_0$ to completely stop at the pole, moving a distance which is approximately equal to R, is

$$a_{\mathrm{stop}} \sim \frac{2V_0^2}{R}. \tag{5.4}$$

The deceleration of the crown due to the dynamic pressure of the gas is

$$a_{\mathrm{crown}} \sim \frac{P_{\mathrm{dyn\,gas}}}{\rho_{\mathrm{liq}} h_{\mathrm{crown}}}. \tag{5.5}$$

The exact shape of the liquid surface adjacent to the advancing wetting front depends on the angle which the root of the crown makes with the surface of the sphere and affects the speed of propagation of the wetting front. A sharper angle increases the curvature, increasing the capillary term in (5.1) and hence the speed of the front, whereas angles above 90° lower the curvature and the speed of the front. In this way, by slowing the crown, the ambient gas slows the wetting front, preventing it from reaching the pole before the falling sphere submerges below the surface.

Combining equations (5.2), (5.4) and (5.5), we arrive at

$$\frac{a_{\text{crown}}}{a_{\text{stop}}} \sim \frac{\rho_{\text{gas}} V_{\text{gas}}^2}{2\rho_{\text{liq}} h_{\text{crown}}} \frac{R}{2V_0^2} \sim 2\frac{\rho_{\text{gas}}}{\rho_{\text{liq}}} \frac{R}{h_{\text{crown}}} \tag{5.6}$$

As explained in previous sections, the thickness of the crown h_{crown} was measured experimentally, resulting in a value between 50 and 100 μm. At the set of parameters when the cavity/no-cavity transition occurs i Fig. 4.2, $a_{\text{crown}}/a_{\text{stop}}$ varies between 1 and 2, depending on the sphere radius R. This supports our hypothesis that the presence of the ambient gas shifts the threshold speed for cavity formation, resulting in an increase of the threshold capillary number Ca when going between 0.6 and 0.2 times atmospheric density. We emphasise that (5.6) is an order of magnitude estimate valid within the considered range of parameters and not a scaling.

5.5 Numerical Simulations

In our experimental work we have only used spheres with small contact angles, but it would be interesting to see if the properties of the gas have an influence on cavity formation in the case of hydrophobic spheres. The estimates and mechanism proposed in Section 5.4 suggest that lowering the ambient gas density would likely not suppress cavity formation in this case, since if the sphere is hydrophobic the contact line departs the sphere due to a contact line instability. We propose to investigate this question numerically and in the next section we describe the simulations which we performed of hydrophobic spheres impacting a liquid surface in the presence of ambient gases with varying density. The main conclusion which we draw from the simulations is that cavity formation cannot be suppressed by lowering the ambient gas density in the case where a sphere is hydrophobic such that it forms a cavity at any impact speed under atmospheric conditions.

5.5.1 Methodology

In the simulations it was assumed that the liquid is incompressible and that the process of impact and entry is carried out at room temperature. The liquid follows the equations for conservation of mass and momentum. A VOF (volume of fluid) Eulerian multiphase model was used with fixed meshes to capture the position and deformations of the multiphase interface. The distributions of the liquid and gas phases and the positions of the interface for the free surface are described by field functions for volume fraction α_i

$$\alpha_i = \frac{V_i}{V},$$

where V_i is the volume of phase i in the control unit and V is the volume of the control unit. The volume fractions for both phases in cell must add up to unity:

$$\alpha_w + \alpha_a = 1,$$

where α_w is the volume fraction for the water phase, α_a is the volume fraction for the gas phase, and $\alpha_i = 0.5$ may be used for the gas-liquid interface.

The range of Reynolds numbers $\mathrm{Re} = \rho_l V d/\mu_l$ used in the study was between 1.1×10^4 and 4.7×10^4, which puts the flow in the turbulent regime. However, the boundary layer itself is not turbulent and the short time scale of the process studied implies that the rest of the domain would not have time for turbulence to develop, hence we do not include turbulence in the simulations. The Reynolds-averaged Navier-Stokes (RANS) method was used with VOF Waves to define a static water wave and capture features of the free liquid surface. The finite volume method was used to transform the mathematical model into a system of algebraic equations. In this transformation, the governing equations of motion are discretised in space and time and since the flow is unsteady, the time interval for the entire process is divided up into timesteps Δt. By integrating the transport equation over a control volume and applying the standard divergence theorem, an integral form is obtained for the transport equation [153]

$$\frac{d}{dt}\int_V \rho\phi \, dV + \int_A \rho v\phi \cdot d\mathbf{a} = \int_A \Gamma\nabla\phi \, d\mathbf{a} + \int_V S_\phi \, dV,$$

where ϕ denotes transport of a scalar property, A is the surface area of a control volume and $d\mathbf{a}$ is the surface vector. The first term in the equation denotes the rate of change over time of a fluid property ϕ inside a control volume, the second term captures convective flux of a fluid property ϕ across boundaries of control volumes, the third term captures diffusive flux, and the fourth term is the source term.

In this study, to enable a comparison with the simulations of Zhou et al. [146], a hydrophobic sphere was used with diameter $d = 0.042$ m and mass $m = 0.09$ kg. The sphere dropped under gravity from a position at rest above the water surface, impacting the water with an initial speed V which was varied between 0.23 and 1 ms^{-1}. The z-axis passed through the centre of the sphere and the negative direction was used to define the reference value for the acceleration due to gravity. The initial moment of time was defined to be the moment at which the sphere begins to fall under gravity. Dynamic fluid-body interactions were used to model the interactions between the liquid and the sphere, where the sphere was modelled as a six degree of freedom 3D continuum body. The sphere is placed at the origin of a moving coordinate frame which is associated to the angular velocity, centre of mass, moment of inertia, orientation and velocity of the sphere.

The DFBI technique allows us to model the motions of a rigid body due to applied forces and moments. This was combined with the overset mesh technique, which is used to model moving parts. The overset mesh contains the rigid body and was superimposed over a stationary background mesh. Depending on the position of the cells within the computational domain they can be used as active, passive, and acceptor cells. Active cells are the cells which are used for the simulation. The governing equations for the fluid flow are solved within these cells, whereas the equations of motion are not solved within the passive cells. Acceptor cells are those which are located between active and passive cells to facilitate interpolation of information between the overset and background meshes. To minimise errors in interpolating variables between the background and overset meshes, the same order of magnitude of grid density was used in the overlapping regions of the two meshes. To achieve this, a volumetric control was set up at the overlapping part of the two mesh regions. An overset interface was created between the background and overset mesh regions, with linear interpolation used at the interface. 10 layers of prism grids with a total thickness of 0.0005 m were used for the wall boundary of the sphere. The background, overset, transition and prism layer meshes are shown in Figure 5.2. The free surface was defined based on the VOF wave and the VOF multiphase flow model was solved using a second-order implicit scheme. Since we used the VOF approach to resolve the shape of the free surface, local mesh refinement was applied at the free surface. The refinement normal to the undisturbed free surface was made by discretising the free surface in the vertical direction using 30 cells per wave height, whereas the free surface was discretised in the horizontal direction using 120 cells per wavelength.

For the background domain, a velocity inlet and pressure outlet were used as boundary conditions, whereas a symmetry boundary condition was used for the symmetry plane. For the overset mesh, an overset mesh condition was used as boundary condition and a symmetry boundary condition was used for the symmetry plane. An important point is that the same type of boundary condition must be used for boundaries of both the background and overset domains which are coplanar. Field functions were used to define both initial and boundary conditions, where the hydrostatic pressure of the VOF wave was used to define both the initial and boundary conditions for the pressure. To ensure fidelity of the results obtained using the Reynolds-averaged Navier-Stokes equations, a time step ($\Delta t = 0.001s$) for subsequent times in the simulation was chosen such that at each step the overset mesh moved a distance which was smaller than the size of the smallest cell in the background mesh. The temporal discretisation was chosen to be second order.

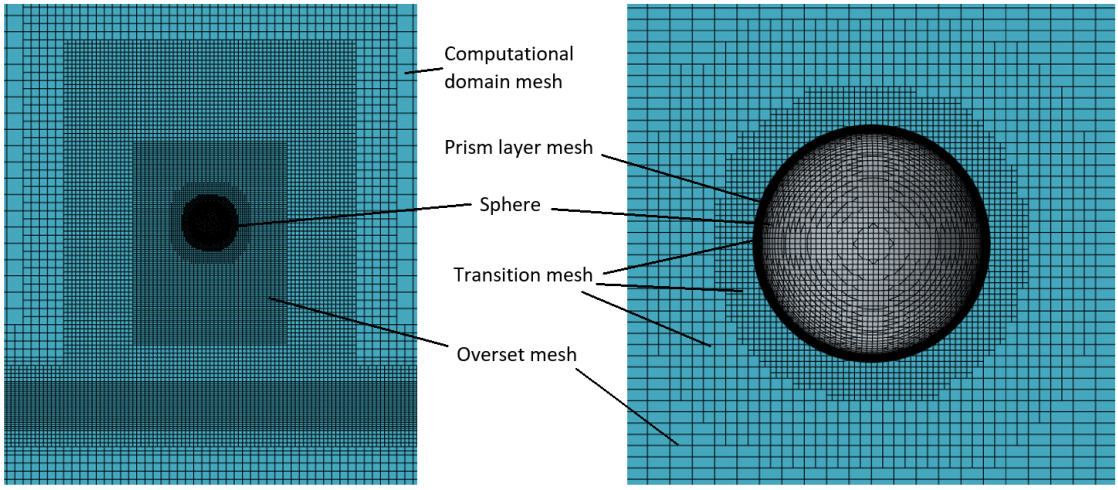

Fig. 5.2 Mesh generation in computational domain.

5.5.2 Validation and Results

To verify the accuracy of the numerical model, we performed simulations with the same parameters used by Zhou et al. [146] and tested agreement with their results. The results of Zhou et al. [146] were validated by checking them against corresponding experiments which used the same parameters and initial conditions for entry speed. The numerical results for cavity shape and sphere position at different moments over time were compared to experimental images of the cavity obtained used a high-speed camera. The displacement and velocity in horizontal and vertical directions were also compared with experiment. The agreement obtained was almost perfect, where the maximum error for displacement was found to be 3.8% for the horizontal displacement at $t = 0.112$ s. In terms of velocity, the numerical results were consistent with experimental results, with a maximum error of 4.1% in the horizontal direction at $t = 0.112$ s.

In Figures 5.3, 5.4 and 5.5, we perform simulations of the sphere impact using the same parameters as Zhou et el and compare with their results on cavity evolution at various characteristic times. In Figure 5.3, an impact speed of $V = 0.5$ ms^{-1} was used and good agreement was found, with almost exact agreement on the shape of the cavity after cavity closure at $t = 0.135$ s. This is the part of the process which most interests us, so it is important that we can find good agreement here. The same qualitative features are observed, including the presence of cavity stretching and cavity closure, with a length associated to each process. In Figure 5.4, we use an impact speed of $V = 0.75$ ms^{-1} and find agreement, with very good agreement on the shape of the cavity at the exact moment of closure at $t = 0.125$ s. The qualitative phenomena are captured, including the presence of a jet during cavity closure. Finally, in Figure 5.4, we use an impact speed of $V = 1$ ms^{-1} and compare with the results of Zhou et al., finding very good agreement for the

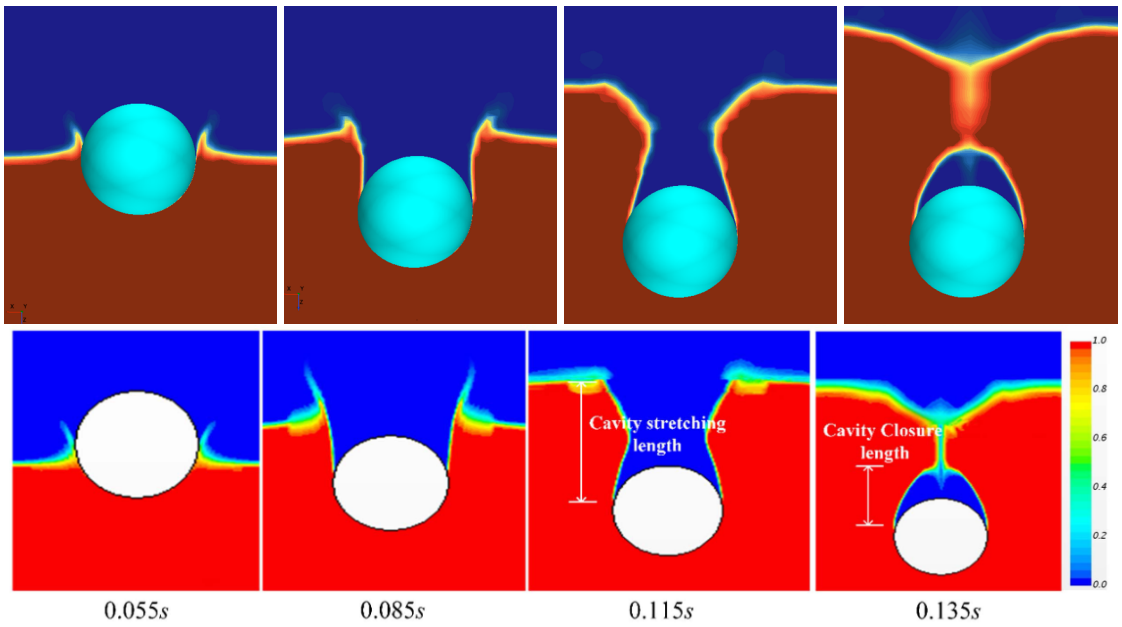

Fig. 5.3 Evolution of the cavity during impact of a 42 mm hydrophobic sphere on water at speed $V = 0.5$ ms^{-1} and atmospheric air density. The colour map indicates the volume fraction of water. The top row shows the results obtained using our VOF model and the bottom row shows the results of numerical simulations of Zhou et al. [146].

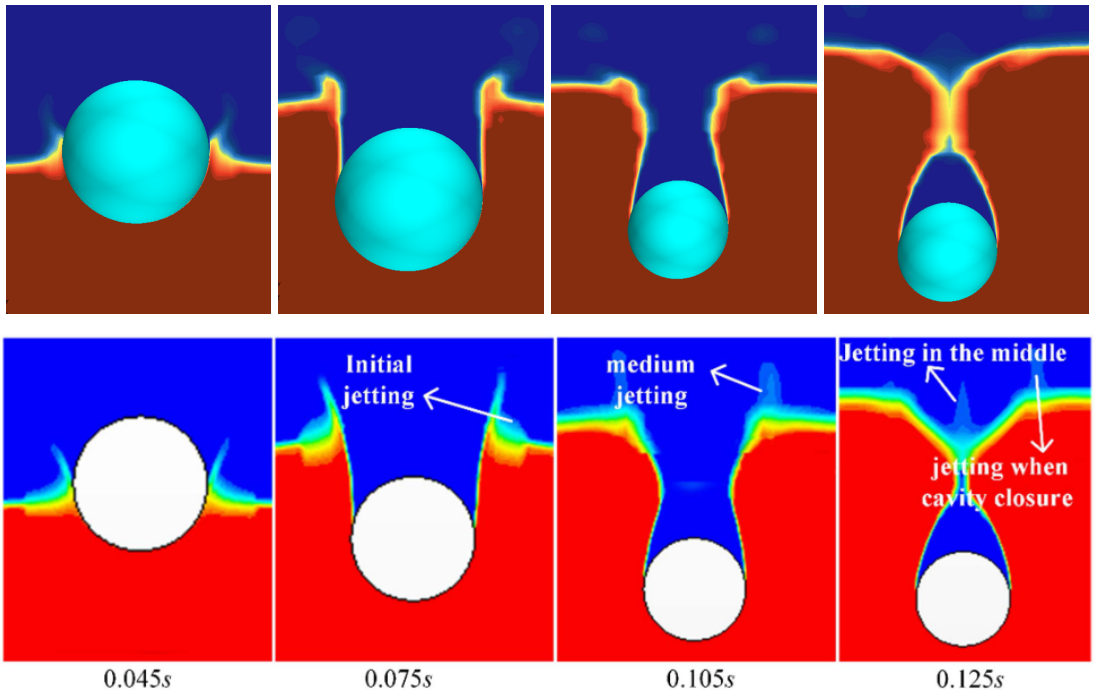

Fig. 5.4 Evolution of the cavity during impact of a 42 mm hydrophobic sphere on water at speed $V = 0.75$ ms^{-1} and atmospheric air density.

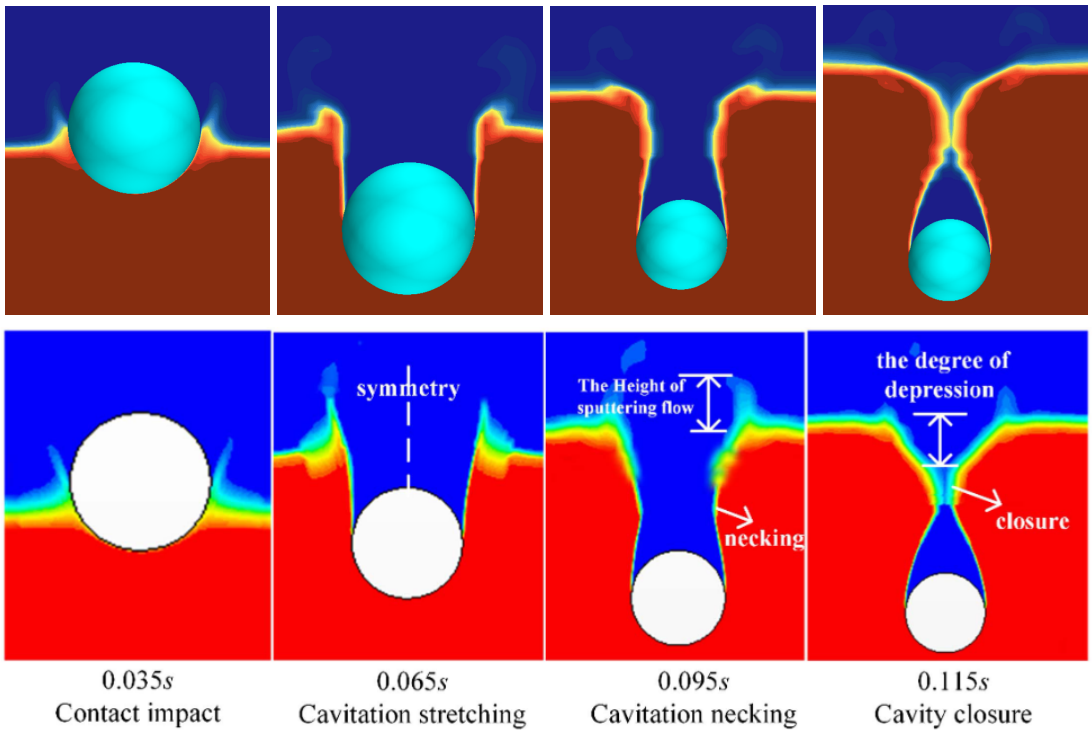

Fig. 5.5 Evolution of the cavity during impact of a 42 mm hydrophobic sphere on water at speed $V = 1$ ms^{-1} and atmospheric air density.

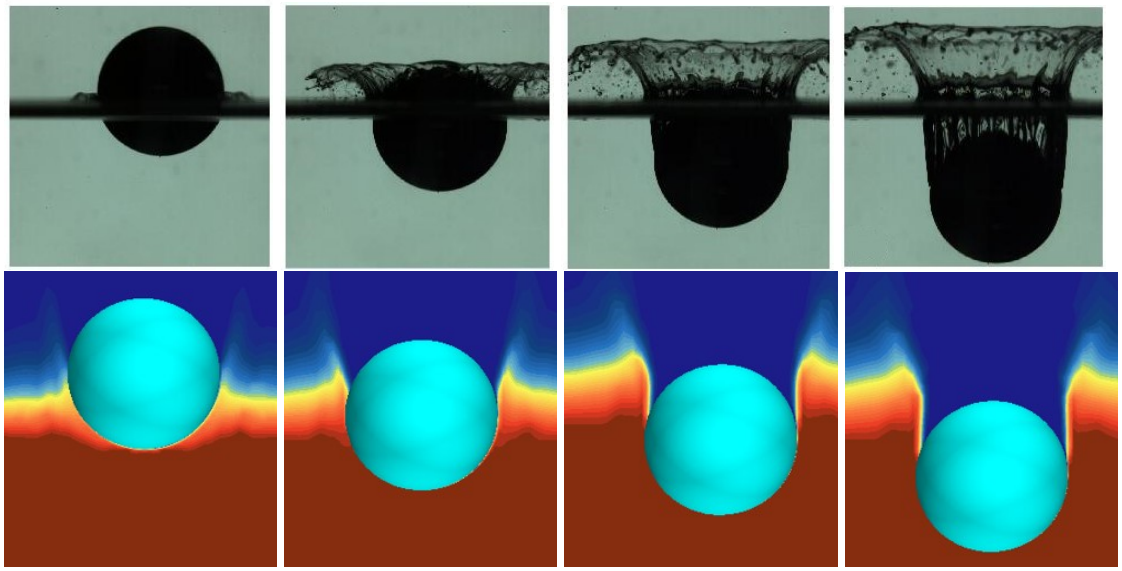

Fig. 5.6 Impact of a 15 mm hydrophobic sphere at speed $V = 2$ ms^{-1} and atmospheric air density. The top row shows the experimental results from Figure 3.4 and the bottom row shows the results from the VOF model.

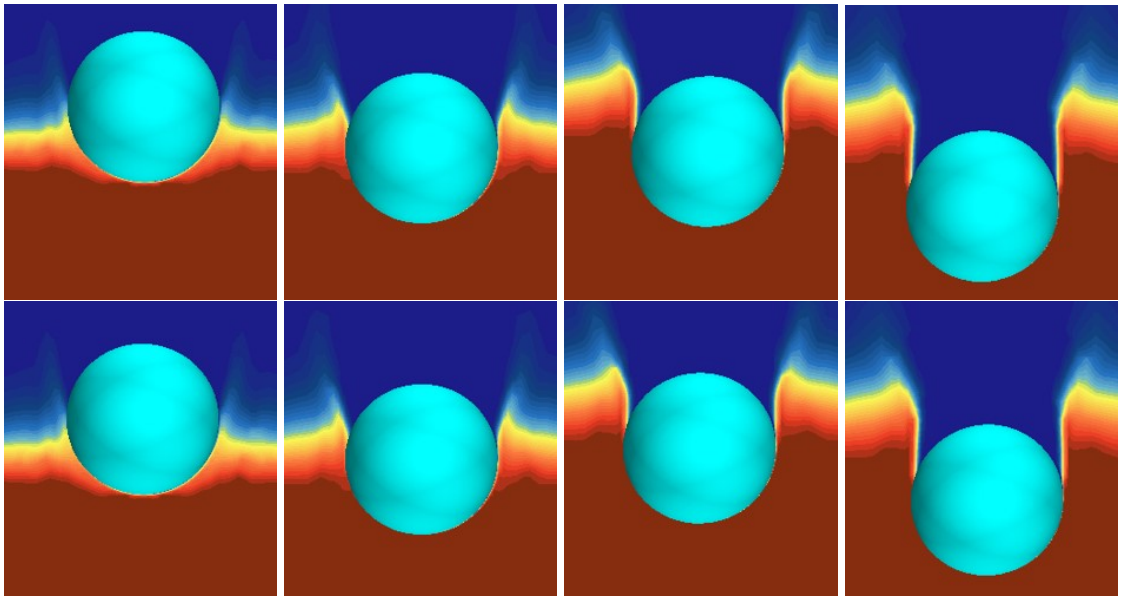

Fig. 5.7 Impact of a 15 mm hydrophobic sphere at speed $V = 2$ ms^{-1}. The top row shows ambient gas density $\rho_l = 1.18$ kg m^{-3} and the bottom row shows ambient gas density $\rho_l = 0.37$ kg m^{-3}.

shape of the cavity just prior to the moment of cavity closure. Once again, the qualitative phenomena found by Zhou et al. are reproduced, including the presence of cavitation stretching and necking.

Having verified the accuracy of our model, we proceeded to investigate the effect of changing the ambient gas density for the impact of a hydrophobic sphere. A sphere diameter of 15 mm and impact speed $V = 2$ ms^{-1} is used to enable a more direct comparison with our experimental data set. In Figure 5.6, we show that at this speed with atmospheric gas density the VOF model is able to capture the fact that a cavity forms. In Figure 5.7, a hydrophobic sphere impacted the liquid at $V = 2$ ms^{-1} with two different gas densities of $\rho_l = 1.18$ kg m^{-3} and $\rho_l = 0.37$ kg m^{-3}. It was found that the two processes were almost indistinguishable when the gas density was lowered to one-fifth atmospheric gas density, with an identical outcome and no suppression of cavity formation.

5.6 Discussion

In this chapter, we have proposed a theoretical mechanism for cavity suppression at reduced gas densities which is based on the modification of the dynamics of the splash crown by the presence of ambient gas. More specifically, the ambient gas slows sealing of the thin crown sheet which forms around the sphere. The reasoning involved was found to reproduce the finding of Duez et al. [89] that the speed of the wetting front V_{front} is of order σ/μ for

hydrophilic spheres. The estimates relied on the fact that V_{front} is a small multiple of the impact speed of the sphere, which has been confirmed by experimental measurements of the maximum wetting speed carried out by Kubota et al. [152].

Since our experimental data set uses spheres with low contact angles and only varies the properties of the liquid and the gas, it is of interest to investigate whether cavity formation can be suppressed at reduced gas densities in the case of hydrophobic spheres. For this purpose, we performed simulations using a three-dimensional VOF multiphase model which employs overlapping meshes. The simulations were validated by showing that they reproduce the results of Zhou et al. [146] on splashing of hydrophobic sphere at atmospheric gas density with good agreement on the geometry and characteristics of the cavity.

It was found that in the VOF simulations that decreasing ambient gas density is not able to suppress cavity formation in the case of hydrophobic spheres. We regard this as indirect support for our proposed theoretical mechanism, since we argue that the motion of the splash crown is connected to the motion of the contact line over the range of diameters which we considered. It follows that if a contact line instability causes the contact line at the root of the splash crown to depart from the surface of the sphere such that a cavity forms at any impact speed, it would not be possible to suppress cavity formation by decreasing the density of the ambient gas.

Chapter 6

Conclusions

6.1 Main Results

The main finding of our work is that in a range of parameters, the presence of ambient gas plays role in cavity formation for impacts of spheres on free liquid roles and that changing the properties of the gas can suppress cavity formation entirely, a result which may have applications in naval hydrodynamics and engineering. We identified the dominant property for cavity suppression to be the density of the gas, whereas the mean free path only affects the appearance of the splash curtain and the ejection of secondary droplets.

A theoretical mechanism was proposed for this effect whereby the presence of the ambient gas slows sealing of the thin crown sheet behind the sphere. The reasoning behind this mechanism was shown to be consistent with the theoretical results of Duez et al. [89] at atmospheric pressures. As part of our focus on the dynamics of the splash crown, we performed optical measurements enabling estimates of the crown thickness during impact. In general, trying to perform measurements of the thickness of a splash curtain during impact is extremely challenging, so this is a valuable result in its own right. Previous studies have used alternative methods to estimate the thickness of the liquid sheet or inserted values by hand to enable a best fit with experimental data [3, 90].

Although we did not have access to hydrophobic spheres in our experimental study, we performed simulations with a VOF multiphase model to study the influence of ambient gas density on hydrophobic spheres which form a cavity for any impact speed at atmospheric pressures. In common with the experimental literature, previous numerical studies of sphere-liquid impacts have only considered the properties of the solid and the liquid or varied the angle of the impactor in a way which might be difficult in an experimental study [146]. In our simulations, it was found that if a sphere forms a cavity at any speed, this cavity cannot be suppressed by lowering the density of the gas. This is consistent with

the mechanism which we proposed for cavity suppression, since lowering the gas density influences the dynamics of the splash crown when it is attached to the sphere.

6.2 Suggestions for Further Work

The work opens up a number of avenues for further investigation. Since the role of surface roughness is similar to but distinct from that of contact angle, it would clearly be interesting to study the combined influence of surface roughness and properties of the ambient gas on cavity formation or identify regimes where one is more important than the other [108].

As stated in Section 6.1, the mean free path only influences ejection of secondary droplets during impact and does not influence the speed of propagation of the splash curtain, which is what is important for deciding the threshold for cavity formation. Further work could investigate in more detail the role of the different properties of the gas (density, viscosity and mean free path) on quantitative properties of the secondary droplets, including the number of droplets ejected and their ejection angle. It could also be determined whether droplet size and horizontal velocity are independent of the properties of the ambient gas, as they are for droplet impacts on smooth dry surfaces at high Reynolds and Weber numbers [49]. However, unlike droplet impacts, studying the quantitative properties of these droplets cannot be used to classify the splashing outcome.

Another part of the work which would merit further study on both the experimental and the theoretical side is the presence of a plateau for threshold speed at low gas densities below one-fifth atmospheric density. We attributed this to a type of ribbing instability which is usually observed for some configuration of one or two cylinders which rotate on a free liquid surface and which are partially submerged so that the contact line is non-existent. Although we noted that the number of bubbles which can appear around the sphere matches the number of buckles which appear in the splash crown in connection with the periodic saw-tooth pattern of the contact line, a criterion would still need to be established which reproduces the threshold capillary number at which ribbing onset seems to occur.

References

[1] A.M. Worthington and R.S. Cole, Impact with a liquid surface, studied by the aid of instantaneous photography, Phil. Trans. R. Soc. Lond. A **189**, 137 (1897).

[2] A.M. Worthington, *A Study of Splashes* (Longmans Green and Company, New York, 1908).

[3] J.O. Marston, T.T. Truscott, N.B. Speirs, M.M. Mansoor and S.T. Thoroddsen, Crown sealing and buckling instability during water entry of spheres, J. Fluid Mech. **794**, 506-529 (2016).

[4] D. Gilbarg and R.A. Anderson, Influence of Atmospheric Pressure on the Phenomena Accompanying the Entry of Spheres into Water, J. Appl. Phys. **19**, 127-139 (1948).

[5] A. May, Vertical Entry of Missiles into Water, J. Appl. Phys **23**, 1362 (1952).

[6] Y. Yakimov, Effect of the atmosphere with the fall of bodies into water, Fluid Dyn. **8**, 679-682 (1975).

[7] T. von Kármán, The impact on seaplane floats during landing, NACA TN **321** (1929).

[8] H. Wagner, Phenomena associated with impacts and sliding on liquid surface, Zeit. Ange. Math. Mech. **12**, 193-215 (1932).

[9] S.D. Howison, J.R. Ockendon and S.K. Wilson, Incompressible water-entry problems at small deadrise angles, J. Fluid Mech. **222**, 215-230 (1991).

[10] T.F. Ogilvie, Compressibility effects in ship slamming, Schiffstechnik **10**, 147-154 (1963).

[11] A. Korobkin, Blunt-body impact on the free surface of a compressible fluid, J. Fluid Mech. **263**, 319-342 (1994).

[12] B.J. de Gans, P.C. Duineveld and U.S. Schubert, Inkjet printing of polymers: state of the art and future developments, Adv. Mater. **16**(3), 203-213 (2004).

[13] T. Ueda, T. Enomoto and M. Kanetsuki, Heat transfer characteristics and dynamic behaviour of saturated droplets impinging on a heated vertical surface, Bull. JSME **22**(167), 724-732 (1979).

[14] M. Kahani, R.G. Jackson and G. Rosengarten, Experimental investigation of TiO2/Water nanofluid droplet impingement on nanostructured surfaces, Ind. Eng. Chem. Res. **55**, 2230-2241 (2016).

[15] M.S. Mahdipoor, F. Tarasi. C. Moreau, A. Dolatabadi and M. Medraj, HVOF sprayed coatings of nano-agglomerated tungsten-carbide/cobalt powders for water droplet erosion application, Wear **330-331**, 338-347 (2015).

[16] J.S. -Pereira, P.G. Aleiferis, H.L. Walmsley, T.J. Davies and R.F. Cracknell, Heat flux characteristics of spray wall impingement with ethanol, butanol, iso-octane, gasoline and E10 fuels, Int. J. Heat Fluid Flow **44**, 662-683 (2013).

[17] L. Xu, W.W. Zhang and S.R. Nagel, Drop splashing on a dry smooth surface, Phys. Rev. Lett. **94**, 184505 (2005).

[18] G. Riboux and J.M. Gordillo, Experiments of Drops Impacting a Smooth Solid Surface: A Model of the Critical Impact Speed for Drop Splashing, Phys. Rev. Lett. **113**, 024507 (2014).

[19] G. Riboux and J.M. Gordillo, Boundary-layer effects in droplet splashing, Phys. Rev. E **96**, 013105 (2017).

[20] G. Riboux and J.M. Gordillo, A note on the aerodynamic splashing of droplets, J. Fluid. Mech. **871** (2019).

[21] M. Pierzyna, D.A. Burzynski, S.E. Bansmer and R. Semaan, Data-driven splashing threshold model for drop impact on dry smooth surfaces, Phys. Fluids **33**, 123317 (2021).

[22] M. Rein, Phenomena of liquid drop impact on solid and liquid surfaces, Fluid Dyn. Res. **12**, 61 (1993).

[23] Y. Guo, Y. Lian, and M. Sussman, Investigation of drop impact on dry and wet surfaces with consideration of surrounding air, Phys. Fluids **28**, 073303 (2016).

[24] J. Hao, L. Lee, Z. Wu, G. Hu and J.M. Floryan, Droplet splashing on an inclined surface, Phys. Rev. Lett. **122**, 054501 (2019).

[25] J.R. Castrejón-Pita, B.N. Muñoz-Sánchez, I.M. Hutchings and A.A. Castrejón-Pita, Droplet impact onto moving liquids, J. Fluid Mech. **809**, 716-725 (2016).

[26] H. Dong, W.W. Carr and J.F. Morris, An experimental study of drop-on-demand drop formation, Phys. Fluids **18**, 072102 (2006).

[27] A.U. Chen, P.K. Notz and O.A. Basaran, Computational and Experimental Analysis of Pinch-Off and Scaling, Phys. Rev. Lett. **88**, 174501 (2002).

[28] R. Li, N. Ashgriz, S. Chandra and J.R. Andrews, Contraction of free liquid ligaments, Am. Inst. Chem. Eng. J **54**, 3084 (2008).

[29] J.R. Castrejón-Pita, A.A. Castrejón-Pita, E.J. Hinch, J.R. Lister and I.M. Hutchings, Self-similar breakup of near-inviscid liquids, Phys. Rev. E **86**, 015301 (2012).

[30] J.R. Castrejón-Pita, N.F. Morrison, O.G. Harlen, G.D. Martin and I.M. Hutchings, Experiments and Lagrangian simulations on the formation of droplets in drop-on-demand mode, Phys. Rev. E **83**, 036306 (2011).

[31] D. Roy, M. Sophia, S.S. Rao and S. Basua, Droplet impact on immiscible liquid pool: Multi-scale dynamics of entrapped air cushion at short timescales, Phys. Fluids **34**, 052004 (2022).

[32] J.S. Lee, B.M. Weon, S.J. Park, J.T. Kim, J. Pyo, K. Fezzaa and J.H. Je, Air evolution during drop impact on liquid pool, Sci. Rep. **10**, 5790 (2020).

[33] B.D. Fudge, R. Cimpeanu and A.A. Castrejón-Pita, Dipping into a new pool: The interface dynamics of drops impacting onto a different liquid, Phys. Rev. E **104**, 065102 (2021).

[34] S.K. Das, A. Dalal, M. Breuer and G. Biswas, Evolution of jets during drop impact on a deep liquid pool, Phys. Fluids **34**, 022110 (2022).

[35] F. Minami and K. Hasegawa, Cavity and jet formation after immiscible droplet impact into deep water pool, Phys. Fluids **34**, 033315 (2022).

[36] E. Berberovic, N.P. van Hinsberg, S. Jakirlic, I.V. Roisman and C. Tropea, Drop impact onto a liquid layer of finite thickness: Dynamics of the cavity evolution, Phys. Rev. E **79**, 036306 (2009).

[37] U. Jain, M. Jalaal, D. Lohse and D. van der Meer, Deep pool water-impacts of viscous oil droplets, Soft Matt. **15**(233), 4629-4638 (2019).

[38] B. Ray, G. Biswas and A. Sharma, Regimes during liquid drop impact on a liquid pool, J. Fluid Mech. **768**, 492-523 (2015).

[39] G. Taylor, The dynamics of thin sheets of fluid II: Waves on fluid sheets, Proc. R. Soc. London, Ser. A. **253**, 296 (1959).

[40] E. Castillo-Orozco, A. Davanlou, P.K. Choudhury and R. Kuman, Droplet impact on deep liquid pools: Rayleigh jet to formation of secondary droplets, Phys. Rev. E **92**, 053022 (2015).

[41] G. Cerne, S. Petelin and I. Tizelj, Coupling of the Interface Tracking and the Two-Fluid Models for the Simulation of Incompressible Two-Phase Flow, J. Comp. Phys. **171**, 2: 776-804 (2001).

[42] O.G. Engel, Initial pressure, initial flow velocity, and the time dependence of crater depth in fluid impacts, J. Appl. Phys. **38**, 3935-3940 (1967).

[43] J.L. Liow, Splash formation by spherical drops, J. Fluid Mech. **427**, 73-105 (2001).

[44] A. Bisighini and G.E. Cossali, Crater evolution after the impact of a drop onto a semi-infinite liquid target, Phys. Rev. E **82**, 036319 (2010).

[45] C. Josserand and S. Zaleski, Droplet splashing on a thin liquid film, Phys. Fluids **15**, 1560 (2003).

[46] H. Yuan, J. Li, X. He, L. Chen, Z. Wang and J. Tan, Study of droplet splashing on a liquid film with a tunable surface tension pseudopotential lattice Boltzmann method, AIP Adv. **10**, 025209 (2020).

[47] C. Josserand, P. Ray and S. Zaleski, Droplet impact on a thin liquid film: anatomy of the splash, J. Fluid Mech. **802**, 775-805 (2016).

[48] D.A. Burzynski and S.E. Bansmer, Droplet splashing on thin moving films at high weber numbers, Int. J. Multiph. Flow **101**, 202–211 (2018).

[49] D.A. Burzynski and S.E. Bansmer, Role of surrounding gas in the outcome of droplet splashing, Phys. Rev. Fluid **4**, 073601 (2019).

[50] C.R. Wilke, A viscosity equation for gas mixtures, J. Chem. Phys. **18**, 517 (1950).

[51] S.G. Jenning, The mean free path in air, J. Aerosol Sci. **19**, 159 (1988).

[52] T. Ashida, M. Watanabe, K. Kobayashi, H. Fujii and T. Sanada, Hidden prompt splashing by corona splashing at drop impact on a smooth dry surface, Phys. Rev. Fluids **5**, 011601 (2020).

[53] L. Xu, L. Barcos and S.R. Nagel, Splashing of liquids: Interplay of surface roughness with surrounding gas, Phys. Rev. E **76**, 066311 (2007).

[54] C. Josserand and S.T. Thoroddsen, Drop Impact on a Solid Surface, Ann. Rev. Fluid Mech. **48**, 365-391 (2016).

[55] M. Marengo, C. Antonini, I.V. Roisman and C. Tropea, Drop collisions with simple and complex surfaces, Curr. Opin. Coll. Interface Sci. **16**, 292-302 (2011).

[56] J. Palacios, J. Hernández, P. Gómez, C. Zansi and J. López, Experimental study of splashing patterns and the splashing/deposition threshold in drop impacts onto dry smooth solid surfaces, Exp. Therm. Fluid Sci. **44**, 571-582 (2013).

[57] J. Hao, Effect of surface roughess on droplet splashing, Phys. Fluids **29**, 122105 (2017).

[58] L. Xu, Liquid drop splashing on smooth, rough, and textured surfaces, Phys. Rev. E **75**, 056316 (2007).

[59] A.A. Castrejón-Pita, J.R. Castrejón-Pita and I.M. Hutchings, Experimental observation of von Kármán vortices during drop impacts, Phys. Rev. E **86**, 045301 (2012).

[60] A. Latka, A. Strandburg-Peshkin, M.M. Driscoll, C.S. Stevens and S.R. Nagel, Creation of prompt and thin-sheet splashing by varying surface roughness or increasing air pressure, Phys. Rev. Lett. **109**, 054501 (2012).

[61] P.G. de Gennes, On Fluid/Wall Slippage, Lang. **18**, 3413 (2002).

[62] M.B. Lesser, Analytic solutions of liquid-drop impact problems, Proc. R. Soc. Lond. A **377**, 289-308 (1981).

[63] M.B. Lesser and J.E. Field, The impact of compressible liquids, Annu. Rev. Fluid Mech. **15**, 97-122 (1983).

[64] K.K. Haller, D. Poulikakos, Y. Ventikos and P. Monkewitz, Shock wave formation in droplet impact on a rigid surface: lateral liquid motion and multiple wave structure in the contact line region, J. Fluid Mech. **490**, 1-14 (2003).

[65] M. Mani, S. Mandre and M.P. Brenner, Events before droplet splashing on a solid surface, J. Fluid Mech. **647**, 163-185 (2010).

[66] S. Mandre and M.P. Brenner, The mechanism of a splash on a dry solid surface, J. Fluid Mech. **690**, 148-172 (2012).

[67] S. Mandre, M. Mani and M.P. Brenner, Precursors to Splashing of Liquid Droplets on a Solid Surface, Phys. Rev. Lett. **102**, 134502 (2009).

[68] G.I. Taylor and P.G. Saffman, Effects of compressibility at low Reynolds number, J. Aeronaut. Sci. **24**, 553 (1957).

[69] T. de Goede, K. de Bruin, N. Shahidzadeh and D. Bonn, Droplet splashing on rough surfaces, Phys. Rev. Fluids **6**, 043604 (2021).

[70] J.W.M. Bush and D.L. Hu, Walking on water: biolocomotion at the interface, Ann. Rev. Fluid Mech. **38**, 339-369 (2006).

[71] J.V. Ward, *Aquatic Insect Ecology: Biology and Habitat* (John Wiley, 1992).

[72] N.B. Speirs, M.M. Mansoor, J. Belden and T.T. Truscott, Water entry of spheres with various contact angles, J. Fluid Mech. **862**, R3 (2019).

[73] J.A. Aristoff, T.T. Truscott, A.H. Techet and W.M. John, The water entry of decelerating spheres, Phys. Fluid **22**, 3 (2010).

[74] R.C. Hurd, J. Belden, M.A. Jandron, D.T. Fanning, A.F. Bower and T.T. Truscott, Water entry of deformable spheres, J. Fluid Mech. **824**, 912-930 (2017).

[75] L. Yang, Y. Wei, J. Li, C. Wang and W. Xia, Experimental study on splash behaviors and cavity shape of elastic spheres during water entry, App. Ocean Res. **113**, 102754 (2021).

[76] D.A. Watson, J.M. Bom, M.P. Weinberg, C.J. Souchik and A.K. Dickerson, Water entry dynamics of spheres with heterogeneous wetting properties, Phys. Rev. Fluids **6**, 044003 (2021).

[77] J.O. Marston, I.U. Vakarelski and S.T. Thoroddsen, Cavity formation by the impact of Leidenfrost spheres, J. Fluid Mech. **699**, 465-488 (2012).

[78] A. Jetly, I.U. Vakarelski, Z. Yhang and S.T. Thoroddsen, Giant drag reduction on Leidenfrost spheres evaluated from extended free-fall trajectories, Exp. Therm. Fluid Sci. **102**, 181-188 (2019).

[79] M.M. Mansoor, J.O. Marston, I.U. Vakarelski and S.T. Thoroddsen, Water entry without surface seal: extended cavity formation, J. Fluid Mech. **743**, 295-326 (2014).

[80] B.C.-W. Tan, J.H.A. Vlaskamp, P. Denissenko, and P.J. Thomas, Cavity formation in the wake of falling spheres submerging into a stratified two-layer system of immiscible liquids, J. Fluid Mech. **790**, 33-56 (2014).

[81] L.B. Smolka and C.K. McLaughlin, Sphere entry through an oil lens floating on water, Phys. Rev. Fluids **4**, 044001 (2019).

[82] N. Kim and H. Park, Water entry of rounded cylindrical bodies with different aspect ratios and surface conditions, J. Fluid Mech. **790**, 33-56 (2019).

[83] O. Enriquez, I.R. Peters, S. Gekle and L.E. Schmidt, Collapse and pinch-off of a non-axisymmetric impact-created air cavity in water, J. Fluid Mech **701**, 40-58 (2012).

[84] T.T. Truscott, B.P. Epps and J. Belden, Water entry of projectiles, Ann. Rev. Fluid Mech. **46** (1), 355-378 (2014).

[85] J.O. Marston, M.M. Mansoor, S.T. Thoroddsen and T.T. Truscott, The effect of ambient pressure on ejecta sheets from free-surface ablation, Exp. Fluids **57**, 61 (2016).

[86] H.I. Abelson, Pressure measurement in the water-entry cavity, J. Fluid Mech. **44**, 129-144 (1970).

[87] M. Lee, R.G. Longoria and D.E. Wilson, Cavity dynamics in high-speed water entry, Phys. Fluids **9**, 540 (1997).

[88] D. van der Meer, Wrapping up a centry of splashes, J. Fluid Mech. **800**, 1-4 (2016).

[89] C. Duez, C. Ybert, C. Clanet and L. Bocquet, Making a splash with water repellency, Nat. Phys. **3**, 180-183 (2007).

[90] J.M. Aristoff and J.W.M. Bush, Water entry of small hydrophobic spheres, J. Fluid Mech. **619**, 45-78 (2009).

[91] J.H. Snoeijer and B. Andreotti, Moving contact lines, regimes and dynamical transitions, Ann. Rev. Fluid Mech. **45**, 269-292 (2013).

[92] Y.D. Shikhmurzaev, Moving contact lines in liquid/liquid/solid systems, J. Fluid Mech. **334**, 211-249 (1997).

[93] J. Billingham, On the model for the motion of a contact line on a smooth solid surface, Euro. J. App. Math. **17**, 347-382 (2006).

[94] H. Ding, B.-Q. Chen, H.-R. Liu, C.-Y. Zhang and P. Gao, On the contact-line pinning in cavity formation during solid-liquid impact, J. Fluid Mech. **783**, 504-525 (2015).

[95] F.-C. Yang, X.-P. Chen and P. Yue, The influence of "gas" viscosity on water entry of hydrophobic spheres, Eur. Phys. Jour. E **42**, 34 (2019).

[96] J.O. Marston, I.U. Vakarelski and S.T. Thoroddsen, Bubble entrapment during sphere impact onto quiescent liquid surface, J. Fluid Mech. **680**, 660-670 (2011).

[97] M.R. Moore, Introducing pre-impact air-cushioning effects into the Wagner model of impact theory, J. Eng. Math. **129**, 6 (2021).

[98] M. Pack, P. Kaneelil, H. Kim and Y. Sun, Contact Line Instability Caused by Air Rim Formation under Nonsplashing Droplets, Langmuir **34** (17), 4962-4969 (2018).

[99] J.A. Diez and L. Kondic, Contact Line Instabilities of Thin Liquid Films, Phys. Rev. Lett. **86**, 632 (2001).

[100] H. Williams, Solitary waves on falling liquid films in the low Reynolds number regime, IOP SciNotes **1**, 025209 (2020).

[101] D. Quere, On the minimal velocity of forced spreading in partial wetting, C. R. Acad. Sci., Ser. II: Mec., Phys., Chim., Sci. Terre Univers **313**, 313 (1991).

[102] R.V. Sedev and J.G. Petrov, The critical condition for transition from steady wetting to film entrainment, Colloids Surf. **53**, 147 (1991).

[103] S.-Y. Nieh, R.M. Ybarra and P. Neogi, Wetting Kinetics of Polymer Solutions: Experimental Observations, Macromolecules **29**, 320-325 (1996).

[104] P.G. López, M.J. Miksis and S.G. Bankoff, Inertial effects on contact line instability in the coating of a dry inclined plate, Phys. Fluids **9**, 2177 (1997).

[105] J. Eggers, Instability of a moving contact line. arXiv:physics/0501096v1.

[106] P. Neogi, Contact line instability in spontaneous spreading of a drop on a solid surface, J. Fluid Mech. **428**, 171-183 (2001).

[107] A.L. Bertozzi and M.P. Brenner, Linear stability and transient growth in driven contact lines, Phys. Fluids **9**, 530 (1997).

[108] M.-H. Zhao, X.-P. Chen and Q. Wang, Wetting failure of hydrophilic surfaces promoted by surface roughness, Sci. Rep. **4**, 5376 (2014).

[109] X. Huang and I. Gates, Apparent Contact Angle around the Periphery of a Liquid Drop on Roughened Surfaces, Sci. Rep. **10**, 8220 (2020).

[110] H. Williams, Superhydrophobic Sand Repels Water, Phys. Teach. **61**, 138 (2023).

[111] D. Bonn, J. Eggers, J. Indekeu, J. Meunier and E. Rolley, Wetting and spreading, Rev. Mod. Phys. **81**, 739 (2009).

[112] J. Eggers, Hydrodynamic theory of forced dewetting, Phys. Rev. Lett. **93**, 094502 (2004).

[113] J. Drelich and A. Marmur, Physics and applications of superhydrophobic and superhydrophilic surfaces and coatings, Sur. Inn. **2**, 4 (2014).

[114] H. Benkreira and M.I. Khan, Air entrainment in dip coating under reduced air pressures, Chem. Eng. Sci. **63**, 448-459 (2008).

[115] J.E. Sprittles, Kinetic effects in dynamic wetting, Phys. Rev. Lett. 118, 114502 (2017).

[116] J.E. Sprittles, Air entrainment in dynamic wetting: Knudsen effects and the influence of ambient air pressure, J. Fluid Mech. **769**, 444-481 (2015).

[117] J.S. Keeler, T.D. Blake, D.A. Lockerby and J.E. Sprittles, Putting the micro into the macro: a molecularly augmented hydrodynamic model of dynamic wetting applied to flow instabilities during forced dewetting, J. Fluid Mech. **953**, A17 (2022).

[118] D. Quéré, Wetting and roughness, Ann. Rev. Mater. Res. **38**, 71-99 (2008).

[119] P. Pavlicek and O. Hybl, White light interferometry on rough surfaces - measurement uncertainty caused by surface roughness, Appl. Opt. **47**, 16 (2008).

[120] T. Dresel, G. Häusler and H. Venzke, Three-dimensional sensing of rough surfaces by coherence radar, Appl. Opt. **31**, 919-925 (1992).

[121] H. Williams, Influence of curved surface roughness on white light interferometer microscopy, Phys. Educ. **57**, 015001 (2021).

[122] N.B. Speirs, K.R. Langley, Z. Pan, T.T. Truscott and S.T. Thoroddsen, Cavitation upon low-speed solid-liquid impact, Nat. Comms. **12**, 7250 (2021).

[123] K. Sefiane, Thermal Effects in the Splashing of Drops under a Reduced Pressure Environment, Phys. Rev. Lett. **96**, 179401 (2006).

[124] L. Xu, W.W. Zhang and S.R. Nagel, Reply to the Comment by Khellil Sefiane, Phys. Rev. Lett. **96**, 179402 (2006).

[125] G. Yang, V. Vaikuntanathan, A. Terzis, X. Cheng, B. Weigand and R. Helmig, Impact of a Linear Array of Hydrophilic and Superhydophobic Spheres on a Deep Water Pool, Coll. Inter. **2019**: 3, 29 (2019).

[126] T.T. Truscott and A.H. Techet, A spin on cavity formation during water entry of hydrophobic and hydrophilic spheres, Phys. Fluids **21**, 121703 (2009).

[127] S.K. Panda, B.K. Rana and P. Kumar, Entrainment in multifluid systems, and rotation induced occurrences, Eur. J. Mech./B Fluids **96**, 156-172 (2022).

[128] M.S. Carvalho and L.E. Scriven, Three-Dimensional Stability Analysis of Free Surface Flows: Applications to Forward Deformable Roll Coating, J. Comp. Phys. **151**, 534-562 (1999).

[129] D.J. Coylet, C.W. Macosko and L.E. Scriven, Stability of symmetric film-splitting between counter-rotating cylinders, J. Fluid Mech. **216**, 437-458 (1990).

[130] C. Vernay, Destabilisation of liquid sheets of dilute emissions, Materials Science [cond-mat.mtrl.sci]. Université Montpellier, 2015. NNT: 2015MONTS199. Tel-01254934v2.

[131] C.B. Tibirica, F. J. do Nascimento and G. Ribatski, Film thickness measurement techniques applied to micro-scale two-phase flow systems, Exp. Therm. Fluid Sci. **34**, 4: 463-473 (2010).

[132] T. Ohyama, K. Endoh, A. Mikami and Y.H. Mori, Optical interferometry for measuring instantaneous thickness of transparent solid and liquid films, Rev. Sci. Instru. **59**, 2018-2022 (1988).

[133] S.V. Makarytchev, T.A.G. Langrish and R.G.H. Prince, Thickness and velocity of wavy liquid films on rotating conical surfaces, Chem. Eng. Sci. **56**, 77-87 (2001).

[134] M. Berhanu and E. Falcon, Space-time-resolved capillary wave turbulence, Phys. Rev. E **87** (3), 033003 (2013).

[135] L.U. Lilleleht and T.J. Hanratty, Measurement of interfacial structure for co-current air-water flow, J. Fluid Mech. **11** (1), 65-81 (1961).

[136] J. Kim and M.H. Kim, A photochromic dye activation method for measuring the thickness of liquid films, Bull. Korean Chem. Soc. **26** (6), 966-970 (2005).

[137] H. Williams, A case study of optical methods for measuring thickness of liquid sheets, Res. Opt. **8**, 100266 (2022).

[138] T.T. Truscott, B.P. Epps and A.H. Techet, Unsteady forces on spheres during free-surface water entry, J. Fluid Mech. **704** (2), 173-210 (2012).

[139] M. Vahab, D. Murphy and K. Shoele, Fluid dynamics of frozen precipitation at the air-water interface, J. Fluid Mech. **933**, A36 (2021).

[140] Z.L. Lu, Y.J. Wei, C. Wang and W. Cao, Experimental and numerical investigation on the flow structure and instability of water-entry cavity by a semi-closed cylinder, Acta Phys. Sin. **66** (6), 064702 (2017).

[141] X.Z. Hu and S.J. Liu, Numerical simulation of water entryof seafloor mining tool with free fall motion, Int. J. Fluid Mech. Res. **38** (3), 193-214 (2011).

[142] K.M.T. Kleefsman, G. Fekken, A.E.P. Veldman, B. Iwanowski and B. Buchner, A volume-of-fluid based simulation method for wave impact problems, J. Comput. Phys. **206** (1), 363-393 (2005).

[143] M. Jalaisendi, S.J. Osma and M. Porfiri, Three-dimensional water entry of a solid body: A particle image velocimetry study, J. Fluid Struct. **59**, 85-102 (2015).

[144] G.D. Xu, W.Y. Duan and G.X. Wu, Numerical simulation of oblique water entry of an asymmetrical wedge, Ocean Eng. **35** (16), 1597-1603 (2008).

[145] G.X. Wu, H. Sun and Y.S. He, Numerical simulation and experimental study of water entry of a wedge in free fall motion, J. Fluids Struct. **19** (3), 277-289 (2004).

[146] B. Zhou, H. Liu, G. Zhang, X. Han, X. Wang and S.-K. Tan, Simulation of Cavity Dynamics and Motion Characteristics for Water Entry of a Hydrophobic Sphere at Various Speeds and Angles, J. Eng. Mech. **146**, 9 (2020).

[147] M. Do-Quang and G. Amberg, The splash of a solid sphere impacting on a liquid surface: Numerical simulation of the influence of wetting, Phys. Fluids **21**, 022102 (2009).

[148] M. Do-Quang and G. Amberg, Numerical simulation of the coupling problems of a solid sphere impacting on a liquid free surface, Math. Comp. Sim. **80**, 1664-1673 (2010).

[149] M. Ahmadzadeh, B. Saranjam, A. Hoseini Fard and A.R. Binesh, Numerical simulation of sphere water entry problem using Eulerian-Lagrangian method, App. Math. Mod. **38**, 1673-1684 (2014).

[150] M.V. Chubynsky, K.I. Belousov, D.A. Lockerby and J.E. Sprittles, Bouncing off the Walls: The Influence of Gas-Kinetic and van der Waals Effects in Drop Impact, Phys. Rev. Lett. **124**, 084501 (2020).

[151] A.Y. Rednikov and P. Colinet, Contact-line singularities resolved exclusively by the Kelvin effect: volatile liquids in air, J. Fluid Mech. **858**, 881-916 (2018).

[152] Y. Kubota and O. Mochizuki, Splash Formation by a Spherical Body Plunging into Water, J. Visual. **12** (4), 339-346 (2009).

[153] J.H. Ferziger and M. Peric, *Computational methods for fluid dynamics* (New York: Springer, 1999).